KEK Report 2009-1
April 2009
H

Measurement of the Proton Longitudinal Structure Function F_L at HERA

Shima Shimizu

Institute of Particle and Nuclear Studies,
High Energy Accelerator Research Organization (KEK)
1-1 Oho, Tsukuba, Ibaraki 305-0801 Japan
and
Department of Physics, University of Tokyo
7-3-1 Hongo, Bunkyo-ku, Tokyo 113-0033 Japan

High Energy Accelerator Research Organization

KEK Reports are available from:

High Energy Accelerator Research Organization (KEK)
1-1 Oho, Tsukuba-shi
Ibaraki-ken, 305-0801
JAPAN

Phone: +81-29-864-5137
Fax: +81-29-864-4604
E-mail: irdpub@mail.kek.jp
Internet: http://www.kek.jp

Measurement of the Proton Longitudinal Structure Function F_L at HERA

Shima Shimizu

Institute of Particle and Nuclear Studies,
High Energy Accelerator Research Organization (KEK)
1-1 Oho, Tsukuba, Ibaraki 305-0801 Japan
and
Department of Physics, University of Tokyo
7-3-1 Hongo, Bunkyo-ku, Tokyo 113-0033 Japan

Abstract

The longitudinal structure function F_L has been directly measured for $24 \leq Q^2 \leq 110$ GeV^2 and $6.7 \cdot 10^{-4} \leq x \leq 4.9 \cdot 10^{-3}$ using the positron-proton inclusive deep inelastic scattering at three different center-of-mass energies, $\sqrt{s} = 318$, 252 and 225 GeV, at HERA. During the measurement, the double differential cross section is also measured at each beam energy for the same Q^2 but $0.13 \leq y \leq 0.75$. Reconstruction of the scattered positron and rejection of the background events were improved for this measurement. The extracted F_L is consistent with perturbative QCD predictions.

Contents

Chapter 1

Introduction

High energy physics has been aiming to understand the fundamental constituents of the world and the interaction between them. In our present understanding, the fundamental particles are 12 spin-$\frac{1}{2}$ fermions, i.e. 6 leptons and 6 quarks, classified to three generations. If we ignore the gravitation, which is too weak to have any importance in the current reach of high energy experiments, the interaction between the particles is mediated by exchanges of spin-1 gauge bosons. The bosons are γ, Z and W for electroweak interaction and gluons for strong interaction, respectively. The Standard Model has been established and successfully describes the various phenomena in the high energy physics.

The strong interaction, the interaction between the quarks and gluons, is described by the Quantum Chromodynamics (QCD). The QCD is a non-abelian SU(3) gauge theory and the gluon itself has the color charge, the charge in the strong interaction. Therefore, gluons can interact with themselves. The self-coupling of gluons determine the characteristics of the behavior of the coupling constant, α_s. At long distance, α_s is large leading confinement of quarks. At short distance, α_s gets small so that quarks and gluons behave as free particles. This is called asymptotic freedom. The small value of α_s means that perturvative calculation is applicable. According to the factorization theorem, the prediction of QCD processes is usually separated into two parts as calculation of hard process by perturbative QCD (pQCD) and experimentally extracted quantities which are considered as process independent.

The proton is one of the most familiar particles around us. The study of its structure is one of the mandatory topics in the QCD, since the proton consists of quarks and gluons. The proton structure itself is a very interesting topic since it would be direct answer to how matter is made of from its origin. In the view of QCD, the good understanding of the proton structure is indispensable for the pQCD prediction of any process involving the proton. The pQCD can describe the hard process with the partons, constituents of the proton in the pQCD view, but the distribution of the partons should be determined based on experimental results.

Historically, in the Rutherford's famous experiment [1], the scattering of α particles off a thin gold film, the angular distribution of scattered α particles revealed the existence of nuclei in the atoms. Starting with this, many scattering experiment has been performed to investigate the inner structure of matters. In the late 1960s, the

first experiments on highly inelastic electron scattering on liquid hydrogen targets were started at the two mile accelerator at the Stanford Linear Accelerator Center (SLAC). The results suggested the point-like constituents in the proton, called partons, which were identified as quarks after some years. Various lepton-nucleon deep inelastic scatterings (DIS) have been performed in following years and have contributed to develop the description of nucleons.

HERA was the unique electron-proton collider in the world operated from year 1992 to 2007 at DESY, Hamburg. The large center-of-mass energy of the scattering largely expanded the kinematic region explored by the previous experiments. The reachable highest value of the squared four momentum transfer, Q^2, was $Q^2 \sim 40000$ GeV^2, which corresponds to the resolution scale of 10^{-18} m, i.e. 1/1000 of the size of the proton. One of the striking early results from HERA is that the steep rise of the inclusive cross sections at the region with the low value of Bjorken x, where no other experiment can perform study. The rise is interpreted in the pQCD description, as there are lot of gluons which carry very small fraction of the proton momentum.

In 15 years of its operation, various measurements has been done at HERA related to both QCD and electroweak physics. From the precise measurements of the cross section of inclusive deep inelastic scattering over the HERA kinematic region, the parton distributions in the proton are well determined in the framework of pQCD. They will be used in the predictions of any processes involving protons at high energy, for example, physics at LHC, the large hadron collider started its operation in 2008, where the observation of new physics is highly expected.

However, further test of pQCD description is still important. There are many assumptions in the pQCD determination of parton distribution. One of such assumptions is on the approximation in a perturbative approach. The approach should have a limit on its validity. There are also other approaches which is theoretically suitable at low x. As QCD process is considered by a convolution of pQCD calculation and non-perturbative part such as parton density, deviation in pQCD calculation may be absorbed by the latter and sometimes may be invisible as long as a single observable is measured.

Concerning the low x physics, the proton structure is interpreted by gluon dominance. The gluon distribution in pQCD description is determined indirectly by Q^2 dependence of DIS cross section, which is called scaling violation. The determination is directly affected by pQCD calculation. Independent variable which has different sensitivity to the gluon distribution in the proton gives consistency check of current pQCD view of the proton structure.

The proton longitudinal structure function F_L is directly related to gluon dynamics in the proton. Since, in the pQCD, its sensitivity to gluon density is by a different manner from the scaling violation, F_L is highly expected to give a test of pQCD validity. Though HERA was the only possible place to study F_L at low x, the region with gluon dominance, the direct measurement had not done due to experimental difficulty. However, at the last months of HERA, HERA operated with significantly lowered proton beam energies. It gives an opportunity for the direct F_L measurement at HERA for the first time. This analysis aims the direct F_L measurement first time at the low x region to test our present understanding of the proton structure.

The thesis is organized as follows. In the next chapter the theoretical backgrounds for the deep inelastic scattering are given. The third chapter explains the experimental setup including description of HERA machine and the ZEUS detector. The fourth and fifth chapters describe event reconstruction and event selection for the measurement, respectively. Chapter 6 presents cross section measurement of inclusive deep inelastic scattering covering the region where indirect sensitivity to F_L is expected. The direct F_L extraction is performed in chapter 7, where its result is also shown. The conclusion is in chapter 8.

Chapter 2

Deep Inelastic Scattering and the Quantum Chromodynamics

2.1 Deep Inelastic Scattering

The lepton-proton scattering with a large momentum transfer is called **Deep Inelastic Scattering** (DIS). This process is interpreted in the quark-parton picture as the point-like lepton is scattered with a parton, a constituent of the proton, and then the proton is broken up. Its diagram is shown in Fig. 2.1. The interaction proceeds by an exchange of an electroweak virtual boson, namely γ^*, Z or W. The process via a neutral boson is called the neutral current (NC) process and that via W is called the charged current (CC) process, which changes the lepton charge via interaction.

A measurement summing up all the final states in the hadronic system is called inclusive measurement. The kinematics of the inclusive DIS process can be described by the following Lorentz invariant kinematic variables. With regarding k, p and k' as four-momentum of the incoming lepton, proton and outgoing lepton, respectively, the

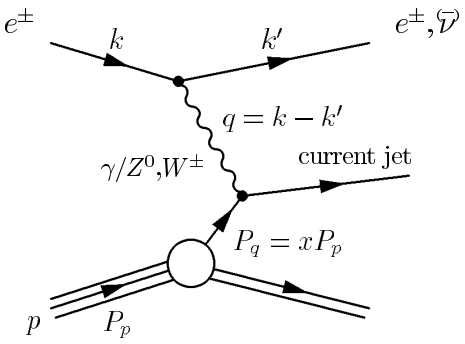

Figure 2.1: Diagram of the deep inelastic scattering.

variables are defined as

$$s \equiv (k+p)^2, \tag{2.1}$$
$$Q^2 \equiv -q^2 = -(k-k')^2, \tag{2.2}$$
$$x \equiv \frac{Q^2}{2p\cdot q}, \tag{2.3}$$
$$y \equiv \frac{p\cdot q}{p\cdot k}. \tag{2.4}$$

The variable s is the squared center-of-mass energy. The negative square of the momentum transfer, Q^2, is virtuality of the exchanged boson, which qualitatively corresponds to the resolution (λ) of the boson looking into the proton as

$$\lambda \sim \frac{1}{\sqrt{Q^2}}. \tag{2.5}$$

The variable x corresponds to the momentum fraction of a struck parton to the proton in the naïve quark-parton model (will be discussed in Sec. 2.3) and is equivalent to Bjorken scaling variable x. The variable y is inelasticy. By ignoring masses of protons and leptons, they are related to each other by an equation

$$Q^2 = sxy, \tag{2.6}$$

so that only two of them are independent at a given center-of-mass energy ($\sqrt{s}$).

2.2 DIS and the structure functions

The cross section of lepton-proton scattering can be written as a convolution of a leptonic part and a hadronic part,

$$d\sigma \sim L_{\mu\nu}W^{\mu\nu}, \tag{2.7}$$

where $L_{\mu\nu}$ and $W^{\mu\nu}$ are the leptonic and hadronic tensor, respectively. With ignoring electron masses, the leptonic tensor can be written as

$$L_{\mu\nu} = 2(k'_\mu k_\nu + k'_\nu k_\mu - (k'\cdot k)g_{\mu\nu}). \tag{2.8}$$

With the requirements of the Lorentz invariance, the hadronic tensor has the general form of [2]

$$W^{\mu\nu} = -W_1 g^{\mu\nu} + \frac{W_2}{M^2}p^\mu p^\nu - i\varepsilon^{\mu\nu\alpha\beta}p_\alpha q_\beta \frac{W_3}{2M^2} + q^\mu q^\nu \frac{W_4}{M^2} + (p^\mu q^\nu + q^\mu p^\nu)\frac{W_5}{M^2} + i(p^\mu q^\nu - p^\nu q^\mu)\frac{W_6}{2M^2}, \tag{2.9}$$

where M is the proton mass and W_i are scalar functions of x and Q^2 reflecting the proton structure. If the scattering proceeds by γ exchange only, the parity violation

term W_3 and also antisymmetric term W_6 are absent. The current conservation gives $q_\mu W^{\mu\nu} = q_\nu W^{\mu\nu} = 0$ so that

$$W_5 = -\frac{p \cdot q}{q^2} W_2 \tag{2.10}$$

$$W_4 = \frac{M^2}{q^2} W_1 + \left(\frac{p \cdot q}{q^2}\right)^2 W_2. \tag{2.11}$$

Therefore, the hadronic tensor depends W_1 and W_2 only and can be written as

$$W^{\mu\nu} = W_1 \left(-g^{\mu\nu} + \frac{q^\mu q^\nu}{q^2}\right) + \frac{W_2}{M^2} \left(p^\mu - \frac{p \cdot q}{q^2} q^\mu\right) \left(p^\nu - \frac{p \cdot q}{q^2} q^\nu\right). \tag{2.12}$$

The functions W_1 and W_2 are redefined as the structure functions F_1 and F_2 which depends on two Lorentz invariant kinematic variables of x and Q^2.

$$F_1(x, Q^2) = M W_1(x, Q^2) \tag{2.13}$$

$$F_2(x, Q^2) = \frac{p \cdot q}{M} W_2(x, Q^2). \tag{2.14}$$

Thus, the DIS cross section with γ^* exchange is written as

$$\frac{d^2\sigma}{dx dQ^2} = \frac{4\pi\alpha^2}{xQ^4} \left[\frac{y^2}{2} 2x F_1(x, Q^2) + (1 - y) F_2(x, Q^2)\right], \tag{2.15}$$

with ignoring mass terms. The longitudinal structure function is defined as

$$F_L = F_2 - 2x F_1. \tag{2.16}$$

The cross section can be also written as

$$\frac{d^2\sigma}{dx dQ^2} = \frac{2\pi\alpha^2}{xQ^4} \left[Y_+ F_2(x, Q^2) - y^2 F_L(x, Q^2)\right], \tag{2.17}$$

where $Y_+ = 1 + (1 - y)^2$. It is convenient to define reduced cross $\tilde{\sigma}$ section as

$$\tilde{\sigma} \equiv \frac{1}{Y_+} \frac{xQ^4}{2\pi\alpha^2} \frac{d^2\sigma}{dx dQ^2} = F_2(x, Q^2) - \frac{y^2}{Y_+} F_L(x, Q^2) \tag{2.18}$$

for discussion.

In principle, F_1 and F_2 are independently defined and both should not be negative from their nature. From Eq. 2.16, F_L is only required to be

$$0 \leq F_L \leq F_2. \tag{2.19}$$

By considering models on proton structure, F_2 and F_L start to have relation between each other.

The structure functions can be related to the cross section of the virtual photon and hadron interaction. The polarization vector $\epsilon(\lambda)$ of the virtual photon with momentum $q = (E, 0, 0, |\mathbf{p}|)$ can be written as

$$\epsilon(\pm 1) = \frac{1}{\sqrt{2}}(0, 1, \pm i, 0), \qquad \epsilon(0) = \frac{1}{\sqrt{E^2 - p^2}}(|\mathbf{p}|, 0, 0, E).$$

By calculating the cross section $\sigma(\lambda)$ with polarization λ, the cross sections for the virtual photon scattering are given for $Q^2 \gg M^2$ as

$$\sigma_T \equiv \frac{1}{2}(\sigma(+) + \sigma(-)) = \frac{4\pi^2\alpha}{Q^2(1-x)}(F_2 - F_L) \tag{2.20}$$

$$\sigma_L \equiv \sigma(0) = \frac{4\pi^2\alpha}{Q^2(1-x)}F_L, \tag{2.21}$$

where σ_T and σ_L are cross sections for transverse and longitudinal virtual photon, respectively. Equation 2.21 shows that F_L is the structure function which reflects the cross section of the scattering by the longitudinal virtual photon.

2.3 Quark-parton model

In the quark-parton model (QPM), the DIS is interpreted as the incoherent sum of elastic scattering between the probing lepton and partons, the point-like constituents of the proton, which were identified as spin-$\frac{1}{2}$ quarks. In this model, the structure functions is written as

$$F_2(x, Q^2) = \sum_q e_q^2 x q(x), \tag{2.22}$$

where e_q is the charge of parton q and $q(x)$ is the probability of the parton q to have momentum fraction x of the proton. The sum runs over all partons in the proton. This means that F_2 depends only on x and has no Q^2 dependence. It is called Bjorken scaling and is observed in the first DIS experiment at SLAC.

Since the longitudinal virtual photon cannot interact with spin-$\frac{1}{2}$ particles, $\sigma_L = 0$, the model predicts

$$F_L(x, Q^2) = 0, \tag{2.23}$$

and consequently gives

$$F_2(x) = 2xF_1(x), \tag{2.24}$$

which is known as Callan-Gross relation [3], valid for spin-$\frac{1}{2}$ partons.

The QPM cannot describe whole property of the DIS. Following three issues are un-answered.

- Partons are confined inside the proton so that they cannot behave as free particles.
- The Bjorken scaling is violated, i.e. a weak Q^2 dependence of the F_2 is experimentally observed.
- The momentum sum of the partons over the proton is only about a half of the proton.

2.4 Quantum Chromodynamics (QCD)

The Quantum Chromodynamics (QCD) is the theory to describe the strong interaction between quarks through color charge coupling. A quark carries one of the three color charges of *red*, *green* and *blue*. The interaction between the quarks is mediated by the exchange of massless spin-1 bosons called gluons. The QCD is a non-abelian SU(3) gauge theory. As a consequence, there are eight gluons and they also have color charge so that they can interact among themselves. Only colorless particles can exist as free particles so that the quarks and gluons should always be confined in hadrons and cannot be observed as free particles.

The framework of the QCD is an analogue to that of the quantum electrodynamic (QED) though the gluon self-coupling in the QCD makes the property of its interaction totally different from that of the QED. The strong interaction of the QCD is characterized by the coupling constant α_s. While the coupling constant α in the QED is generally small and increases only slightly with increase of Q^2, α_s is large at small Q^2 and decreases as Q^2 increases.

The energy scale dependence of the coupling is expressed by the basic renormalization group equation, using $g(\mu) = \sqrt{4\pi\alpha_s(\mu^2)}$,

$$\mu\frac{dg(\mu)}{d\mu} = \beta(g(\mu)) = -2\alpha_s\left(\frac{\alpha_s}{4\pi}\beta_1 + \left(\frac{\alpha_s}{4\pi}\right)^2\beta_2 + \cdots\right). \tag{2.25}$$

$\beta(g)$ is called beta function with

$$\beta_1 = 11 - \frac{2}{3}N_f \tag{2.26}$$

at leading order (LO), where N_f is the number of flavors of quarks.

In the first order, the solution of Eq. 2.25 is given as

$$\alpha_s(\mu^2) = \frac{12\pi}{(33 - 2N_f)\ln\frac{\mu^2}{\Lambda^2_{\mathrm{QCD}}}}, \tag{2.27}$$

where Λ_{QCD} characterizes the energy scale at which the strong coupling constant becomes large and is the order of 300 - 500 MeV. At large energy scale μ, corresponding to short scale, α_s gets logarithmically close to 0, which is known as **asymptotic freedom**. It is a necessary condition for application of perturbative calculation in the QCD.

Another important issue for the application of perturbative calculation is **factorization theorem**, which states that the physics process involving quarks or gluons can be separated into short distance and long distance parts. The former is a hard process which is process dependent and can be calculated by perturbative QCD (pQCD). The latter is largely process independent but not predictable so that it requires experimental results. This part absorbs the divergence, which come from gluon self-coupling, if perturbation were applied at the low energy scale.

From the factorization theorem, the inclusive cross section of the DIS, $l + A \longrightarrow l' + X$, can be written as convolution of parton densities and hard-scattering cross

section;

$$F_A^\lambda(x,Q^2) = \sum_i \int_x^1 \frac{dy}{y} f_A^i(y,\mu_F,\mu)\, \hat{F}_A^\lambda\left(\frac{x}{y}, \frac{Q}{\mu}, \frac{\mu_F}{\mu}, \alpha_s(\mu)\right) \tag{2.28}$$

where f_A^i is the distribution of parton q_i in the hadron A and $\hat{F}_A^\lambda$ is the hard cross section, $\gamma^*(q,\lambda) + q_i \longrightarrow X$, which can be obtained from perturbative calculation. The factorization scale, μ_F, separates the perturbatively calculable and non-calculable region. The scale μ is the renormalization scale which defines the boundary between the finite and the divergent contributions in the renormalization procedure. If the perturbative calculation is performed at all order, the results do not depends on μ_F nor μ, so that they can be arbitrary chosen. In the finite order calculation, there is a dependence on scale. In DIS, Q^2 is usually chosen as a scale.

Which scheme is used to absorb the divergence should be also chosen. The commonly used scheme is $\overline{\text{MS}}$ (modified minimal subtraction) scheme and another scheme useful for the deep inelastic scattering is the DIS scheme.

2.5 QCD improved parton model

The naïve QPM should be modified in the QCD since quarks emit gluons and gluons split into quark pairs or gluons. It introduces the Q^2 dependence to the parton distribution functions (PDFs), $q(x,Q^2)$ or $g(x,Q^2)$ for quarks or gluons respectively. With higher Q^2, which means finer spatial resolution, more quarks or gluons with low x are recognizable by the interaction and hence the number of quarks or gluons at low x increases with Q^2. This Q^2 dependence is usually referred as Q^2 evolution.

2.5.1 DGLAP evolution equation

The Q^2 evolution of parton distributions can be predicted within pQCD by the Dokshitzer-Gribov-Lipatov-Altarelli-Parisi (DGLAP) [4, 5, 6, 7] evolution equation.

$$\frac{dq(x,Q^2)}{d\ln Q^2} = \frac{\alpha_s}{2\pi}\int_x^1 \frac{dy}{y}\left(q(y,Q^2)P_{qq}\left(\frac{x}{y}\right) + g(y,Q^2)P_{qg}\left(\frac{x}{y}\right)\right) \tag{2.29}$$

$$\frac{dg(x,Q^2)}{d\ln Q^2} = \frac{\alpha_s}{2\pi}\int_x^1 \frac{dy}{y}\left(\sum_q q(y,Q^2)P_{gq}\left(\frac{x}{y}\right) + g(y,Q^2)P_{gg}\left(\frac{x}{y}\right)\right) \tag{2.30}$$

where $P_{ij}\left(\frac{x}{y}\right)$ is the *splitting function*, which are calculable in the pQCD and represent the probability of that a parton i with the momentum fraction x is emitted by a parton j with the larger momentum fraction y ($y > x$). In both equations, the first term corresponds to gluon radiation from a quark ($q \longrightarrow qg$ or gq) and the second term corresponds to gluon splitting ($g \longrightarrow qq$ or gg) and they are integrated over the partons with momentum fraction higher than x.

The DGLAP equation is formally derived in the Leading Logarithm Approximation (LLA), where the terms of $(\alpha_s \ln(Q^2))^n$ are summed up to all orders. These $(\alpha_s \ln(Q^2))^n$ terms correspond to the ladder diagrams with n gluons emission as shown in Fig.

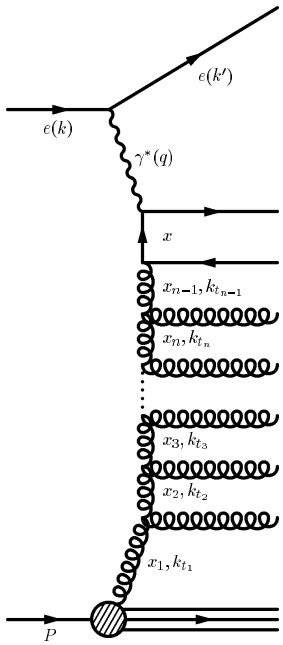

Figure 2.2: Ladder diagrams.

2.2. The LLA approximation is that the emissions are strongly ordered by transverse momentum of gluons k_T as

$$Q^2 \gg k_{T_n}^2 \gg \cdots \gg k_{T_2}^2 \gg k_{T_1}^2. \tag{2.31}$$

The approximation is valid for the large Q^2 region and not too small x region, where $\alpha_s(Q^2) \ln \frac{1}{x} \ll \alpha_s(Q^2) \ln(Q^2)$.

2.5.2 Scaling violation of F_2

The Q^2 dependence of the parton distribution indicates that Bjorken scaling is no longer valid. F_2 decreases at high x and increases at low x as Q^2 increases, reflecting that more quarks with small x are resolved by virtual photons with larger Q^2.

In the DIS factorization scheme, F_2 can be written as

$$F_2(x, Q^2) = \sum_i e_i^2 \left[x q_i(x, Q^2) + x \bar{q}_i(x, Q^2) \right]. \tag{2.32}$$

Therefore, the DGLAP equation gives

$$\frac{\partial F_2(x, Q^2)}{\partial \ln Q^2} = \frac{\alpha_s}{2\pi} \int_x^1 \frac{dy}{y} \left(F_2(y, Q^2) P_{qq}\left(\frac{x}{y}\right) + 2\bar{e}^2 x g(y, Q^2) P_{qg}\left(\frac{x}{y}\right) \right), \tag{2.33}$$

where $\bar{e}^2 = \sum_i e_i^2$. At low x ($x < 0.01$), the contribution from the P_{qq} term is negligible [8] so that the Q^2 dependence of F_2 can be written as

$$\frac{\partial F_2(x, Q^2)}{\partial \ln Q^2} \propto \alpha_s P_{qg} x g, \tag{2.34}$$

which shows indirect sensitivity to gluon PDF.

The scaling violation is observed by many experiments. At HERA, which covered so far the widest kinematic range in both x and Q^2, steep rise of F_2 as increase of Q^2 at low x is seen as shown in Fig. 2.3.

2.5.3 Longitudinal structure function F_L

In the naïve QPM, $F_L = 0$ since scattering between a spin-$\frac{1}{2}$ particle and a longitudinal photon cannot conserve helicity and angular momentum simultaneously as drawn in Fig. 2.4. However, in the QCD, existence of gluon make it possible to give non-zero F_L through gluon emission or splitting. From its nature, F_L has direct sensitivity to the gluon emission inside the proton, i.e. dynamics in the proton.

In the pQCD framework, F_L at LO is given as [10, 11]

$$F_L(x,Q^2) = \frac{\alpha_s}{4\pi}x^2 \int_x^1 \frac{dz}{z^3}\left[\frac{16}{3}F_2(z,Q^2) + 8\sum_q e_q^2\left(1-\frac{x}{z}\right)zg(z,Q^2)\right], \tag{2.35}$$

where the last term includes gluon PDF.

2.6 DIS at low x

HERA, the ep collider, had brought the widened kinematic region for DIS analysis comparing to the fixed target experiments. The accessible region is expanded by about two orders towards both high Q^2 and low x. The DIS cross sections measured at HERA shows steep rise at low x and reveals that the pQCD view can describe the measurements. From the QCD analysis based on the DGLAP equations, the PDFs are determined. At low x, the strong rise of gluon PDF is obtained as seen in Fig. 2.5, which shows the PDFs from the experiments at HERA [12, 13]. PDF determination is done by several groups and their PDFs reasonably agree. However, there is still room for discussion in the pQCD approach.

2.6.1 Description of low x physics

At small x, the terms of $(\alpha_s \ln\frac{1}{x})^n$ cannot be neglected so that the DGLAP equations may fail to describe the data. There are other approaches to describe the low x physics.

At moderate small x, the Double Leading Logarithm Approximation (DLLA) can be used. In the DLLA, the terms of $(\alpha_s \ln\frac{1}{x}\ln(Q^2))^n$ are summed up.

For description of further small x, the Balitskii-Fadin-Kuraev-Lipatov (BFKL) equation was developed. In the BFKL equation, the ordering by k_T is no longer needed but the strong ordering by x, the momentum fraction of emitted gluon is required

$$x_1 \gg x_2 \gg \cdots \gg x \tag{2.36}$$

to sum up the terms of $(\alpha_s \ln\frac{1}{x})^n$. The BFKL equation predicts steeper increase of F_2, hence gluons, at low x than the DGLAP equation.

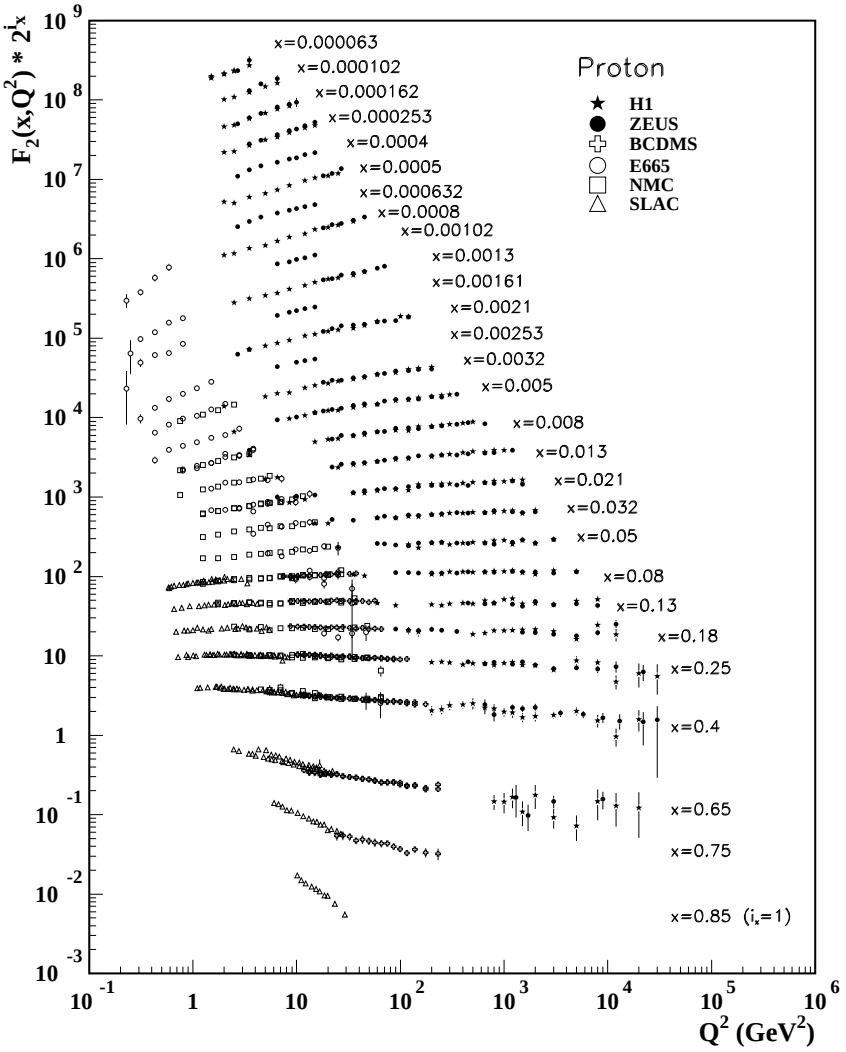

Figure 2.3: F_2 from HERA and other fixed target experiments as a function of Q^2. This plot is taken from [9].

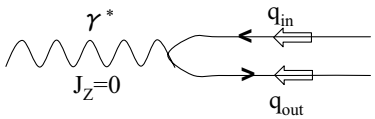

Figure 2.4: $\gamma^* q$ interaction in QPM. Helicity and angular momentum cannot be conserved simultaneously.

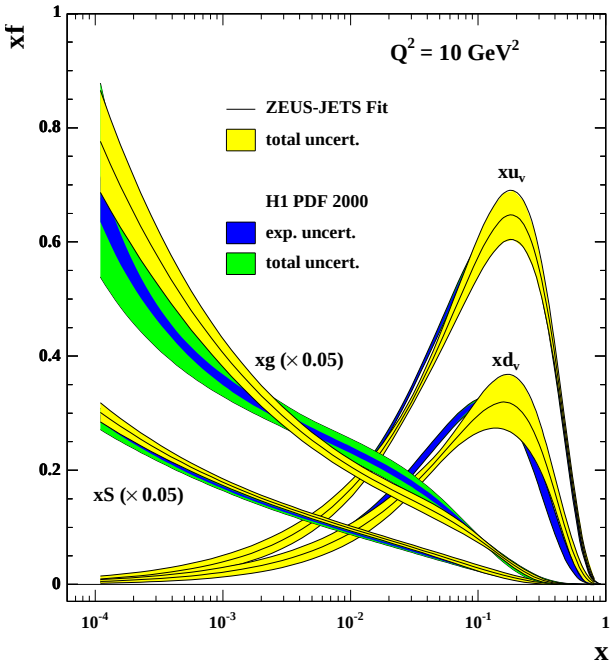

Figure 2.5: ZEUS-JETS PDF and H1 2000 PDF.

The different approaches are summarized in Fig. 2.6. With very low Q^2, perturbation cannot work due to the large value of $\alpha_s(Q^2)$. The high density of gluon distribution at very low x may saturate due to recombination or annihilation of gluons.

2.6.2 F_L at low x

In the PDF determination, the gluon PDF is mainly determined from scaling violation of F_2, which has indirect sensitivity to the gluon PDF as described in Sec. 2.5.2. However, Eq. 2.34 shows that the scaling violation is a convolution of the splitting function P_{qg} and the gluon PDF. Any extension on P_{qg}, which is usually calculated from NLO DGLAP, will be absorbed by the gluon PDF by modifying its shape. Measurement of variable with different sensitivity to the gluons is necessary for cross check of P_{qg} and the gluon distribution, which means the test of current understanding by the pQCD description.

One of such variables is F_L. According to the QCD, F_L directly reflects gluon dynamics in the proton. As seen in Eq. 2.35, the pQCD description of F_L, its sensitivity to the gluon PDF is in different manner as the scaling violation.

However, the measurement of F_L is not easy and the experimental results are limited. As seen in the Eq. 2.17, the separation of F_2 and F_L needs DIS cross sections at the same (x, Q^2) but the different y, which requires measurements at different center-of-mass energies. In the past F_2 measurements at HERA, the F_L contribution to the cross section was subtracted by using model predictions.

In the past fixed target experiments [14, 15, 16, 17], the direct measurements of F_L

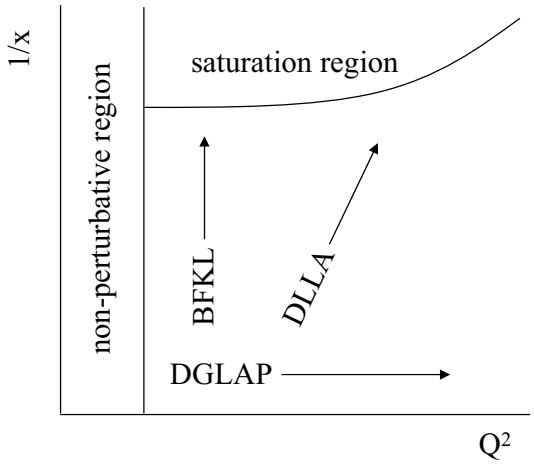

Figure 2.6: Approaches on the $(Q^2, \frac{1}{x})$ plane.

had been done in the form of

$$R = \frac{\sigma_L}{\sigma_T} = \frac{\frac{4M^2x^2}{Q^2}F_2 + F_L}{F_2 - F_L} \tag{2.37}$$

$$\cong \frac{F_L}{F_2 - F_L}, \quad (Q^2 \gg M^2) \tag{2.38}$$

where M is the proton mass. These results are shown in Fig. 2.7 [17]. These measurements are at relatively high x where the sensitivity to the gluon physics is small.

At HERA, the inclusive cross section measured by the H1 collaboration [18] showed turnover in $\tilde{\sigma}$ at low x, implicitly indicating non-zero F_L contribution to the cross section. Nevertheless, a study on such turnover has limited precision and the direct measurement of F_L is necessary for the consistency check of the pQCD.

Various predictions of F_L have been done as summarized in [19]. In addition to the predictions using NLO or NNLO pQCD, there are also predictions with corrections beyond the fixed order pQCD, such as $\ln\frac{1}{x}$ resummation (or BFKL enhanced model), higher twist correction and color dipole model. Comparison of predictions is shown in Fig. 2.8 for $x = Q^2/35420 \sim 2.8 \times 10^{-5} \cdot Q^2$. The differences between the predictions are sizable at very low Q^2, but not so large at $Q^2 \gtrsim 10$ GeV^2.

The F_L measurement requires to collect DIS events at high y. The measurement of such events is difficult and gets more difficult for lower Q^2. In this thesis, by using a newly developed tool to increase the purity of DIS events, the measurement goes down to $Q^2 \simeq 20$ GeV^2. F_L is separated from the measured DIS cross sections for the first time at low x without model dependence. It is done for $24 \leq Q^2 \leq 110$ GeV^2 to perform consistency check of the pQCD description of the proton structure.

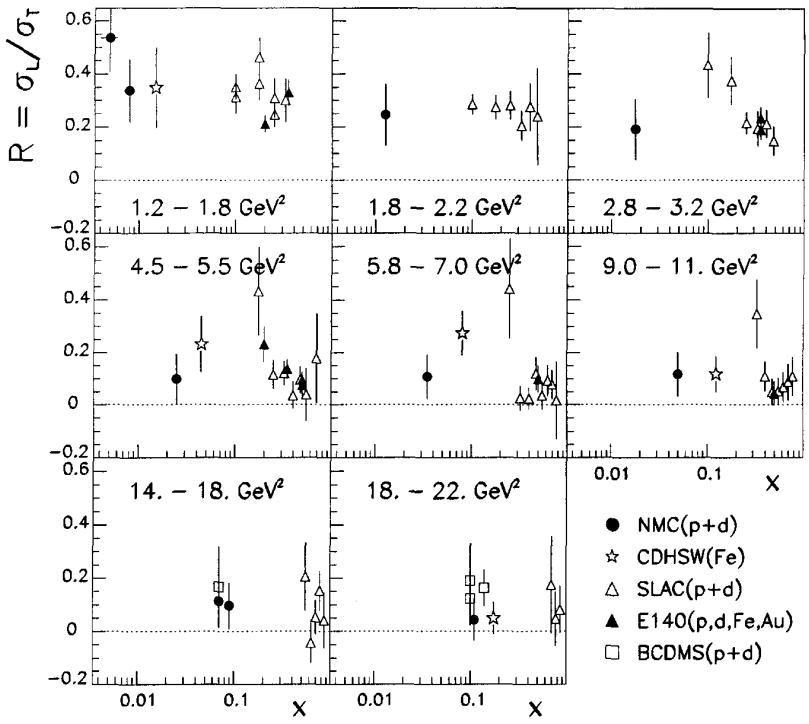

Figure 2.7: R measured by various fixed target experiments. The plot is taken from [17].

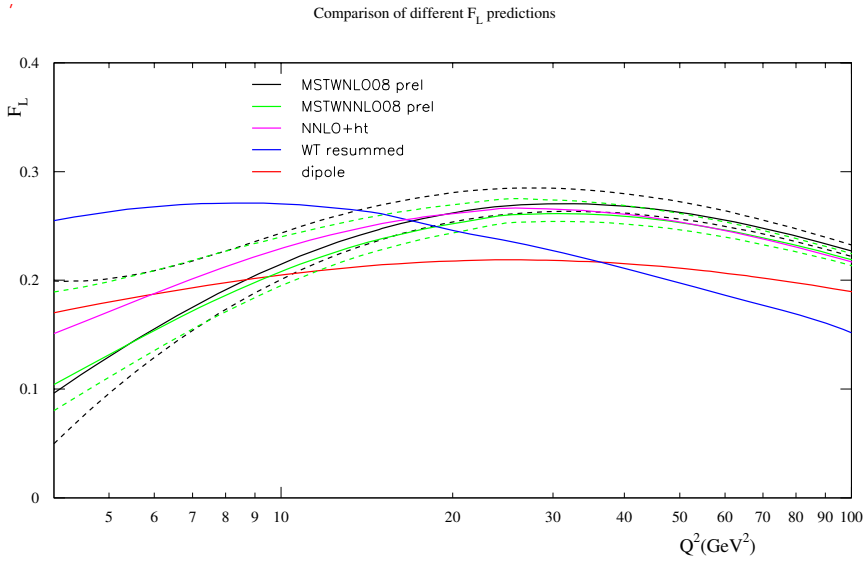

Figure 2.8: Comparison of different F_L predictions. The plot is taken from the slides of [19]. It is shown for $x = Q^2/35420 \sim 2.8 \times 10^{-5} \cdot Q^2$.

Chapter 3

Experimental setup

3.1 The HERA Collider

HERA (Hadron Elektron Ring Anlage) is located at the research center DESY in Hamburg, Germany. It was the unique accelerator in the world which collides electrons or positrons with protons and was in operation from 1992 to the end of June in 2007. Its center of mass energy was 318 GeV from 1998 with the electron energy of 27.5 GeV and the proton energy of 920 GeV. The luminosity upgrade took place from 2000 to 2002.

A schematic view of HERA is shown in Fig. 3.1. Protons are first accelerated in the form of H^{-1} by the linear accelerator (LINAC) to 50 MeV. After electrons are stripped off, protons are accelerated to 7.5 GeV at DESY III and then to 40 GeV at PETRA. Finally they are injected to HERA and accelerated to their final energy. Acceleration of electrons or positrons starts at LINAC I or II, respectively, to 220 MeV for electrons and to 480 MeV for positrons. They are subsequently accelerated by DESY II to 7.5 GeV and by PETRA II to 12 GeV and then injected to HERA. In HERA, the proton ring uses superconducting magnets while the electron ring uses normal conducting magnets. Both beams have bunch structure with 96 ns bunch spacing, resulting a bunch crossing rate of 10.4 MHz. The nominal parameters of HERA are shown in Table 3.1.

	electron	proton
Circumference of the ring	6336.83m	
Number of bunches (incl. empty bunches)	180	
Number of colliding bunches	174	
Time between bunch crossings	96ns	
Center of mass energy	318GeV	
Beam energy	27.5GeV	920GeV
Maximum current	58mA	140mA
Luminosity	$7.4 \cdot 10^{31}\text{cm}^{-2}\text{sec}^{-1}$	

Table 3.1: Parameters of HERA after 2005.

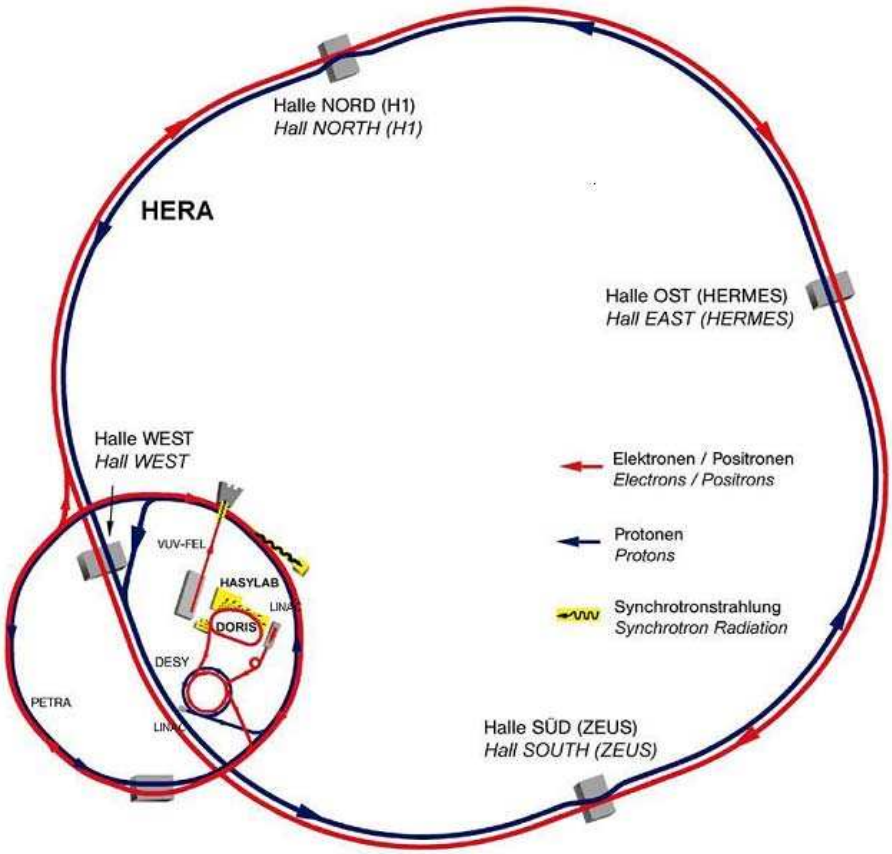

Figure 3.1: A schematic view of HERA.

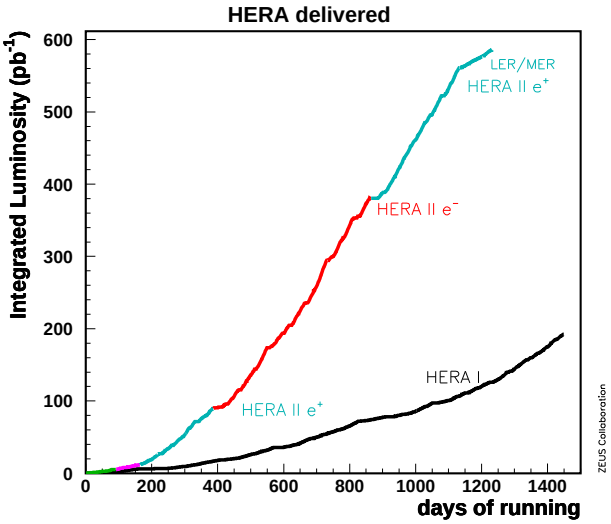

Figure 3.2: Integrated luminosity delivered by HERA. The periods before and after the luminosity upgrade are called HERA I and HERA II.

Four experiments were in operation at HERA. H1 and ZEUS were collider experiments located at Hall North and Hall South, respectively. HERA-B and HERMES are fixed target experiments using the proton beam and the electron beam, respectively.

Before the end of HERA, HERA was operated with lowered proton beam energies which give the opportunity for the direct measurement of F_L. While positron beam energy was kept as 27.5 GeV, the proton beam energies were 460 GeV in the first two months and 575 GeV in the last month. These operations are referred as the Low Energy Running (LER) and as the Medium Energy Running (MER), respectively, in this thesis. In contrast, operation with the nominal energy of 920 GeV is now called as the High Energy Running (HER).

The integrated luminosity which was delivered by HERA during its whole operation is shown in Fig. 3.2.

3.2 The ZEUS Detector

The ZEUS detector [20] is a multipurpose detector, designed to measure particles from ep collision. It surrounds an ep interaction point almost hermetically. A schematic view of the ZEUS detector is shown in Fig 3.3.

The ZEUS coordinate system is a right-handed system defined with respect to the nominal interaction point. The direction of the proton beam is taken as the positive z direction. The positive x direction is horizontal direction pointing the center of the HERA ring and the y direction is pointing upwards. Since ep system is boosted towards the proton direction, the positive z direction is also referred to as the $forward$ direction while the negative z direction is called the *rear* or *backward* direction. The polar angle θ is measured with respect to the proton beam direction and the azimuthal angle ϕ is measured with respect to the positive x direction.

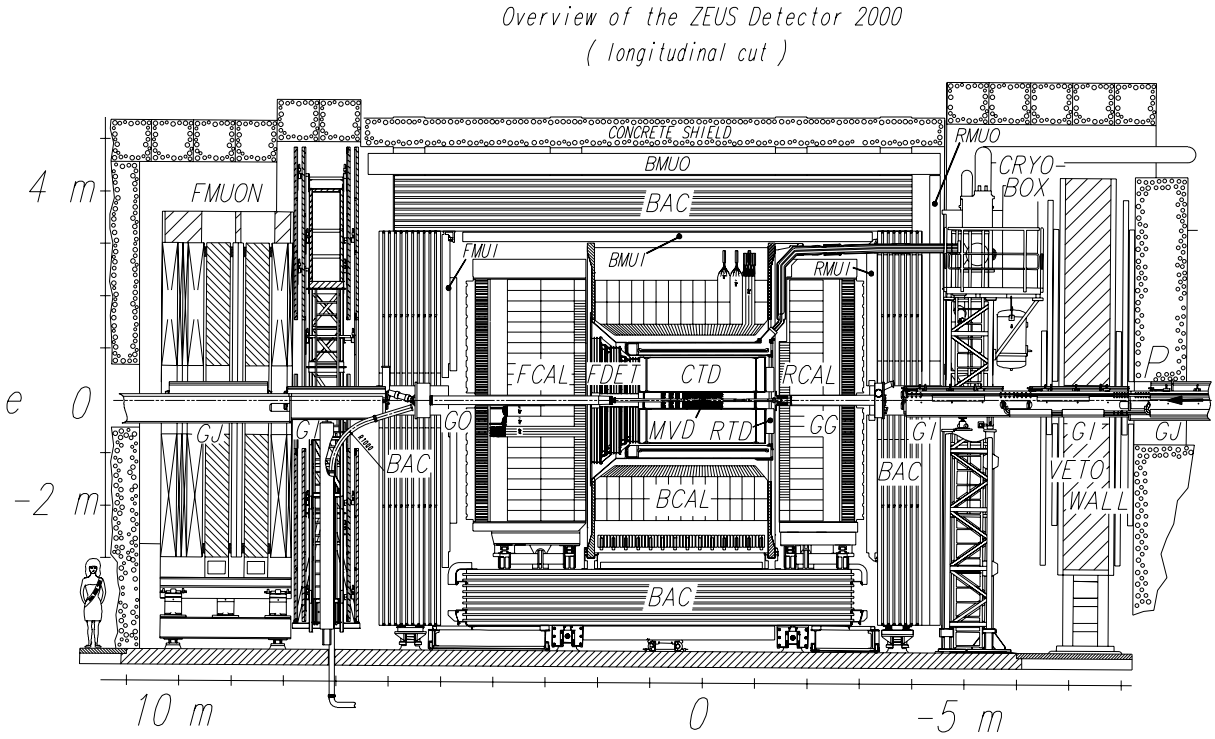

Figure 3.3: The ZEUS detector along the beampipe. In this figure, the left side is the forward direction and the right side is the rear direction.

From the inner part to the outer, the ZEUS detector has a tracking system, a calorimeter and a muon detecting system. In the barrel region, a superconducting solenoid coil surrounding the tracking system provides a magnetic field of 1.43 T. The tracking system consists of the Microvertex Detector (MVD), the Central Tracking Detector (CTD) and the forward detector (FDET) which contains the Straw Tube Tracker (STT) with the interleaved Transition Radiation Detectors (TRD). The uranium-scintillator calorimeter (CAL) is placed surrounding the tracking system and the solenoid and is divided into three sections namely Rear, Barrel and Forward calorimeters (RCAL, BCAL and FCAL). It is equipped with sub-detectors such as silicon pads called Hadron-Electron-Separators (HES) and scintillator tiles called Presampler (PRES). The Small Angle Rear Tracking Detector (SRTD) is attached to the front face of the RCAL around the beam pipe. Outside the CAL, iron yokes are used as the absorber for the Backing Calorimeter (BAC). The wire chambers for muon detection (BMUON, RMUON and FMUON) are at the inner side and the outer side of the BAC. At the rear side of the main detector, the Veto Wall, which consists of an iron wall with scintillator hodoscopes on both sides, rejects background particles from the proton beam halo. The C5 counter, which is a small scintillator counter located at $z = -1.2$m around the beam pipe, monitors the beam condition and is used to veto beam gas events. In downstream of the electron beam, several detectors are situated. The 6m tagger tags electrons escaped through the beam pipe. Two kinds of luminosity monitors are placed at $z \simeq -100$m, namely the Photon Calorimeter (PCAL) and the Spectrometer (SPEC).

In the following sections, further details of the detector components important for this analysis are described.

3.2.1 The microvertex detector (MVD)

The MVD [21] is a detector using silicon strip sensors and consists of the Barrel (BMVD) and the Forward (FMVD) sections. A schematic cross section along the z direction of the MVD is shown in Fig. 3.4. The BMVD has a 3-layer structure and the FMVD consists of 4 wheels. The MVD takes its place from $z = -33$cm to $z = 75$cm within the radius of 16.2 cm. The length of the BMVD and the FMVD are 65 cm and 43 cm, respectively. The coverage in polar angle is from 7° to 160°.

Sensors of the MVD are single-sided detectors made of n-type silicon of 300 μm active thickness with implanted p^+ strips. Capacitive charge division is used and the readout pitch is 120 μm with 5 intermediate strips giving 20 μm strip pitch. The spatial resolution of a sensor is $20 \sim 30\mu$m.

In the BMVD, each sensor has a square shape of 6.4 cm $\times$ 6.4 cm with 512 readout strips which run parallel to a side of a sensor. Two sensors with their strip directions perpendicular to each other form a Half Module (HM) as shown in Fig. 3.5. Two strips in different sensors are read together, which leads to existence of ghost hit. Two mirror-shaped HMs are put together and form a module. Five modules are placed in a line and form a ladder. In total, 30 ladders, which correspond to 600 sensors, are placed parallel to the beam pipe in the BMVD. Their arrangement is shown in Fig. 3.6. Due to the elliptic shape of the beam pipe, which is not centered, the first layer in

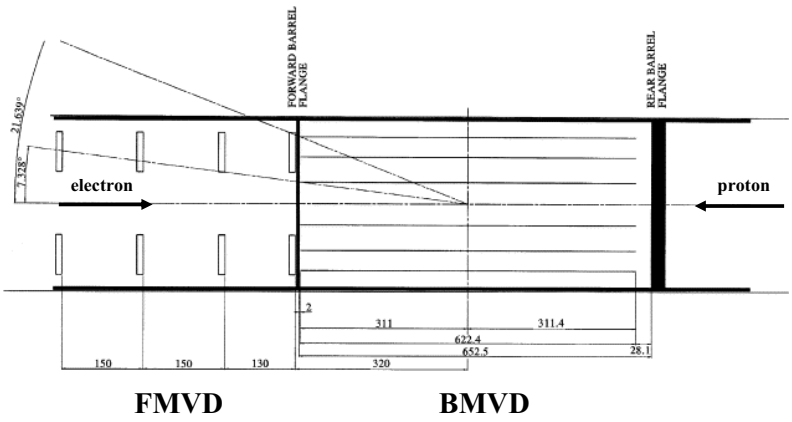

Figure 3.4: The cross section of the MVD along z direction.

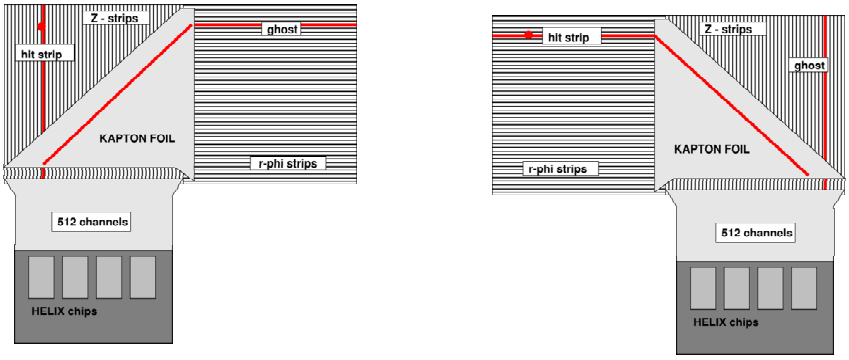

Figure 3.5: Half Modules in the BMVD.

the BMVD is not symmetric resulting some angular regions covered by 2 layers only.

The sensors in the FMVD have a trapezoidal shape with a base of 6.4 cm, a height of 7.4 cm and a tilt of a side of $\pm 13°$. Some of the sensors have a shorter height of 4.9 cm due to their location. Each sensor has 480 strips and they run parallel to one of the tilted sides. A sensor forms a HM and two sensors with oppositely tilted strips are overlapped and form a module. A wheel consists of 14 modules arranged to surround the beam pipe. The FMVD consists of 4 wheels corresponding to 112 sensors in total.

3.2.2 The central tracking detector (CTD)

The CTD [22] is a cylindrical drift chamber with 72 radial layers of sense wires. A cross section of an octant of the CTD is shown in Fig. 3.7. The layers are organized in 9 superlayers (SL) of cells, each containing 8 sense wires. The wire plane in each cell is rotated by 45° with respect to the radial direction adapted to Lorentz Angle of the CTD. The SLs are numbered as from 1 to 9 from the inner side. Wires in the SLs with

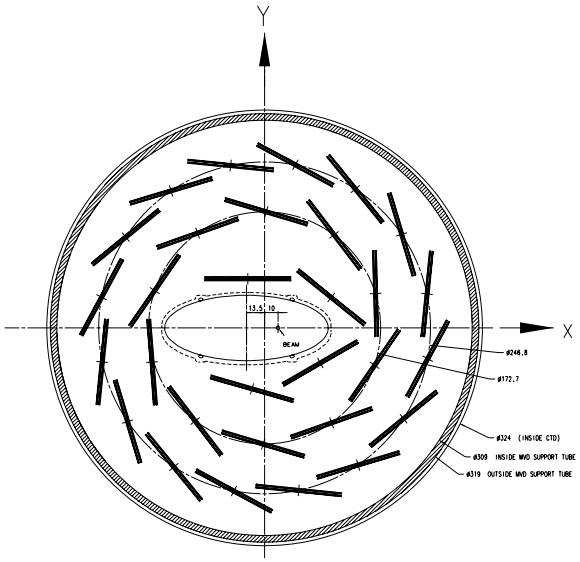

Figure 3.6: The arrangement of the ladders in the BMVD.

SL	1	2	3	4	5	6	7	8	9
Center radius of a cell (cm)	21	27	35	41	49	56	63	69	77
Number of cells	32	40	48	56	64	72	80	88	96

Table 3.2: Radii of CTD SLs.

odd number are parallel to the beam axis, while those in the SLs with even number are tilted with respect to the beam axis by approximately ± 5 to provide a stereo view to determine the z position of a track.

The CTD covers the polar angle region of $15^\circ < \theta < 164^\circ$ ($19^\circ < \theta < 160^\circ$ when requiring the track to pass the third layer) from the nominal interaction point. The active volume extends from $z = -1.00$m to $z = 1.05$m with the inner and outer radii of 18.2 cm and 79.4 cm, respectively. The center radius of each SL is shown in Table 3.2.

The CTD tracking resolution is parameterized as $\sigma(p_T)/p_T = 0.0058 p_T \oplus 0.0065 \oplus 0.0014/p_T$ [23], where p_T is transverse momentum of a track in GeV, for tracks fitted to the event vertex and passing all the 9 SLs. The first term in the right hand side derives from the position resolution of hits and the second and the last terms are coming from multiple scattering inside and before the CTD, respectively. The spatial resolution for a track passing all the 9 SLs is $\sim 180\mu$m in $r\phi$ direction and ~ 2mm in z direction.

The z position of a hit can be also given by the difference in signal arrival time at the ends of a wire. All the wires in SL 1 and half of the wires in SL 3 and 5 are equipped with special electronics to measure the time difference. The system is called as the z-by-timing system. Though the position resolution is not precise, about 4 cm, it performs a fast measurement of the z position. The information from the z-by-timing

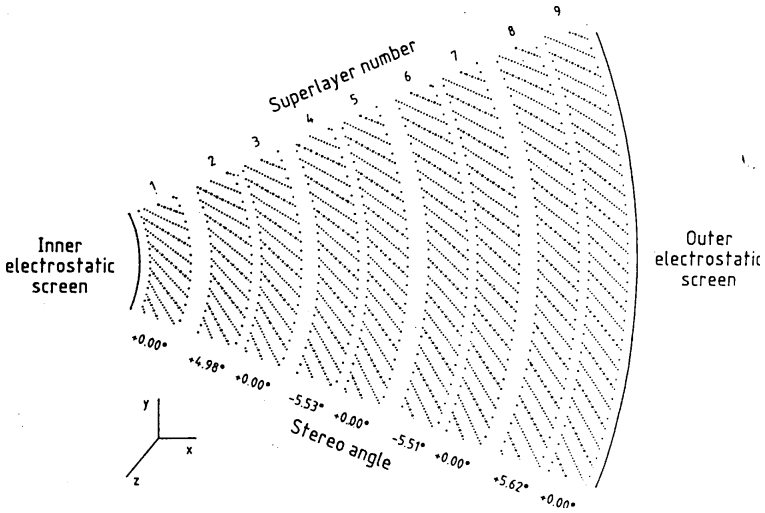

Figure 3.7: The cross section of an octant of the CTD.

is mainly used in the ZEUS trigger system but also in offline tracking.

The CTD gives the reference frame of the ZEUS coordinate system. Other detectors are aligned to the CTD.

3.2.3 The uranium-scintillator calorimeter (CAL)

The calorimetry [24, 25] for the ep collider physics is required to perform precise measurement of both the scattered electron and the hadronic systems in the final state. To have good hadronic energy resolution, the ZEUS experiment has chosen a uranium-scintillator sampling calorimeter. It consists of alternating plates of depleted uranium (DU) as absorbers and plastic scintillator as active materials for readout. While the calorimeter response to a hadronic shower is usually less than that of an electromagnetic shower, the combination of DU and plastic scintillator compensates the undetected energy in a hadronic shower through the following process. Neutrons produced from the fragmentation of uranium elastically scatter out protons in the scintillator. These protons lead scintillation and hence produce additional signals which " compensate " the undetected energy. By selecting the thickness of each layer as 3.3 mm for DU plate and 2.6 mm for scintillators, the ZEUS calorimeter has achieved the equal response to hadrons and electrons, e/h $= 1.00 \pm 0.03$ for $E > 3$ GeV, where e/h is the ratio of average signal of electron and hadron of the same energy. The energy resolutions were obtained from the test beam study as

$$\frac{\sigma(E)}{E} = \frac{18\%}{\sqrt{E[\mathrm{GeV}]}} \oplus 1\% \text{ for electrons} \tag{3.1}$$

$$\frac{\sigma(E)}{E} = \frac{35\%}{\sqrt{E[\mathrm{GeV}]}} \oplus 2\% \text{ for hadrons.} \tag{3.2}$$

	RCAL	BCAL	FCAL
Angular coverage (degree)	$128.1 - 176.5$	$36.7 - 129.1$	$2.2 - 39.9$
Size of EMC front face (cm $\times$ cm)	20×10	23×5	20×5
Depth (λ)	4	5	7
Depth (X_0)	194	128	109

Table 3.3: The parameters of the CAL.

The plastic scintillator also gives a fine timing resolution, which is important for effective rejection of backgrounds from beam gas interaction or cosmic rays. The timing resolution of the CAL is $0.5 + \frac{1.5}{\sqrt{E[\mathrm{GeV}]}}$ ns.

The CAL is divided into three sections of the Rear, the Barrel and the Forward calorimeters (RCAL, BCAL and FCAL) as shown in Fig. 3.8. They mechanically consist of modules, which are further segmented into units for readout called towers. In the FCAL and the RCAL, modules have 20 cm width in the x direction and are placed parallel to the $y - z$ plane. A schematic view of an FCAL module is shown in Fig. 3.9. The size of a tower is 20 cm $\times$ 20 cm in the $x - y$ cross section and towers are lined with the y direction in each module. Each module is longitudinally separated into an electromagnetic calorimeter (EMC) and a hadronic one (HAC). An FCAL tower has 4 EMC cells with the size of 20 cm $\times$ 5 cm, shorter in y, on its front face and 2 HAC cells with the size of tower, 20 cm $\times$ 20 cm, following behind them. An RCAL tower has 2 EMC cells with the size of 20 cm $\times$ 10 cm and a HAC cell with the size of 20 cm $\times$ 20 cm. The longitudinal thickness of the EMC part is 26 radiation length (X_0) or ~ 1 interaction length (λ). Each HAC cell has a thickness of ~ 3 λ which results in the thickness of 4 λ and 7 λ for RCAL and FCAL, respectively. In the BCAL, 32 modules are arranged parallel to the beam axis and have a wedge shape in transverse cross section. The EMC cells in the BCAL are projective in polar angle with each size of 5 cm in z and 23 cm in $r\phi$ on the front face. The BCAL has 2 layers of HAC cells behind the layer of EMC cells, where 4 EMC cells are connected to a HAC cell. The first layer in a HAC cell has a dimension of 24 cm $\times$ 27 cm. The thickness of the BCAL is $\sim 5\lambda$ with 22 X_0 for EMC layer and 2 λ for each HAC layer. The parameters of each RCAL, BCAL and FCAL are summarized in table 3.3. The CAL has 99.7% coverage of 4π solid angle in total except for holes for the beam pipe in FCAL and RCAL, where each hole has approximately the size of a tower.

The scintillation light is transmitted by wavelength shifters to photomultiple tubes (PMTs). The wavelength shifters are attached to the both sides of each cell and placed between modules so that every cell is read out by 2 PMTs. The impact position of a shower can be known from the imbalance of the signals from the 2 PMTs.

3.2.4 The Hadron-Electron-Separator (HES)

The HES [26, 27] is a detector inserted in the CAL EMC to identify electromagnetic showers. It consists of 20518 silicon pad detectors forming two layers of the HES with one in the RCAL and the other in the FCAL. Each layer covers the radius up to ~ 190

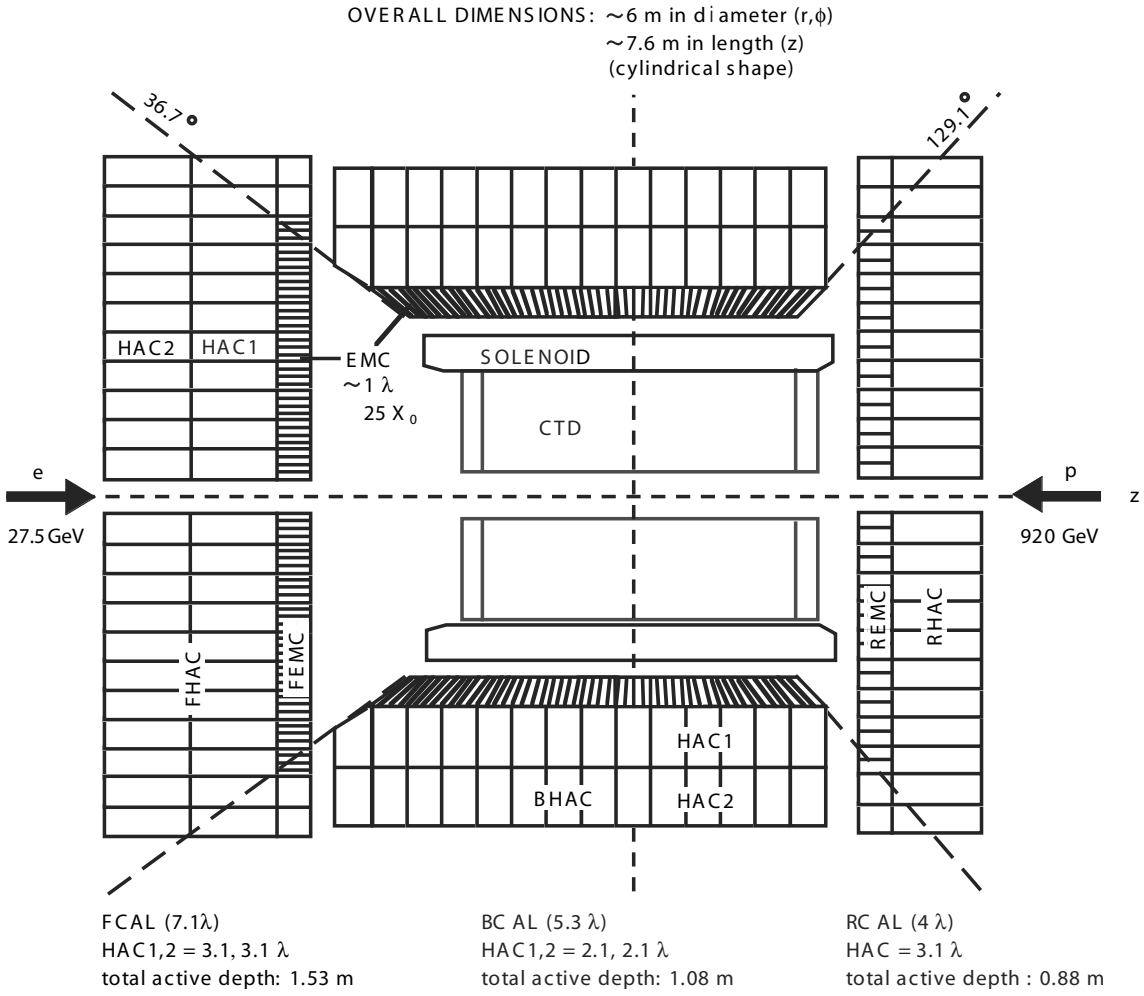

Figure 3.8: The layout of the CAL.

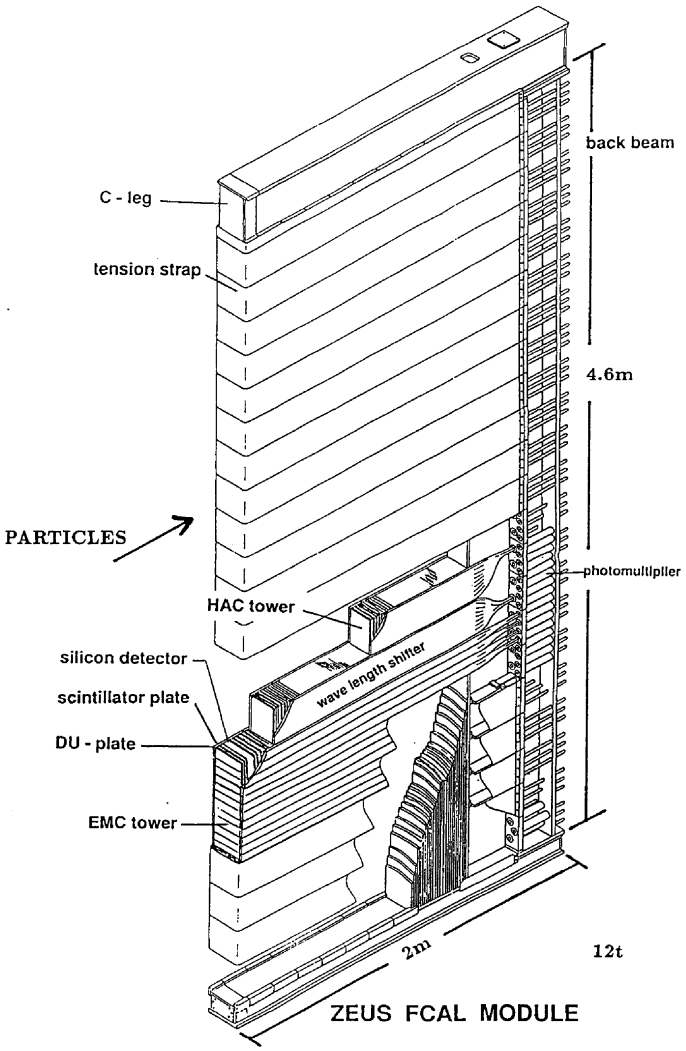

Figure 3.9: A schematic view of an FCAL module.

cm from the beam pipe and is placed at 3.3 X_0 from the CAL surface. It corresponds to the shower maximum position for electromagnetic showers while hadrons behave as MIP particles at the position of the HES. Based on the fact that the Moliere radius of electromagnetic shower in the ZEUS CAL is about 2 cm, the size of a silicon pad was chosen as 3.1 cm $\times$ 3.4 cm with 400 μm thickness. A HES cluster is reconstructed by 3 $\times$ 3 silicon pads with highest energy deposit in its central pad. When a shower hits more than a single pad, the position resolution of the HES is about 0.5 cm.

Pairs of pads are arranged in line on HES skis. Each ski has a width of 6.3 cm. Three skis are installed to a CAL module to fill a gap prepared for the HES. The cross section of a gap is 1.5 cm $\times$ 19 cm.

3.2.5 The small rear tracking detector (SRTD)

The SRTD [28] is a scintillator strip hodescope placed on the RCAL front face. Four quadrants are arranged to surround the beam pipe. Each quadrant has a size of 24 cm $\times$ 44 cm and consists of two planes of scintillator strips, which are 1 cm wide and 0.5 cm thick. The two planes are placed so that strip directions are perpendicular to each other. The position resolution of the SRTD is 3 mm. It has a good timing resolution of 1 ns for MIP and its timing information is used for background vetoes in the trigger system.

3.2.6 The luminosity monitor

The ZEUS experiment was equipped with two independent luminosity monitors since 2003, namely the Photon Calorimeter (PCAL) [29] and the Spectrometer (SPEC) [30]. Both systems measure the rate of high energy bremsstrahlung photons from the Bethe-Heitler process, $ep \longrightarrow e\gamma p$ and are located at the downstream of the electron beam. The cross section of the process is large and is theoretically well known, which minimize both statistical and theoretical uncertainties on the luminosity measurement.

The PCAL system consists of carbon filters, aerogel cerenkov counters [31], and a photon calorimeter. Their setup is shown in Fig. 3.10. The carbon graphite filters work as absorbers and shield the calorimeter from high synchrotron radiation emitted from the electron beam. The thickness of the filters is 4.2 X_0 in total. The silica aerogel cerenkov counters are placed before and behind of one of the filters to improve the calorimeter resolution, which is significantly deteriorated by the filters. With the cerenkov energy threshold for electrons of 1.62 MeV, the counters do not detect photons from synchrotron radiation, which have energy spectrum up to 1-2 MeV, but measure electromagnetic showers from the bremsstrahlung photons since typical energy of their shower particles is about 20 MeV. The photon calorimeter is a sandwich lead-scintillator calorimeter located at $z = -107$m. It consists of 48 layers of lead plates and scintillator plates with the dimension of 20.0 cm $\times$ 20.0 cm. It corresponds to the depth of 24 X_0. After 8 layers from the front, a position detector is inserted to reconstruct the positions of the incoming photons. The position detector is a hodoscope made of two layers of scintillator strips with 1.0 cm wide and 0.3 cm thickness. The length of

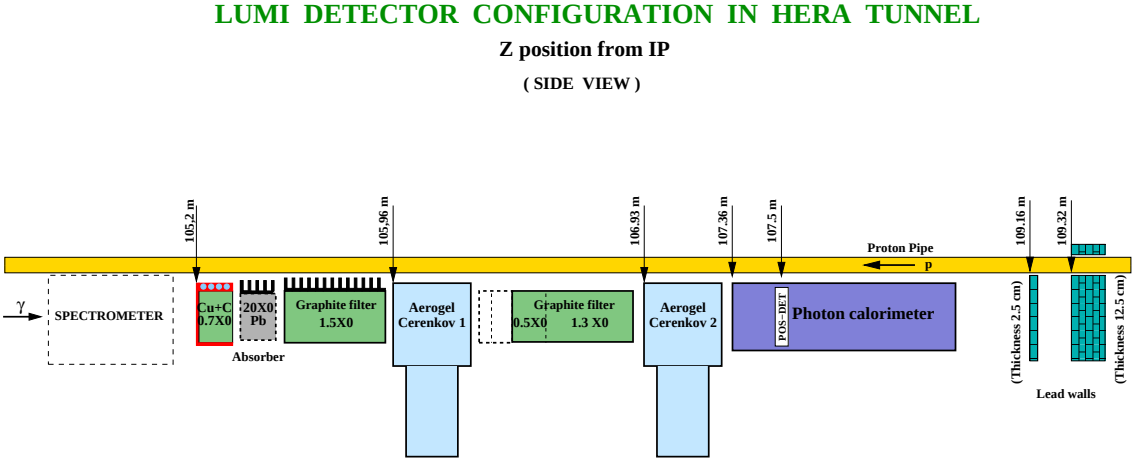

Figure 3.10: The setup of the PCAL system.

the strips is 15 cm for 17 strips running in vertical and 18 cm for 13 strips running in horizontal.

The SPEC system detects the bremsstrahlung photons by measuring electron-positron pairs from their conversion, $\gamma \rightarrow e^+e^-$. A schematic layout of the system is shown in Fig. 3.11. Approximately, 10 % of the photons covert into the electron pairs at the photon exit window, which is located at $z = -92.5$m. The electrons and positrons are split vertically by the dipole magnet and detected by calorimeters below and above the photon beam, respectively. The calorimeters are segmented tungsten-scintillator sampling calorimeters which allow the simultaneous measurement of the impact position and energy of an electron. They consist of 26 tungsten layers with 3.5 mm thickness and layers of scintillator strips. The strips are 7.9 mm wide and 2.6 mm thick and alternates after each layer in x and y direction. The total depth of each calorimeter is 24 X_0. Their energy and position resolutions are $17\%/\sqrt{E}$ and 1 mm, respectively.

The systematic uncertainty on the luminosity measurement is 2.6 %. The measurements from the two systems agree well within the uncertainty.

3.2.7 The 6m tagger

Electrons from the Bethe-Heitler process or the photoproduction process are deflected off the beam electrons by the dipole magnet for the electron beam separation. The 6m tagger [32] is a tungsten scintillator spaghetti calorimeter located at $z = -5.37$m to detect these electrons. It consists of 84 tungsten plates and 1890 fibres and has a size of 85 mm $\times$ 24 mm $\times$ 100 mm. The calorimeter is divided into 70 cells, 14 in x and 5 in y, where each cell has 27 fibres and is read out by a photomultiple tube. The tagger has almost 100 % efficiency for electrons with energy of 4-8 GeV.

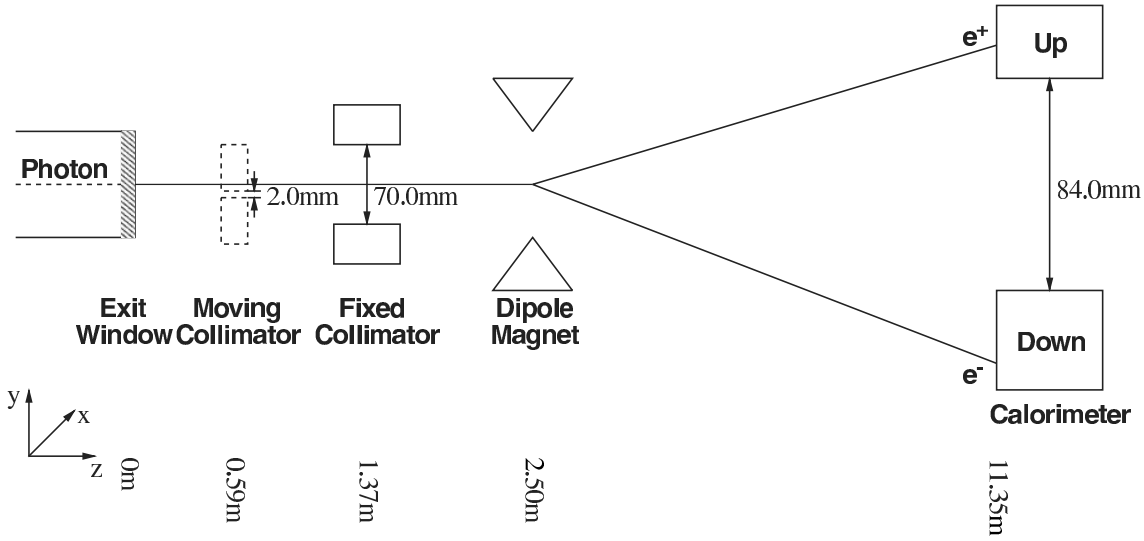

Figure 3.11: The setup of the SPEC system.

3.3 The ZEUS Trigger and data acquisition system

An experiment at HERA is required to have a sophisticated data acquisition system to cope with the short bunch spacing and large backgrounds. While the bunch spacing of 96 ns gives event rate of 10.4 MHz, the rate of ep scattering events to be analyzed is a few Hz. The rate of backgrounds is about 100 kHz. Most of them are caused by interactions between proton beam particles and residual gas molecules in the beam pipe. There are also electron beam gas backgrounds, beam halo and cosmic events.

The ZEUS experiment is equipped with pipeline readout and three-level trigger system [33] to minimize the dead time and to take data efficiently. A schematic diagram of the ZEUS trigger system is shown in Fig. 3.12.

First Level Trigger (FLT)

The FLT is a hardware trigger designed to reduce the event rate to less than 1 kHz. It consists of local FLTs and the Global First Level Trigger (GFLT). Each detector component stores its data in the own pipeline system during the FLT calculation which takes $\sim 5\mu$s. For the first 2μs, local FLTs, the FLTs at the components, make rough calculation on the particular data read for trigger purpose and send the calculated trigger signal to the GFLT. The GFLT collects the signals from all the local FLTs and make a decision whether to take or not using memory lookup tables. The output is 64 bits, where each bit corresponds to a decision for a single logic and called *slot*. These logics can be easily modified via software. The GFLT decision is OR of the 64 slots. If the GFLT makes a positive decision, an accept flag is sent to each detector component and components start to read out the data in the corresponding pipeline.

The GFLT also sends HERA clock to each component to synchronize all the pipeline systems and the local FLTs with the HERA bunch crossings.

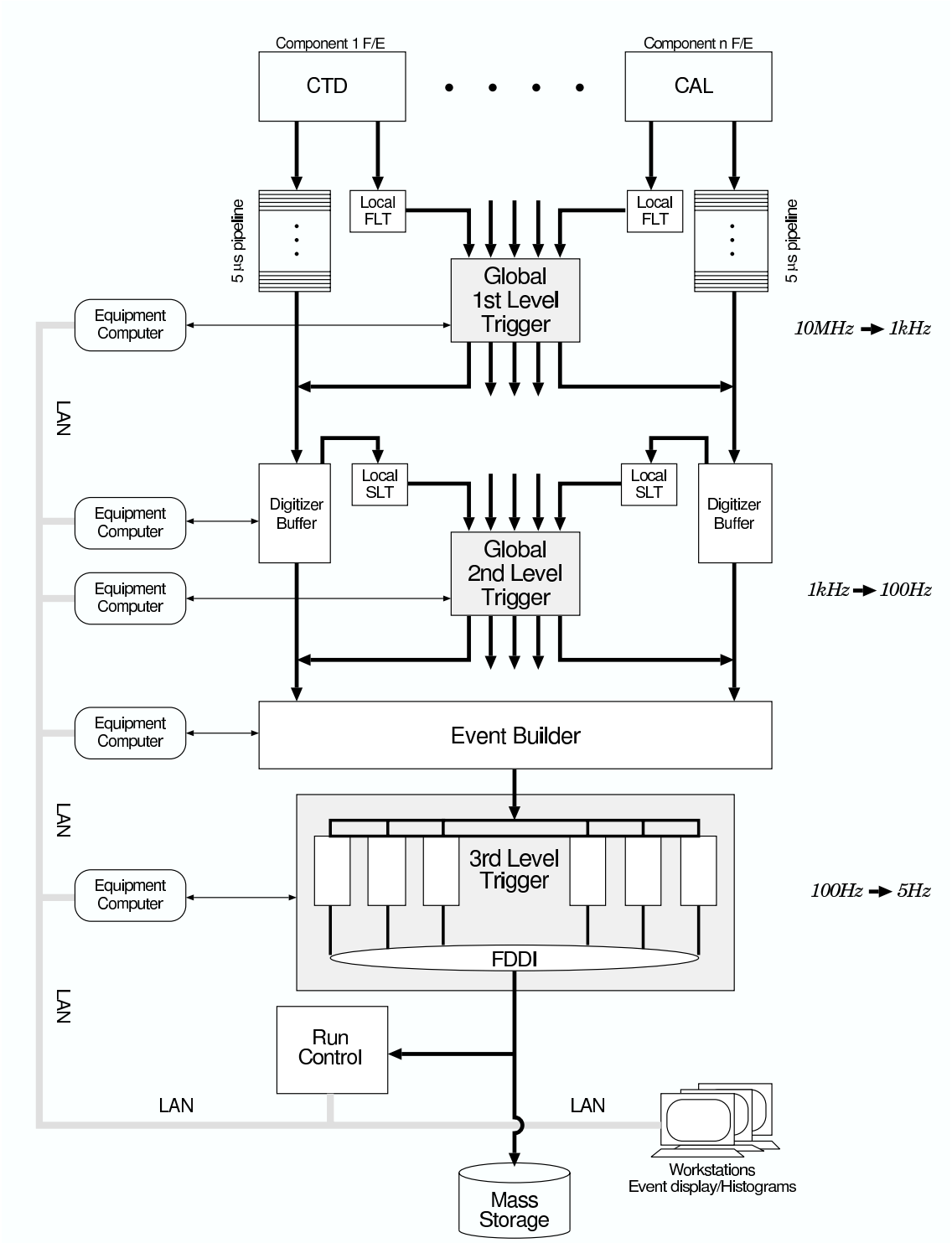

Figure 3.12: A schematic diagram of the ZEUS trigger system.

Second Level Trigger (SLT)

The SLT is a software based trigger running on a network of computers. It reduces the event rate to less than 100 Hz within the available time of $\sim$ 10ms. The SLT also consists of local SLTs and Global Second Level Trigger (GSLT).

The data read out based on the GFLT accept flag is digitized and sent to digitizer buffers which play a similar role as pipelines at the FLT. Each local SLT process the nominal data of its own detector component and sends it to the GSLT. Since all the data from the detectors is available, the GSLT makes the decision based on physics oriented filters with more sophisticated vetoes than the FLT for the background rejection. The number of filters is about up to 100.

If an event is accepted by the GSLT, all the detector components send the data stored in their buffer to the Event Builder (EVB). It constructs the event structure combining all data from the components.

Third Level Trigger (TLT)

The TLT runs a part of the offline reconstruction codes on a PC farm. It selects physics events with the output rate of less than 10 Hz.

The events which are accepted by TLT are sent to Mass Storage and written into tapes. The typical size of a event is about 100 kBytes.

3.4 Monte Carlo simulation

Any detector has limited acceptance and also imperfection in reality. Their effect on the measurement should be well understood for the cross section measurement. The complexity of a detector requires accurate detector simulation for estimation of the acceptance and the smearing effect of the detector.

The Monte Carlo (MC) simulation is used for the estimation. The simulation has two steps, first the event generation and then the detector simulation.

Event generation

In the lepton-proton scattering, the event generation is done through the combination of parton distributions in the proton, hard scattering at the parton level and hadronization.

The DIS events are simulated by DJANGOH1.6 [34] using CTEQ5D PDFs [35]. In the simulation, HERACLES4.6 [36] takes into account of first-order electroweak radiative correction. HERACLES is interfaced to the QCD program, ARIADNE4.12 [37], by DJANGOH. ARIADNE simulates QCD cascades from partons using the color-dipole model. Hadronization is done based on LUND string model of JETSET7.4 [38]. The sample used in this analysis is generated with $F_L = 0$.

The photoproduction MC is used for the background estimation. It was simulated by PYTHIA6.221 [39, 40]. It also uses HERACLES4.6 so that the first-order electroweak radiative correction is included.

E_p (GeV)	Signal MC	N_{events}	$\mathcal{L}$	Background MC	N_{events}	$\mathcal{L}$
920	$Q^2 > 1.5$ GeV^2	20 M	28 pb^{-1}	$y > 0.5$, $Q^2 < 1.5$ GeV^2	20 M	9 pb^{-1}
	$Q^2 > 4$ GeV^2	10 M	29 pb^{-1}			
460	$Q^2 > 1.5$ GeV^2	20 M	33 pb^{-1}	$y > 0.5$, $Q^2 < 1.5$ GeV^2	25 M	13 pb^{-1}
	$Q^2 > 4$ GeV^2	10 M	37 pb^{-1}			
575	$Q^2 > 1.5$ GeV^2	20 M	31 pb^{-1}	$y > 0.5$, $Q^2 < 1.5$ GeV^2	20 M	10 pb^{-1}

Table 3.4: MC samples used in the analysis.

Photoproduction events can be classified in subprocesses according to the interaction. The proportion of each subprocess in the generated photoproduction MC is set to reproduce the measured results by the ZEUS collaboration [41]. While the total cross section is unchanged, the proportion of direct processes is increased and that of diffractive process is decreased.

The both DIS and photoproduction MC includes the diffractive component. The generated samples are summarized in Table 3.4.

Detector simulation

The detector simulation is done by the program MOZART based on GEANT3.21 [42], which includes detector description and simulates detector response. After the simulation of detector response, the trigger simulation is done and the full event reconstruction is applied.

Chapter 4

Measurement and event reconstruction

4.1 Overview of the F_L measurement

As seen in Eq. 2.17, the DIS cross section is formulated as a combination of the structure functions. The reduced cross section $\tilde{\sigma}$ is defined by Eq. 2.18 as

$$\tilde{\sigma} \equiv \frac{1}{Y_+}\frac{xQ^4}{2\pi\alpha^2}\frac{d^2\sigma}{dxdQ^2} = F_2(x,Q^2) - \frac{y^2}{Y_+}F_L(x,Q^2), \tag{4.1}$$

which is to be measured. The separation of the F_L contribution can be done by the comparison of the reduced cross sections with the same (x, Q^2) but the different y. If the reduced cross sections are plotted as a function of $\frac{y^2}{Y_+}$, the slope corresponds to the F_L. Due to the relation of $Q^2 = sxy$, the comparison needs the DIS cross section measurement at the different center-of-mass energies.

The DIS events are identified by the existence of the scattered positron in the detector. In this measurement, the accurate reconstruction of the positron is crucial. To have a large sensitivity to F_L, the measurement should be done at the high y region due to the factor of $\frac{y^2}{Y_+}$, where the scattered positrons have low energy. The interesting region is at low Q^2 which means the scattered angle is also low. However, the accurate identification of the positrons with low energy and low angle is difficult. Misidentification of charged- or neutral- pions as the positrons bring the background contamination to the DIS events. The main background are photoproduction events, in which the almost real photon is emitted from the positron and interacts with the proton. The positron escapes through the beam pipe and is undetected in the main detector. Since its cross section is huge, it may cause a significant amount of background events by the positron misidentification.

The kinematic reconstruction uses the energy and the angle of the scattered positron as described in the next section. The measurement is quite sensitive to the positron reconstruction.

4.2 Reconstruction of kinematic variables

The accurate reconstruction of the kinematic variables x, y and Q^2 is essential for the better measurement of the inclusive cross section. Two of the variables are independent and the rest can be determined by the relation of $Q^2 = sxy$.

In the final state of the scattering, four parameters are measurable, namely the energy and angle of the scattered positron (E'_e, θ_e) and two variables from the hadronic system, $\delta_h = \sum_h (E - p_z)_i$ and $p_{T,h} = \sqrt{\left(\sum_h (p_{x,i})\right)^2 + \left(\sum_h (p_{y,i})\right)^2}$, where the sum $\sum_h$ runs over all particles in the final state except the scattered positron. The particles in the proton remnant little contribute to δ_h nor $p_{T,h}$ since the remnant runs downstream of the proton beam with $E \sim p_z$. The hadronic angle γ_h can be reconstructed from δ_h and $p_{T,h}$ as

$$\cos\gamma_h = \frac{p_{T,h}^2 - \delta_h^2}{p_{T,h}^2 + \delta_h^2}, \tag{4.2}$$

which corresponds to the angle of the scattered quark in the naïve QPM view. Isolines of these measured variables in the (x, Q^2) plane is shown in Fig. 4.1. The variables are shown for $E_p = 920$ GeV. Closer lines in the kinematic plane mean steeper dependence on the variable. In such region, in principle the variable is expected to reconstructs kinematic variables with the better precision. The variables of E'_e and θ_e are shown also for $E_p = 460$ GeV in Fig. 4.2.

There are several methods to reconstruct kinematic variables depending on which variables to use. Three of them are described here.

Electron method

The reconstruction based purely on the variables of the scattered positron is referred as the **Electron method**.

$$y_{el} = 1 - \frac{E'_e}{2E_e}(1 - \cos\theta_e) \tag{4.3}$$

$$Q^2_{el} = 2E_e E'_e (1 + \cos\theta_e) \tag{4.4}$$

The equations show that high y corresponds to low E'_e and low Q^2 corresponds to large θ_e in the ZEUS coordinate, i.e. low scattered angle. The reconstructed values are sensitive to the positron energy scale. This method has a good resolution at the high y region. At the low y region, the reconstruction loses the sensitivity to the E'_e and its resolution deteriorates as seen in Fig. 4.1 (a).

Jacqet-Blondel method

In the **Jacqet-Blondel method** [43], the kinematic variables are reconstructed by hadronic variables only. It is used in the charged-current analysis, where the scattered neutrino escapes from the detector and is not measurable.

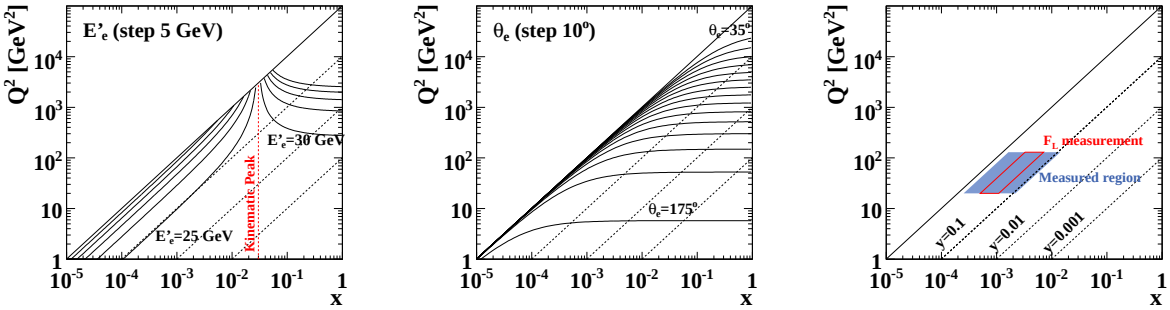

(a) E_e (b) θ_e (c) Measured region

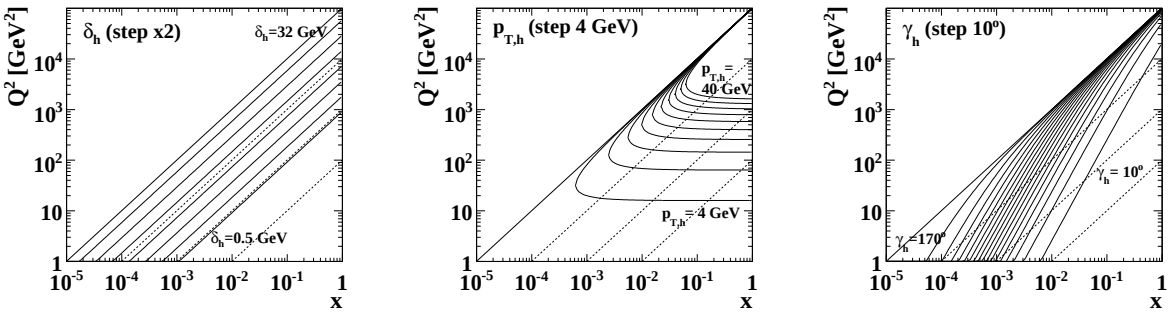

(d) δ_h (e) $p_{T,h}$ (f) γ_h

Figure 4.1: Isolines of measured variables. Dotted lines are isolines of y. They are shown for $E_p = 920$ GeV.

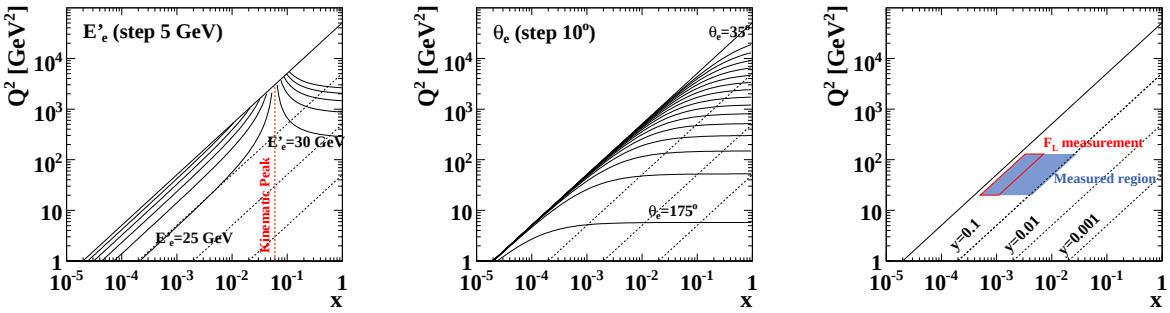

(a) E_e (b) θ_e (c) Measured region

Figure 4.2: Isolines of measured variables. Dotted lines are isolines of y. They are shown for $E_p = 460$ GeV.

$$y_{JB} = \frac{\delta_h}{2E_e} \tag{4.5}$$

$$Q^2_{JB} = \frac{p^2_{T,h}}{1 - y_{JB}} \tag{4.6}$$

The method has reasonably good reconstruction power for y. The Q^2 reconstruction depends on the measurement of $p_{T,h}$, whose accuracy can be easily spoiled by the detector effects such as calorimeter noises, so that the method gives a worse resolution of Q^2 reconstruction comparing to other methods.

Double Angle method

The **Double Angle method** minimizes the sensitivity to the absolute energy scale. It uses the angles of the scattered positron and the hadronic system.

$$Q^2_{DA} = 4E_e^2 \frac{\sin\gamma_h(1+\cos\theta_e)}{\sin\gamma_h + \sin\theta_e - \sin(\gamma_h + \theta_e)} \tag{4.7}$$

$$x_{DA} = \frac{E_e}{E_p} \frac{\sin\gamma_h + \sin\theta_e + \sin(\gamma_h + \theta_e)}{\sin\gamma_h + \sin\theta_e - \sin(\gamma_h + \theta_e)} \tag{4.8}$$

$$y_{DA} = \frac{\sin\theta_e(1-\cos\gamma_h)}{\sin\gamma_h + \sin\theta_e - \sin(\gamma_h + \theta_e)} \tag{4.9}$$

The method performs generally reasonable reconstruction of kinematic variables over the whole kinematic region.

The measurement of E'_e, θ_e, δ_h and $p_{T,h}$ are done during the reconstruction described in the following sections. The E'_e reconstruction is described in Sec. 4.3.2. The θ_e is reconstructed by the positron position and the event vertex, whose reconstructions are described in Sec. 4.3.3 and 4.5.1, respectively. The hadronic four momentum is reconstructed as described in Sec. 4.4.

This measurement is focusing on the high y region. The measured region in this analysis is shown in Fig. 4.1 (c). Figure 4.3 and Figure 4.4 show the bias and the resolutions of the Q^2 and y reconstructed with the Electron method and the Double Angle method in (y, Q^2) bins for the region of $0.1 < y < 0.7$ and $10 < Q^2 < 400\mathrm{GeV}^2$. The bias and resolutions are estimated from the comparison between reconstructed and true values of each Q^2 and y in MC. In both Q^2 and y, the distributions by the Electron method have a peak at 1 and show no significant bias. For the resolution, the Electron method has good Q^2 resolution over the region. The Q^2 resolution from the Double Angle method gets worse at higher y. For the y resolution, the Electron method has a good resolution at high y and gets worse at lower y, where the Double Angle method gives better resolution. In this analysis, the Electron method is adopted for the main kinematic reconstruction. The other methods are used for various checks.

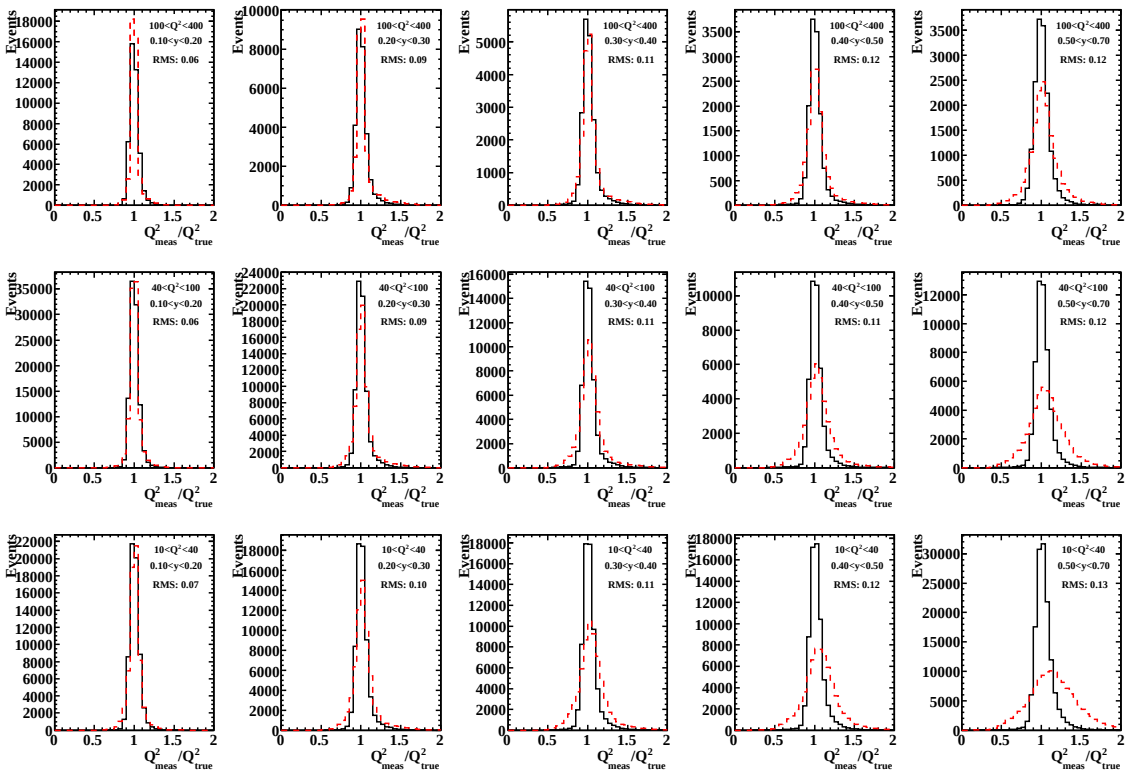

Figure 4.3: Resolution of Q^2. The solid line is for the Electron method and the dashed line is for the Double Angle method. The values of RMS are shown for the Electron method.

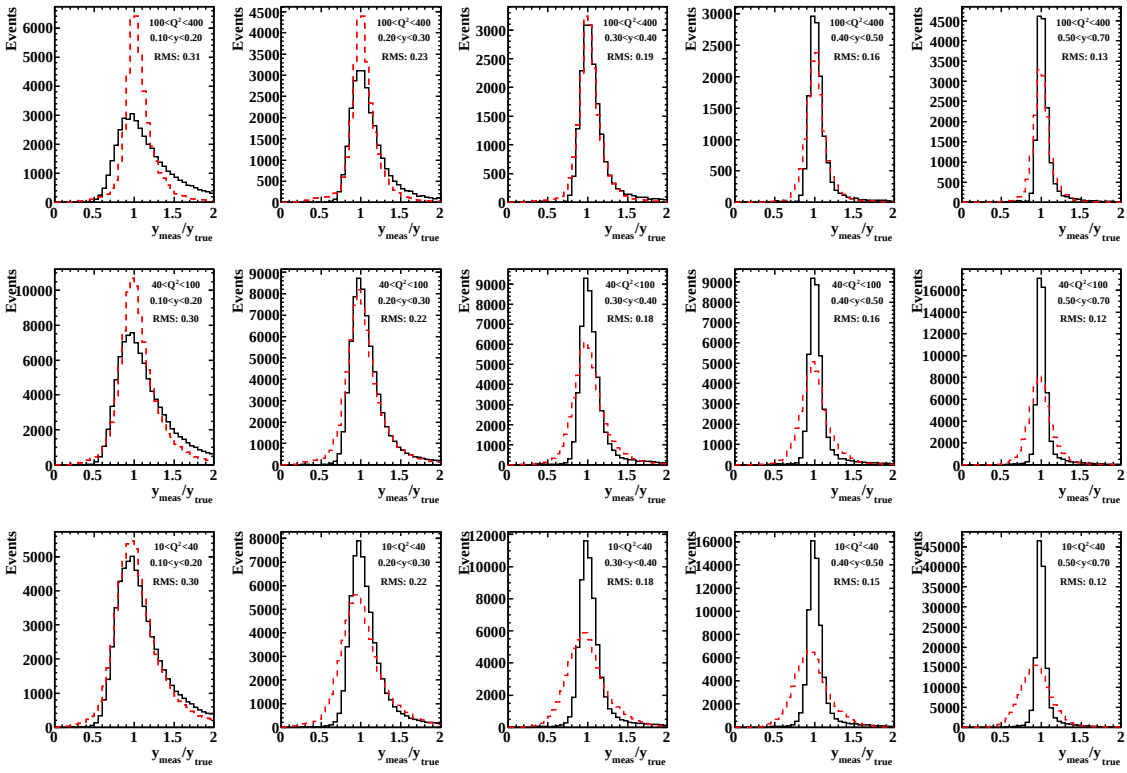

Figure 4.4: Resolution of y. The solid line is for the Electron method and the dashed line is for the Double Angle method. The values of RMS are shown for Electron method.

4.3 Positron reconstruction

4.3.1 Positron finding

A scattered positron creates an electromagnetic shower in the CAL, where most of its energy would be measured in the EMC cells with a small energy leakage to the HAC cells. Once calorimeter cells with energy deposits are clustered into *islands*, finding of candidates for the scattered positron is done by the positron finder SINISTRA [44, 45]. It evaluates the shower profile using a neural network based on calorimeter information. SINISTRA gives an output variable called *probability*, P_{Sira}, which can take the value from 0 (hadron-like) to 1 (positron-like). The probability for the low energy scattered positrons ($E_e < 10\mathrm{GeV}$) gets significantly smaller than 1, since it gets harder to distinguish for showers with lower energy whether it comes from positrons or hadrons. $\pi^{\pm}$ contaminates the distribution of the positrons at the low energy region. In addition, since photons make the similar electromagnetic showers as positrons, it is hard for SINISTRA to exclude photons from $\pi^0 \to 2\gamma$. Their rejection needs tracking information, which is described in Sec. 4.3.4.

4.3.2 Energy reconstruction

Since the Electron method uses the energy of scattered positron, the accurate measurement of positron energy is crucial. The measured energy is deviated from its original energy by energy losses in the inactive materials, non-uniformity of the detector and inadequate understanding of the individual response of each calorimeter cell. The following corrections are applied at the reconstruction.

- RCAL cell-by-cell energy scale correction.
  The energy scale in data is corrected by cell-by-cell basis. The positrons detected well within each cell are used to extract its scale factor. During the extraction, some cells show deficit in their energy distribution and are considered as bad cells. They are masked in this analysis by setting the energy measured in them to zero.

- Non-uniformity correction
  The gaps between the modules and those between the cells cause non-uniform response of the calorimeter. The effect in RCAL is corrected by the product of a x-dependent correction factor and a y-dependent factor which are derived for the MC and the data separately. The upper and lower halves (left and right halves) have different x-dependent (y-dependent) parameters.

- Dead material correction
  Before entering the calorimeter, the scattered positron looses its energy by traveling materials, such as the beam pipe, supporting materials or cables, etc. To compensate this energy loss, the dead material correction is applied. The correction depends on the calorimeter energy and the amount of inactive materials, which is estimated based on dead material map, from the position of the event vertex and the scattered angle.

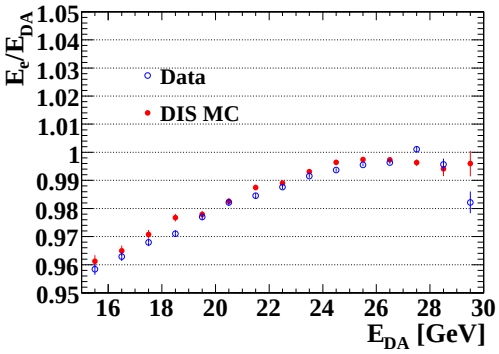

Figure 4.5: Energy calibration. Comparison of the reconstructed energy with the DA energy is shown for both data and DIS MC.

- Low E'_e correction
  Additional low E_e correction,

$$E'_e \longrightarrow 1.015 \cdot (5.5 - E'_e) \cdot E'_e \text{ for } E'_e < 5.5 \text{ GeV},$$

  is applied in the data.

These correction parameters are mainly derived using two different methods, one of which uses Kinematic Peak (KP) events and the other uses Double Angle (DA) energy. In a wide kinematic region around the line of $x = x_0 \equiv E_e/E_p$ ($Q^2 \lesssim 100$GeV and $y \lesssim 0.03$), the energy of scattered positron is close to the positron beam energy and almost independent of x or Q^2 as seen in Fig 4.1 (a). These events form a peak in the E'_e distribution at the positron beam energy and hence called the Kinematic Peak events. These positrons can be used as a reference energy. The DA energy is the energy of the scattered positron estimated from θ_e and γ_h,

$$E'_{DA} = 2E_e \frac{\sin\gamma_h}{\sin\gamma_h + \sin\theta_e - \sin(\gamma_h + \theta_e)}. \tag{4.10}$$

E'_{DA} is an independent estimate of E'_e since the kinematic reconstruction needs only two of the four measured variables. It gives reasonable estimation for the positrons when $E'_e \gtrsim 15$GeV. The reconstructed energy after all the corrections is compared with the DA energy in Fig. 4.5.

For the check of the reconstructed energy, J/Ψ production events and QED Compton events are also used. Figure 4.6 shows the comparison between the data and the MC after applied all the corrections. The systematic uncertainty for the energy scale is estimated as 1% for $E_e > 15$GeV and linealy increased for lower energy to be 2% at $E_e = 5$GeV.

Figure 4.7 shows the energy distribution for the KP events after all the correction. The energy in the MC is too good comparing with data. In the MC, smearing factor is applied event by event to worsen the resolution by 1 %.

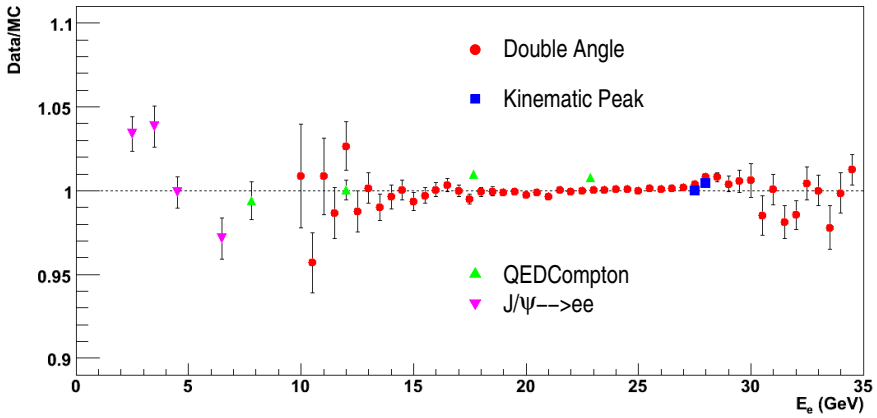

Figure 4.6: Energy calibration. The ratios of energy scale ($E_{rec.}/E_{ref.}$) in data to that in MC are shown.

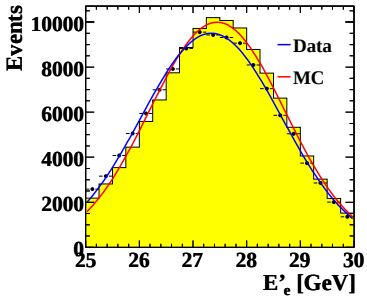

Figure 4.7: Energy distribution of KP events after the energy corrections. The points are data and the yellow histogram is the DIS MC.

4.3.3 Position reconstruction

The DIS cross section has a strong dependence on Q^2 by the factor of $\frac{1}{Q^4}$ and it requires good reconstruction of Q^2. As seen in Fig. 4.1 (b), θ_e is sensitive to the Q^2 reconstruction. In general, tracking performs a good reconstruction of θ_e. However, in this measurement, the scattered angle of the positrons is not so high and reasonable tracking is not always available for the positrons. Therefore, θ_e is reconstructed by the hit position of positrons on the ZEUS detector and the event vertex.

Variety of the position reconstruction

In the calorimeter, the hit position of the positron is reconstructed from the energy sharing between the cell with the maximum energy and its neighboring cells [46]. The y position is extracted using energy fraction between neighbouring cells. To reconstruct the x position, energy imbalance between the PMTs in the left and right sides of cells is also used. The depth of the electromagnetic shower depends on its energy and angle. The effect is taken into account in the both x and y reconstruction.

Comparing with the calorimeter, the HES can reconstruct the position with better resolution thanks to the finer granularity. The position is reconstructed by the logarithmic center of gravity of 9 pads where the center pad has the highest energy deposit. The closest HES cluster is matched to the positron reconstructed by the calorimeter.

Around the beam pipe, slight deviation of the measured position affects largely on the measurement, since it corresponds to the low Q^2 region. In this region, the SRTD also detects the scattered positrons and measures its position with good resolution. The position is reconstructed by the center of gravity of 3 strips around the highest energy deposit.

The tracking gives the position of the positron independently of its energy deposit in the calorimeter. However, the reasonable reconstruction of tracks requires for the positron to pass through tracking detectors with enough length. It cannot be done for the low angle positrons. The positions from the tracking except the low angle region are used only as the reference position in the detector alignment or the systematic checks.

Choice for the analysis

The analysis uses the position reconstructed from the HES and the SRTD for the θ_e reconstruction. The efficiency of the HES is high as shown in Fig. 4.8 and reasonably described by the MC.

The position from the CAL is not used in θ_e reconstruction since it is found that they deviates from the reference position given by the HES or tracking. The deviation depends on its position in a cell and gets larger in the outer cells.

If both the HES and the SRTD are available for position reconstruction, then the average is taken as the positron position. During the data taking period, there were some bad channels in both the SRTD and the HES and the situation of the channels differs time to time. The bad channels are simulated in the MC based on the luminosities of their period of failure.

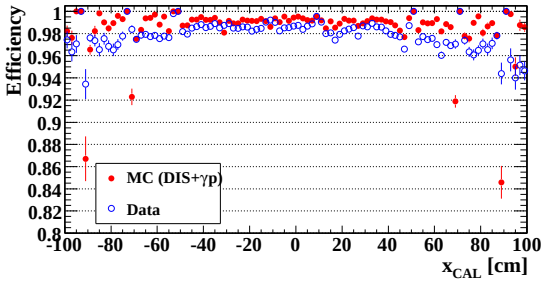

(a) HES efficiency as a function of x.

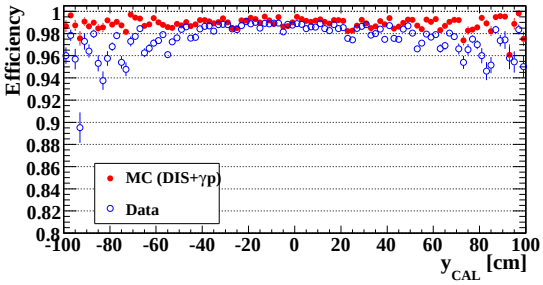

(b) HES efficiency as a function of y.

Figure 4.8: HES efficiency. The sample is described in Sec. C.1.

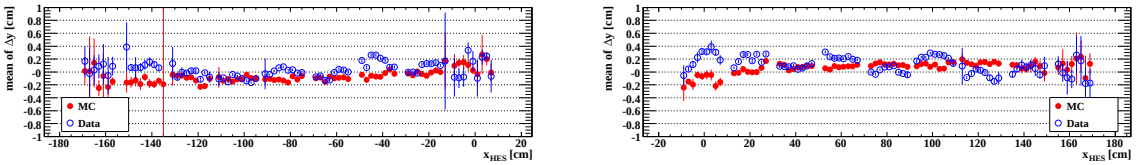

(a) Before the y alignment.

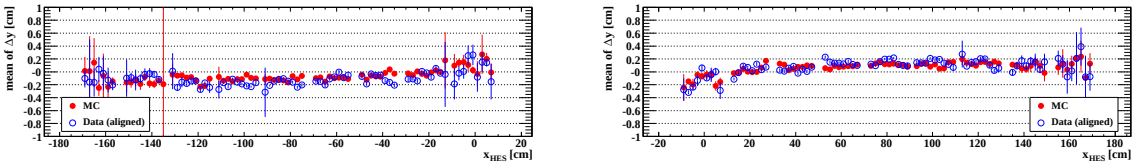

(b) After the y alignment.

Figure 4.9: HES module-by-module y alignment correction. The plots show $\Delta y = y_{\mathrm{HES}} - y_{\mathrm{Track}}$ vs x_{HES} for each negative-x and positive-x side of the RCAL.

HES position

At the installation, the HES modules were slid into each CAL module from the top. Therefore, the y position of each HES module may be shifted. Figure 4.9 (a) shows mean of $\Delta y = y_{\mathrm{HES}} - y_{\mathrm{Track}}$ distribution as a function of x_{HES}. The data clearly shows the structures with the length of ~ 20 cm. The module-by-module HES y alignment parameters are extracted by the comparison of the position from the HES and the tracking using the $e^- p$ scattering data taken in 2004 and 2005 [47]. The difference between the data and the MC is taken as the correction parameter and applied to the data used in this analysis. Figure 4.9 (b) shows the mean of Δy after the correction. The Δy in data gets flat. The correction parameters from $e^- p$ data work well for the 2006 $e^+ p$ data.

In Fig. 4.10, the distributions of $\Delta x = x_{\mathrm{HES}} - x_{\mathrm{Track}}$ and Δy after the y correction are shown. Their dependences on x or y are also shown in Fig. 4.11. The structure of every about 20cm in x is due to module edges, at which the HES has gaps. The Δx

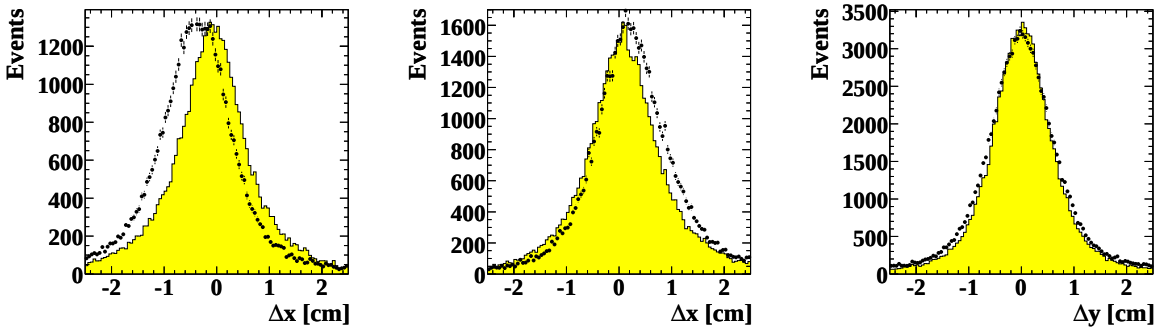

(a) Δx for $x < 0$. (b) Δx for $x > 0$. (c) Δy.

Figure 4.10: The distributions of $\Delta x = x_{\mathrm{HES}} - x_{\mathrm{Track}}$ and $\Delta y = y_{\mathrm{HES}} = y_{\mathrm{Track}}$. The points are data and the yellow histogram is the DIS MC.

quadrant	1	2	3	4
x shift [cm]	0.47	-0.25	-0.53	0.37
y shift [cm]	-0.24	0.26	0.09	-0.38

Table 4.1: SRTD alignment correction parameters

in data is shifted to negative and to positive for the positrons in the negative-x side and in the positive-x side of the RCAL. Small but similar shift is seen also in the MC. For Δy, though y dependence shows a slight slope, Δy is well distributed around 0.

From the width of the distributions in Fig. 4.10, the resolution of the position from HES can be considered as the same in the From Fig. 4.10 and Fig. 4.11, the discrepancy between the MC and the data is considered as 4 mm at maximum. Though the discrepancy can be contributed from the tracking, the insufficiency of the understanding of the position reconstruction is regarded as 4 mm. This number is used at the systematic checks described in Sec. 6.3.1.

SRTD position

Each SRTD quadrant is aligned with respect to the HES. The extraction of parameter is done using the sample with $E_e > 10$GeV from the period with the small number of SRTD bad channels. The distributions of $\Delta x(y) = x(y)_{\mathrm{HES}} - x(y)_{\mathrm{SRTD}}$ for each quadrant is looked for all the HER, LER and MER data. Figure 4.12 is an example of such distribution shown for quadrant 1 in the HER. For each quadrant, the mean position of the distribution is checked for all the HER, LER and MER data and the value agrees within 1 mm. The difference of mean position between the data and the MC is taken as the correction parameter. The final parameters are shown in Table 4.1 which are applied to the data.

The $\Delta x(y)$ distributions have different width as seen in Fig. 4.12 implying the different resolution of the SRTD in the data and the MC. Based on the differences, the SRTD position in the MC is smeared to have the same resolution as in the data.

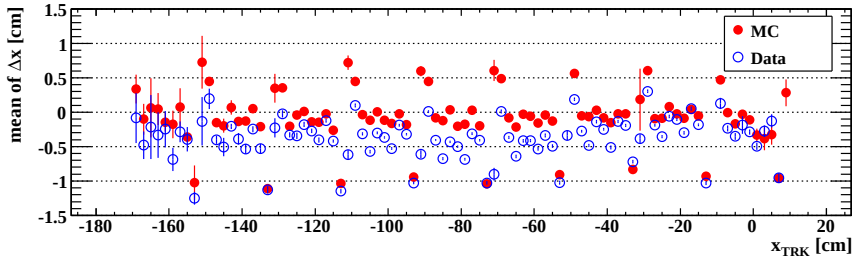

(a) $\Delta x = x_{\mathrm{HES}} - x_{\mathrm{Track}}$ vs x_{Track} for negative-x side of the RCAL.

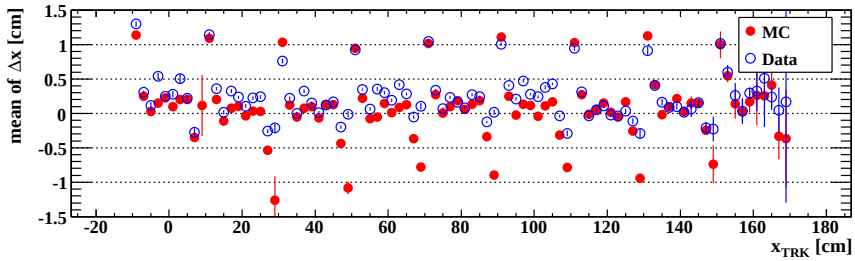

(b) $\Delta x = x_{\mathrm{HES}} - x_{\mathrm{Track}}$ vs x_{Track} for positive-x side of the RCAL.

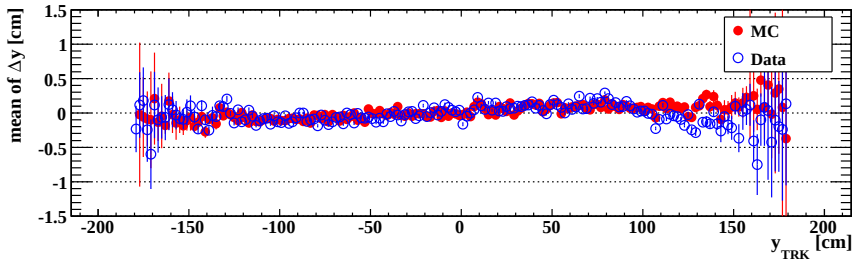

(c) $\Delta y = y_{\mathrm{HES}} - y_{\mathrm{Track}}$ vs y_{Track}.

Figure 4.11: Position dependence of the comparison of the HES and track positions.

4.3.4 Backward tracking

As mentioned in Sec. 4.3.1, the requirement of a track is a key issue to reject photons from the reconstructed positron samples. However, it is not suitable to require a track in the standard ZEUS reconstruction for positrons in the low Q^2 events ($Q^2 \lesssim 100\mathrm{GeV}^2$). The track reconstruction needs a certain number of hits in the tracking detectors, typically at least hits in 3 SLs of the CTD, so that the tracking efficiency for the low angle positrons is poor and it is also difficult to estimate the tracking performance in such region.

In order to make full use of the hit information in the tracking detector even without the track reconstruction, a new tool is developed for rejection of photons among the positron candidates.

Road utility

The concept of the utility is shown in Fig. 4.13. A *road* on which the particle has possibly passed can be created between the interaction point and the detected particle

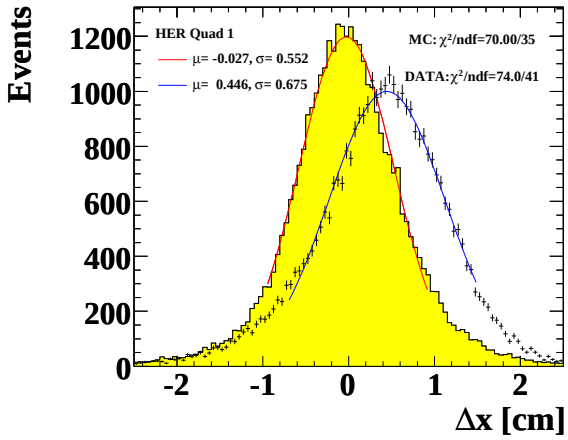

Figure 4.12: Δx distribution for the SRTD quadrant 1 in the HER. The points are data and the yellow histogram is the DIS MC.

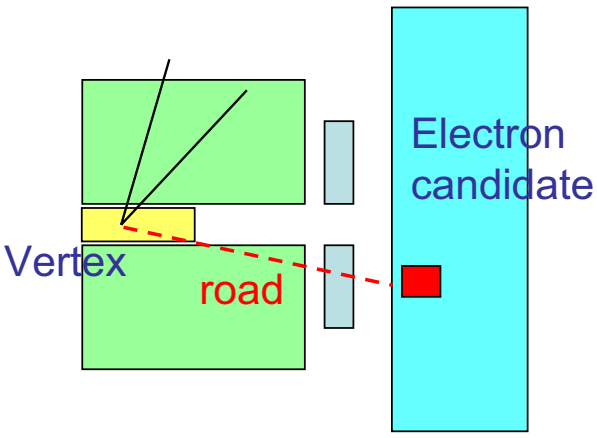

Figure 4.13: The road utility.

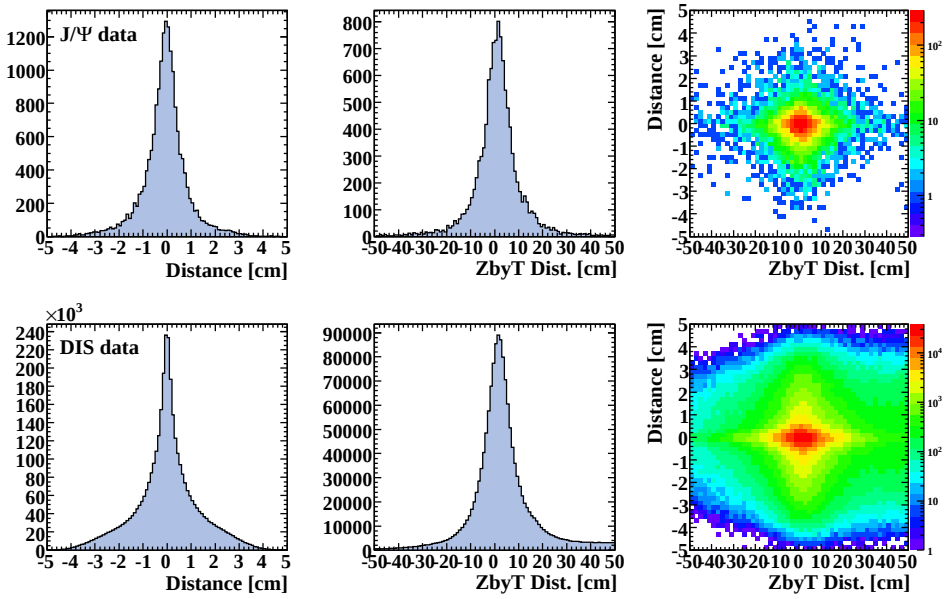

Figure 4.14: The distance distributions of the hits on the sense wires in the CTD SL 1. They are shown for J/Ψ data (upper row) and for DIS data (bottom row).

in the CAL. Hits around the road are collected and the number of them are evaluated to distinguish whether the particle has charge or not.

A road is created by the information of the reconstructed vertex and a positron candidate, which gives the energy and the position. The effect from the magnetic field is taken into account using the charge polarity, which is known from the beam polarity as the candidate should be a positron. The event vertex is expected to be reconstructed by the hadronic activity as described in Sec. 4.5.1.

Each sense wire of the CTD gives $r\phi$ hits. In addition, wires in the SL 1, 3 and 5 give the z coordination, by the z-by-timing ($ZbyT$). The distributions of the distance between a hit and the position of a road on the measurement plane of the sense wire is shown in Fig. 4.14 for $J/\Psi \longrightarrow e^+e^-$ and DIS data. They are shown for the hits on the sense wire in the SL 1. Due to the resolutions of the position of the positron candidate and the reconstructed vertex, $r\phi$ distance distribution has a width of $\sim O(1)$ cm. The $r\phi$ hits also have ambiguity whether the hit is on the left or right side of the sense wire. The $ZbyT$ distance distribution for the DIS data has a long tail in the positive side, indicating the contamination of coincidental hits from the hadronic activity in the forward region.

Hits are required to pass the distance cut. After detailed study of distance distributions, a loose selection is adopted.

$r\phi$	: -4 cm < *distance* <3 cm Regarding the left/right ambiguity, the distance is taken from the closer one.
$ZbyT$ (if available)	: -25 cm < *distance* < 25 cm.

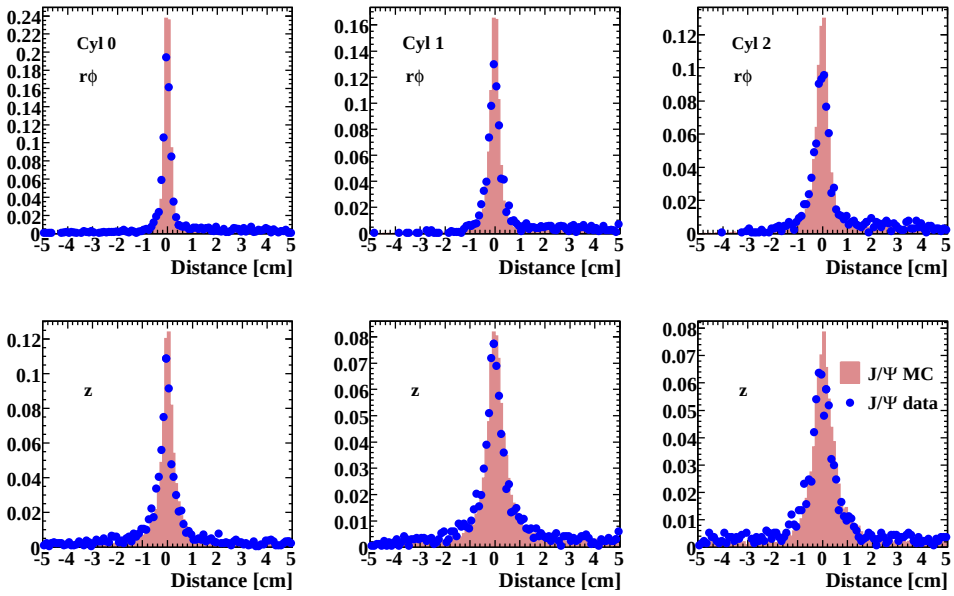

Figure 4.15: The MVD distance distribution comparing J/Ψ data to the MC. They are area normalized.

With this loose threshold, influence from the various dependences on, for example, E'_e, θ_e and the layer of the hit are negligible.

As described in Sec. 3.2.1, the MVD consists of silicon strip sensors. Since the typical MIP signal has ~ 90 ADC counts, a hits consisting of only 1-strip and with its signal less than 60 ADC counts is rejected as a noise hit. The distance distributions in the MVD are shown in Fig.4.15 for each cylinder and separately for hits on the $r\phi$ measurement plane and the z measurement plane . The distribution in the J/Ψ data is compared to the MC. The distribution gets wider for the z hits and hits on the outer layer. The distance cut for the MVD hits is

$$\begin{aligned} &\text{hit on } r\phi \text{ plane} \quad : \text{-1.5 cm} < \textit{distance} < \text{1.5 cm} \\ &\text{hit on } z \text{ plane} \quad : \text{-2.5 cm} < \textit{distance} < \text{2.5 cm}. \end{aligned}$$

The hits found around the road are counted and the result is evaluated by *Hit Fraction*,

$$\mathcal{F}_{\rm Hit} = \frac{N_{\textit{found hits}}}{N_{\textit{expected hits}}}, \tag{4.11}$$

where $N_{\textit{expected hits}}$ is the number of layers of the MVD or CTD geometrically overlapped by the road and $N_{\textit{found hits}}$ is those with hits. By using the form of fraction, it is less sensitive to the non-uniform structure in ϕ of the MVD and the dead sensor in the MVD. $\mathcal{F}_{\rm Hit}$ is calculated in each CTD and MVD separately, since they are quite different detectors. In the MVD, a single side of a ladder is counted as a layer. The situation of dead chips in the MVD is checked for each data taking period to analyze and they are excluded from the calculation of $\mathcal{F}_{\rm Hit}$.

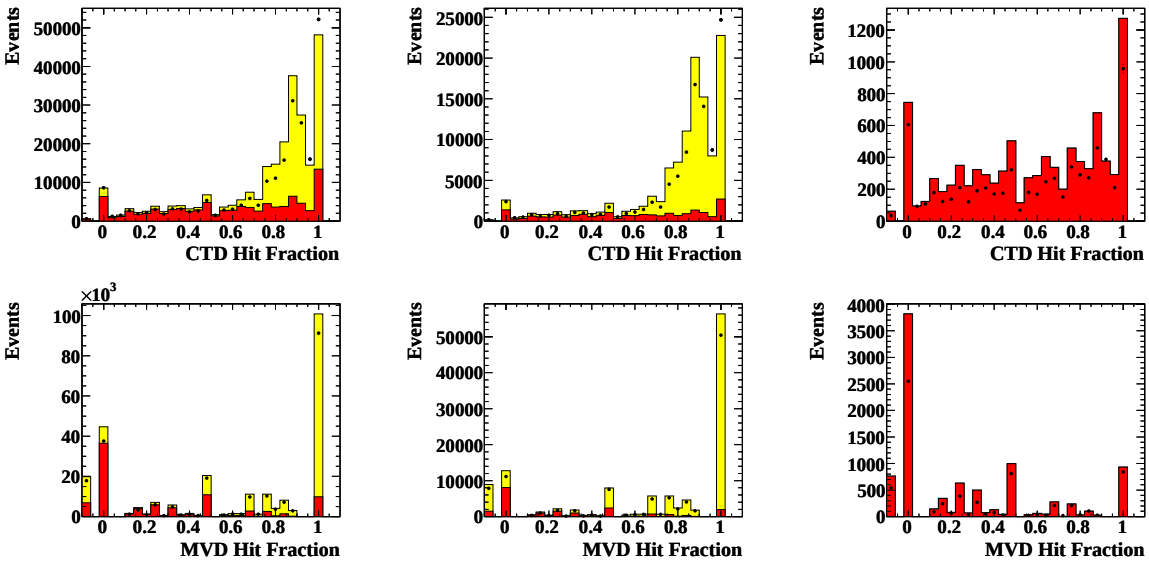

(a) DIS sample (b) high $E - p_z$ sample (c) 6m tagged sample

Figure 4.16: $\mathcal{F}_{\rm Hit}$ from the CTD and MVD. The points are data and the yellow and red histograms are the DIS+γp and the γp MCs, respectively.

The distributions of $\mathcal{F}_{\rm Hit}$ from the CTD and the MVD are shown in Fig. 4.16 for positron candidates with 4 GeV $< E_e <$ 12 GeV and 20 cm $< R_{\rm CTD} <$ 100 cm. Figures are for three samples, namely DIS sample (Chapter 5), high $E - p_z$ sample and 6m tagged sample (Sec. 5.4.1). In addition to the data, expectation from the DIS and the γp MCs are also shown[1] by colored histograms, where yellow one is for the sum of the DIS and the photoproduction MC and red one is for the photoproduction MC. The high $E - p_z$ sample has a higher threshold of 50 GeV on $\sum(E - p_z)$ so that the sample has less photoproduction events while 6m tagged sample is almost pure photoproduction sample. In the CTD $\mathcal{F}_{\rm Hit}$ distributions, DIS MC events have high value of $\mathcal{F}_{\rm Hit}$ as expected. For the photoproduction MC, not a small fraction of them are distributed also at high value of CTD $\mathcal{F}_{\rm Hit}$, since there can be hits due to the photon conversion or coincidental hits in the counted hits. The MVD $\mathcal{F}_{\rm Hit}$ distributions is discrete reflecting that the MVD has only 3 cylinders. Roads passing the edges of a sensor may have low value of MVD $\mathcal{F}_{\rm Hit}$. Nevertheless, photoproduction MC events are better separated from DIS MC events. This shows that the MVD has a good identification power for positrons. The difference between the MVD and the CTD is understandable since the MVD is closer to the interaction point and more photon conversions are seen in the CTD. In the all distributions, the data distributions are reasonably described by the MC.

[1]The normalization of the γp MC has 15% uncertainty as discussed in Sec. 5.4.

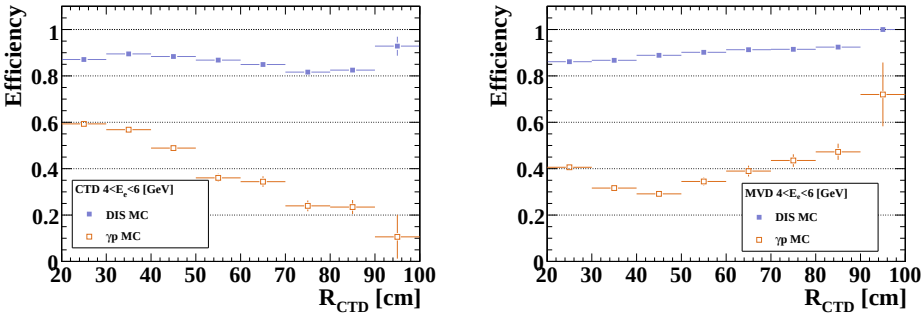

(a) CTD $\mathcal{F}_{\mathrm{Hit}} > 0.6$ (b) MVD $\mathcal{F}_{\mathrm{Hit}} > 0.45$

Figure 4.17: The efficiency with the CTD and the MVD hit requirement.

Performance of the road utility

With a requirement of a certain value of the $\mathcal{F}_{\mathrm{Hit}}$, the photoproduction rejection can be achieved. In Fig. 4.17, the efficiencies of the requirements of

$$\text{CTD } \mathcal{F}_{\mathrm{Hit}} > 0.60 \tag{4.12}$$

$$\text{MVD } \mathcal{F}_{\mathrm{Hit}} > 0.45 \tag{4.13}$$

is shown as a function of R_{CTD} for the both DIS and photoproduction MC events with low energy positron candidates (4 GeV $< E_e <$ 6 GeV). While $R_{\mathrm{CTD}} > 20$ cm ensures at least three expected CTD hits, there can be the events with no expected MVD hits. For these events, MVD $\mathcal{F}_{\mathrm{Hit}}$ requirement is not imposed. It is seen that the MVD has the highest discrimination power at $R_{\mathrm{CTD}} \sim 30$ cm and the CTD works better at the higher angle.

The efficiencies to fulfill the both MVD and CTD requirement is shown in Fig. 4.18 (a) and (b) for each DIS and photoproduction MC events with two ranges of E'_e. They are compared with the efficiency when a standard reconstructed track with $DCA < 10$ cm and $p_{\mathrm{Track}} > 1$ GeV are required, where DCA is the distance between the positron position on the CAL and the end point of a track and p_{Track} is the track momentum. While the $\mathcal{F}_{\mathrm{Hit}}$ requirement has similar photoproduction rejection power as the track requirement, it keeps high efficiency for the DIS events at the lower angle than the tracking works. At low E'_e, the DIS efficiency is worse than at medium E'_e. Among the 20 % inefficiency, many of the rejected events are very low Q^2 DIS events ($Q^2_{true} \lesssim$ 10 GeV^2) with misidentified positrons, such as photons from π^0. The efficiency plots restricted to the reconstructed positrons which match to the true scattered positrons only are also shown in Fig. 4.18 (c) using DIS MC. The plots show the $\mathcal{F}_{\mathrm{Hit}}$ requirement has high efficiency of more than 90 % for events with properly reconstructed positrons.

The efficiency of the $\mathcal{F}_{\mathrm{Hit}}$ requirement in the data is shown in Fig. 4.19 compared to the MC. For the MC, the DIS and photoproduction MC events are mixed according to their cross sections. The MC describes the data fairly well for all the R_{CTD} range. In the MC description, 80 % of photoproduction events are rejected by the $\mathcal{F}_{\mathrm{Hit}}$ requirement at $4 < E'_e < 6$ GeV as seen in the Fig. 4.18 (b).

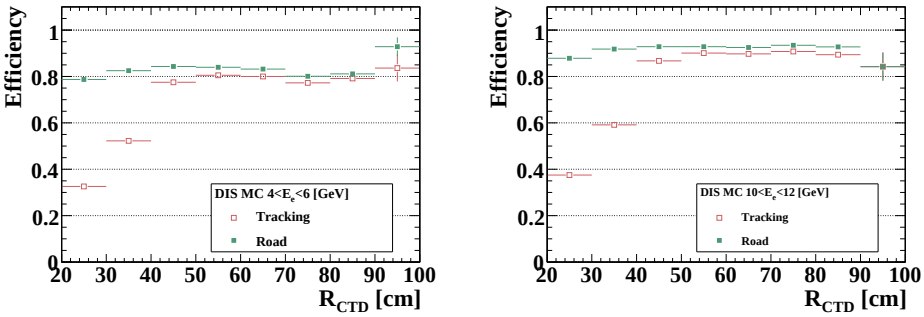

(a) DIS MC

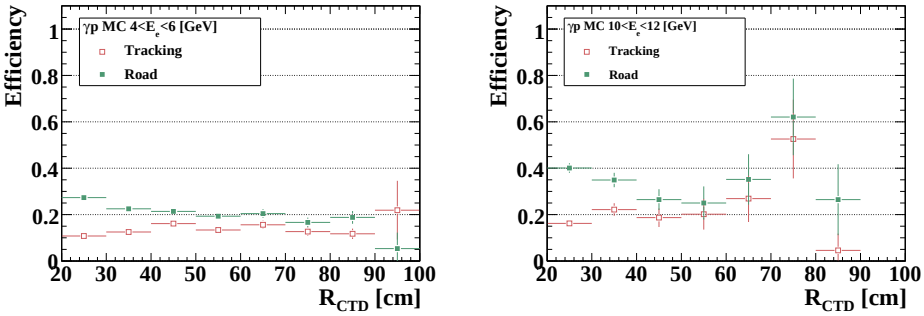

(b) γp MC

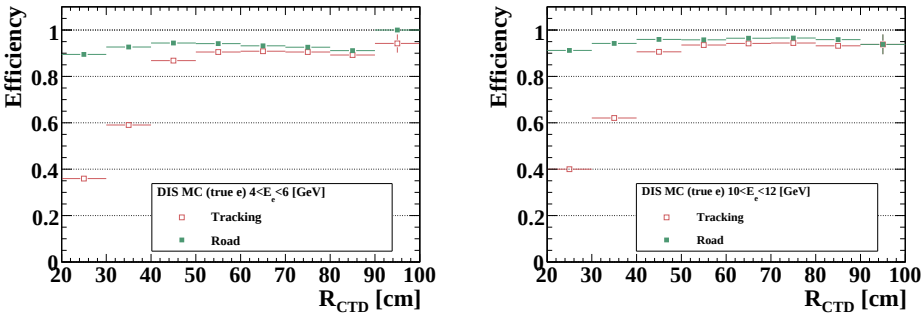

(c) DIS MC with properly reconstructed positrons

Figure 4.18: The efficiency with the hit requirement and the tracking for $4 < E'_e < 6$ GeV and $10 < E'_e < 12$ GeV.

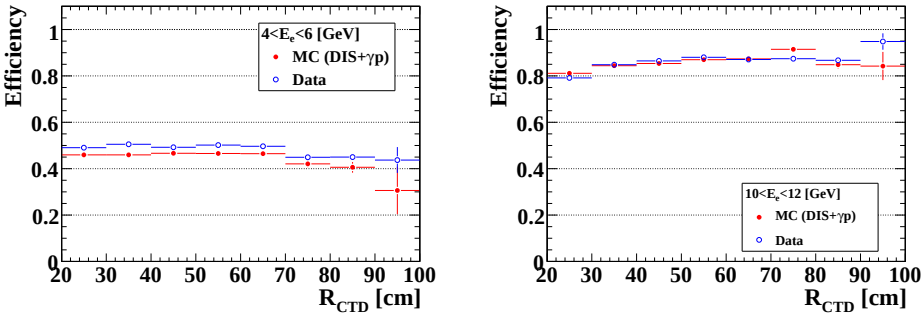

Figure 4.19: The efficiency with the hit requirement for $4 < E'_e < 6$ GeV and $10 < E'_e < 12$ GeV.

4.4 Hadron reconstruction

As long as the Electron method is used, hadron distributions do not directly affect the kinematic reconstruction. However, they still affect the measurement through the event selections.

The four momentum of the hadronic system, and hence δ_h and $p_{T,h}$, is reconstructed from the energy deposits in the calorimeter using the **CorAndCut** algorithm [48]. The algorithm creates *cone islands* by combining the clusters of calorimeter cells, which have energy deposit, in $\theta - \phi$ plane. After the back-splash rejection described below, the energy of each island is corrected by three kinds of corrections. The first one is the dead material correction, which is parameterized with the amount of the inactive materials and the measured energy, to correct the energy loss in the inactive materials. The second one is the correction for hadrons with low energy, where the ratio e/h of the calorimeter response is no longer 1 due to increase of ionization energy loss instead of showering. The last one is the correction for energy loss in the super-cracks, which are the name of the space between FCAL and BCAL or BCAL and RCAL. Then the hadronic four momentum, which gives δ_h and $p_{T,h}$, are reconstructed by the sum running on the islands.

The particles may be scattered off from the detector or HERA machine components creating secondary particles. They may cause energy deposits far away from its original position. Such energy deposits are called back-splash. The back-splash rejection are done by following manner. If an island has larger angle than a threshold γ_{max} which is defined as a function of $\gamma_{h,all}$ calculated from all the islands, and if it has energy less than 3 GeV, it is excluded from the reconstruction of hadronic four momentum and γ_h. The rejection also exclude calorimeter noises.

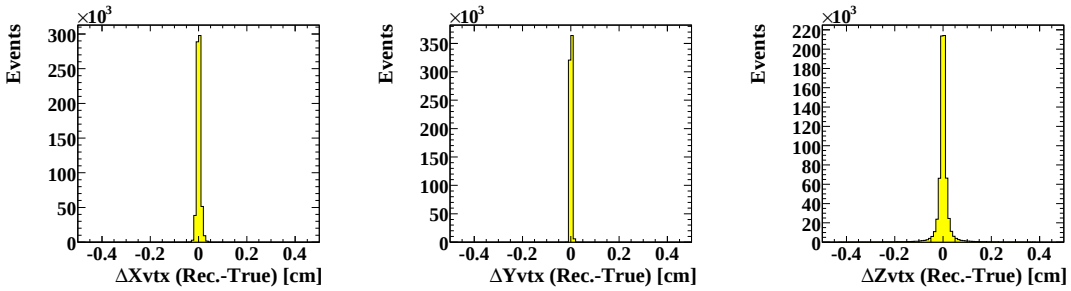

(a) x direction (b) y direction (c) z direction

Figure 4.20: The difference between the reconstructed vertex and true event vertex.

4.5 Vertex reconstruction

4.5.1 Reconstruction and efficiency

The accurate measurement of the event vertex is also essential to measure the angle of particle, hence to the kinematic reconstruction.

The hits from the charged particle in the tracking detectors are collected by the Pattern recognition. They are fitted using the Kalman filter with consideration of the material effect and the inhomogeneity of the magnetic field [49]. The primary vertex is reconstructed from them using the Deterministic Annealing Filter (DAF) [50] with the constraint of the beam spot. The difference between the reconstructed vertex and the true event vertex in each direction is shown in Fig. 4.20 for DIS MC selected by the DIS selections (Chapter 5) but without Z_{vtx} criteria. The plot shows good reconstruction of the vertex.

The efficiency of the vertex reconstruction is studied with a sample selected as in Sec. C.2. The efficiency is shown in Fig. 4.21, as a function of E'_e, $R_{\rm HES}$ and γ_h, where $R_{\rm HES}$ is the radius of positron position reconstructed only by the HES. In γ_h reconstruction, the position of $(0, 0, 0)$ is used as the vertex position, if no reconstructed vertex is available. The efficiency gets slightly worse at low $R_{\rm HES}$ and at high γ_h, i.e. where the angle gets close to the beam hole for the positrons and the hadronic system, respectively. However the efficiency is still more than 99% and the discrepancy between the data and the MC is within 1%.

4.5.2 Vertex distribution

Figure 4.22 shows the distributions of measured Z_{vtx}, the z position of the vertex, in the HER, LER and MER for the DIS sample (Chapter 5). The Z_{vtx} has wide distribution due to the length of the proton bunch. In addition to the main distribution, there are additional distributions at $Z_{vtx} \sim \pm 80$ cm, which are come from satellite bunches. The beams are captured in a RF bucket and the satellite bunch is formed by the protons which leak to the neighbouring bucket. As seen in Fig. 4.22, the fraction of the satellite distributions depends on the run. In the luminosity measurement, contribution from these satellite bunches is also included.

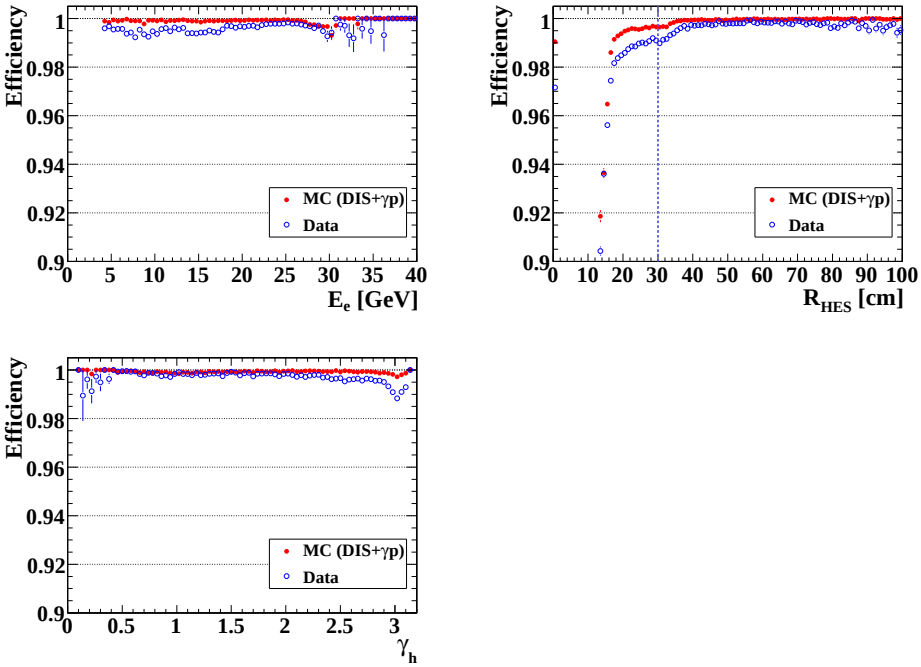

Figure 4.21: The vertex reconstruction efficiency.

Figure 4.23 shows the acceptance of the DIS selections (Chapter 5) except for the Z_{vtx} requirement. It is plotted as a function of true Z_{vtx}. The sample is all the generated DIS MC events described in Sec. 3.4, i.e. $Q^2_{True} > 1.5$ GeV^2. It shows that the acceptance of this measurement has the Z_{vtx} dependence. Since the radius cut is applied on the position of the positron at $z = -100$ cm as described in Sec. 5.3.1, low angle events, which have large cross section, are more accepted in the forward region. In the final selection, the reconstructed Z_{vtx} is also required to be in some range. To understand the acceptance of the measurement, the MC needs to reproduce the Z_{vtx} distribution in data, which depends on the beam condition, hence has a run dependence as written above.

The distribution of the Z_{vtx} for each HER, LER and MER sample is measured with the following procedure to have less bias from Z_{vtx} as possible. The DIS events are selected in the three separated region with different detector acceptance. The separation is done by the angle of the scattered positron so that efficiency in each region has less dependence on the Z_{vtx} as possible. A well reconstructed track from the hadronic system is also required to ensure that the vertex reconstructed by the hadrons. With these selections, the efficiency in each region gets linear and very little dependence on Z_{vtx} in a certain Z_{vtx} range. By combining the Z_{vtx} distribution from each region with consideration of efficiency, the Z_{vtx} distribution is measured with minimum bias.

MC events are generated based on the measured Z_{vtx}.

It is also important for MC to reproduce the position of X_{vtx} and Y_{vtx} in data since both directly affect the θ_e reconstruction. Their distributions in the MC are

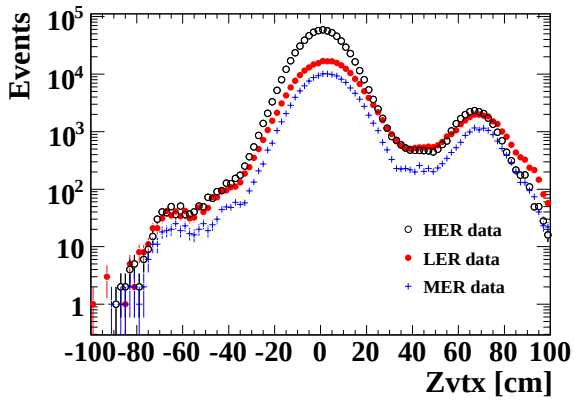

Figure 4.22: The Z_{vtx} distribution in HER, LER and MER data selected by the DIS selections.

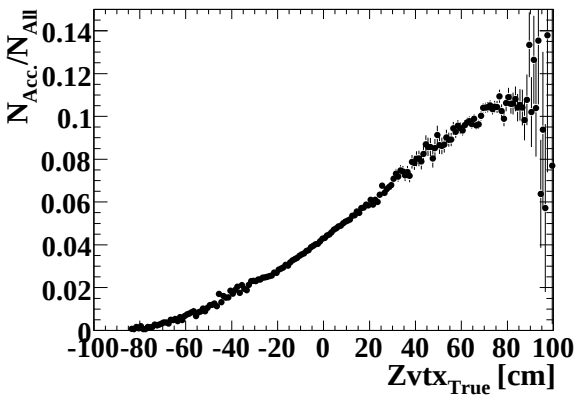

Figure 4.23: The acceptance of the DIS selection except for Z_{vtx} requirement. It is shown as a function of MC true Z_{vtx}.

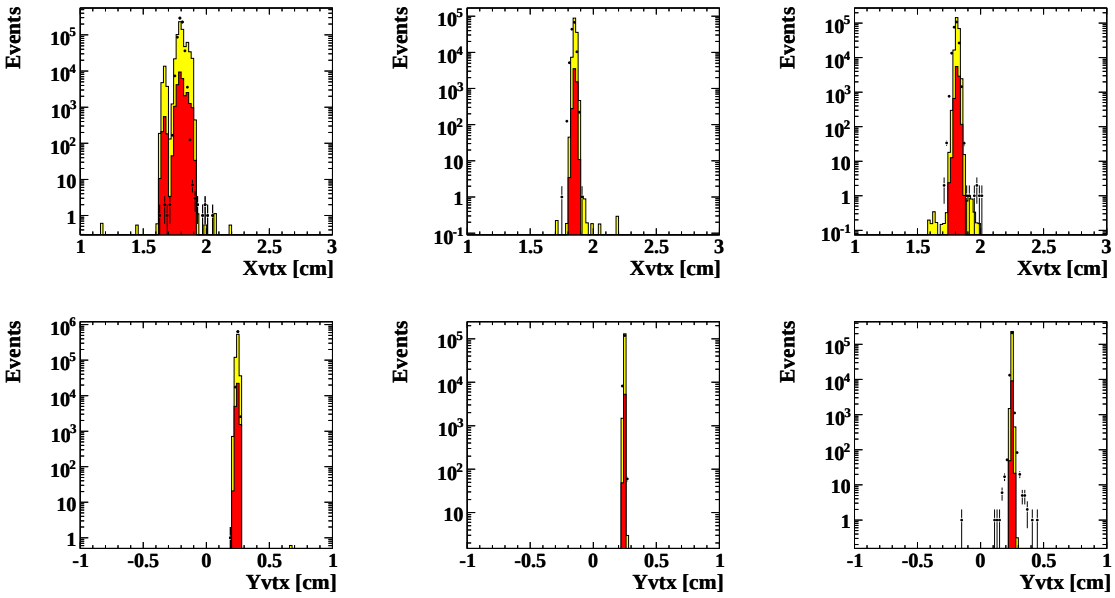

(a) HER (b) MER (c) LER

Figure 4.24: The X_{vtx} and Y_{vtx} distributions. The points are data and the yellow and red histograms are the DIS+γp and the γp MCs, respectively.

determined from the data. Figure 4.24 shows the distributions of X_{vtx} and Y_{vtx} after the DIS selections. The peak positions in MC agree well with the data for all the HER, MER and LER samples. In the HER X_{vtx} distribution, secondary peaks are seen only in the MC. The peaks are associated to the data sample not used in this measurement. The effect of the peak to the cross section measurements is investigated and found to be negligible.

Chapter 5

Event selection

5.1 Analyzed data sets

As the F_L measurement is done by the comparison of the cross section at the different beam energies, the e^+p data sets taken in the HER, LER and MER are analyzed. Data taking was done during a part of the HER period and the whole LER and MER periods.

Due to the higher instantaneous luminosity in the HER than the LER and the MER, the data taking was done as following. As described in the next section, two kinds of trigger configuration were prepared for data taking, namely medium-Q^2 and low-Q^2 trigger logics. The latter also collects DIS events at lower Q^2 compared with the former. The data taking with the low-Q^2 trigger logic was done for the whole LER and MER period and a short period ($\sim$ 3 weeks) in the HER. To collect luminosity for higher Q^2 in the HER, the data taking with the medium-Q^2 trigger logic was done for longer period. In this analysis, the HER data taken with medium-Q^2 trigger logic and the whole the LER and MER data are used.

In addition to the data taking with the proper trigger setup, the data is required to be taken with good condition of the important detectors for the measurement, namely the CAL, the CTD, the luminosity monitor, the HES and the MVD.

Table 5.1 summarizes three data sets used in this analysis. All the data is e^+p scattering data.

	HER	LER	MER
Center of mass energy	318 GeV	225 GeV	252 GeV
Proton beam energy	920 GeV	460 GeV	575 GeV
Year of the data taking	Sep.-Dec. 2006	Mar.-May 2007	June 2007
Trigger configuration	medium-Q^2	low-Q^2	low-Q^2
Integrated luminosity	31.7 pb^{-1}	13.8 pb^{-1}	7.1 pb^{-1}

Table 5.1: The analyzed data sets.

5.2 Online event selection

The requirements for the online event selections, i.e. the trigger, are to take the interesting physics with high efficiency and to suppress the event rate to the acceptable level by rejecting backgrounds.

A specific signature of the DIS events is the existence of the scattered positron as already mentioned in Sec. 4.1. In this analysis, the interesting events are the low Q^2 and high y DIS events. The scattered positrons have low scattering angle and low energy. The accurate tagging of such a positron is difficult so that the online selection tries to be less sensitive to online positron finding as possible.

In another way, the existence of positron in the detector can be implicitly required by the high value of $\sum(E - p_z)$. The sum runs over all the energy deposit in the main detector. Its value would be twice of the positron beam energy for ep scattering if no particle escape to the negative z direction through the beam pipe. Though it still rejects some of DIS events with the photon radiation, the requirement of high value of $\sum(E - p_z)$ can effectively reject the non-DIS events which do not have the scattered positrons in the main detector.

The main non-DIS backgrounds are beam gas events, off-momentum positrons, photoproduction events and cosmic rays. The off-momentum positrons are the beam positrons which have interacted with residual gas in the beam pipe far from the interaction point and deviate from their orbit. Some of them escape from collimators in the beam line and hit the certain position of the CAL with lower momentum than the beam energy. The photoproduction events have similar final state as the DIS events except for the absence of the scattered positron.

As already mentioned in the previous section, two kinds of the trigger configuration, medium-Q^2 and low-Q^2 trigger logics, are prepared to cope with the high instantaneous luminosity in the HER. The medium-Q^2 trigger logic has a tighter selection focusing on events with the scattered positron outside the first inner ring of the RCAL, which corresponds to the events with $Q^2 \gtrsim 20\text{GeV}^2$, while the low-$Q^2$ trigger logic tries to tag the positrons on the first inner ring also. The overview of the both trigger logics are;

- requirement of EMC energy with isolation and/or track existence at the FLT,
- $\sum(E - p_z)$ requirement at the SLT (i.e. positron requirement is not applied),
- the medium-Q^2 trigger logic consists of OR of the $E - p_z$ filter and the positron finding filter, while the low-Q^2 trigger logic requires $\sum(E - p_z)$ only.

The cross section for each logic is estimated during HER and it was $\sim 0.4\mu$b for the medium-Q^2 trigger logic and $\sim 1\mu$b for the low-Q^2 trigger logic.

5.2.1 Medium-Q^2 trigger logic

FLT

The FLT requirement is to fire one of the 11 slots which are described in Appendix D. In the HER, the logic is designed to inclusively take events with low energy positrons

at the outside the RCAL 1st inner ring. In addition to the requirement of REMC energy excluding the 1st inner ring, the logics require either *Risoe*, the isolated EMC energy deposit with the EMC energy above 2 GeV, or at least one *good track*, which usually exists from hadronic activity in high y events.

SLT

Following four requirements are imposed at the SLT;

- $\sum(E - p_z) > 30$ GeV
- $E_{\mathrm{REMC}} > 2.5$ GeV OR $E_{\mathrm{BEMC}} > 2.5$ GeV OR $E_{\mathrm{FEMC}} > 10$ GeV OR $E_{\mathrm{FHAC}} > 10$ GeV
- Off-momentum positron rejection
  The events with the positrons which are in a certain small region and with low $\sum(E - p_z)$ or no other energy deposit are rejected as off-momentum positron events.
- Vetoes
  The timing vetoes and the spark veto are applied at the SLT. The timing vetoes reject cosmic or beam gas events based on the CAL timing and its differences between up/down or FCAL/RCAL. The spark veto excludes fake positrons due to electric discharge of a PMT which can be recognized by a break of energy balance between two PMTs for a CAL cell.

TLT

The TLT logic is the OR of two filters, one (SPP16) is positron finding filter and the other (SPP15) is $E - p_z$ filter which is free from the performance of the online positron finders.

SPP16

- $\sum(E - p_z) > 30$ GeV AND
- positron with $E_e > 4$ GeV, $|x| > 15$ cm and $|y| > 15$ cm (box cut)

SPP15

- $30\mathrm{GeV} < \sum(E - p_z) < 100$ GeV AND
- $20\mathrm{GeV} < \sum^{\mathrm{ex.1ir}}(E - p_z)$, where the sum does not include the energy deposit in the RCAL 1st inner ring.
  The DIS events which are exclusively rejected by this should have positrons in the RCAL 1st inner ring.

5.2.2 Low-Q^2 trigger logic

FLT

The FLT requirement is again to fire one of the 11 slots as in the HER logic, but some of them have looser criteria to take events with positrons on the RCAL 1st inner ring also. The main slot to take such events requires both *Risoe* and *good track*.

SLT

The SLT logic is the same as in the HER.

TLT

The requirement is only $\sum(E - p_z)$ to take events inclusively as possible.

- $30\text{GeV} < \sum(E - p_z) < 100$ GeV

5.3 Offline event selection

At the offline analysis, further precise event selections are applied for the events which pass the online selections. The offline selections ensure the good reconstruction of events and increase the purity of the sample.

The positron requirement is a key issue of event selection. In the previous $\tilde{\sigma}$ measurement [51], the lowest E'_e was 8 GeV with tight P_{Sira} requirement ($P_{\text{Sira}} > 0.96$ at $E'_e = 8$ GeV [52]). However, this measurement aims to take positrons with lower E'_e with a reasonable efficiency. The development of the road utility (Sec. 4.3.4) has enabled a better rejection power for the photoproduction backgrounds. It allows to use positrons with lower P_{Sira} so that the positron efficiency was increased. Further details are described in the following sections.

5.3.1 Positron requirement

The most important selection for DIS events is requirement of the scattered positron. For the precise identification of the positron, the following conditions are applied on the positron candidate with the highest P_{Sira}, the *probability* from the SINISTRA. Events with the candidate fulfilling the following conditions are selected.

- Probability cut
  A positron candidate should have enough high P_{Sira} as

$$P_{\text{Sira}} > 0.95 - 1.5 \cdot \exp\left(-\frac{E_e}{2.5}\right), \text{ with the lowest boundary } 0.8.$$

  In order to keep a good efficiency for low energy positrons, the threshold has an energy dependence. The P_{Sira} distributions before the P_{Sira} and E'_e are shown for DIS MC and γp MC with the threshold lines in Fig. 5.1 (a) and (b).

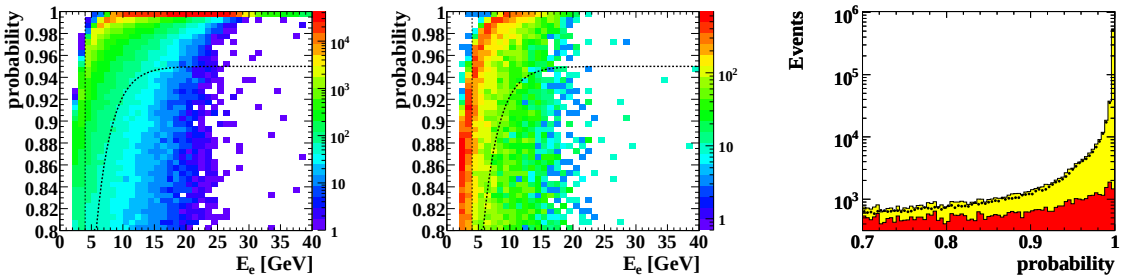

(a) DIS MC (b) γp MC (c) P_{Sira}

Figure 5.1: Distributions of P_{Sira}. The left two plots show the correlation with E'_e. The dotted lines are threshold lines in the event selections. The sample is HER sample.

- Energy cut
  The lowest energy of the positron is required to be found with good identification power of the finder,

$$E_e > 4 \text{ GeV}$$

- Requirement of hit(s) in the tracking detectors
  The existence of hits in the tracking detectors should confirm the candidate is a charged particle. Using the road utility described in Sec. 4.3.4, the *Hit Fraction*, $\mathcal{F}_{\mathrm{Hit}}$, is required to be

$$\begin{array}{ll} \text{CTD } \mathcal{F}_{\mathrm{Hit}} \geq 0.6 & \text{AND} \\ \text{MVD } \mathcal{F}_{\mathrm{Hit}} \geq 0.45 & \text{if the candidate traverses the MVD.} \end{array}$$

  Since the CTD tends to have larger value of $\mathcal{F}_{\mathrm{Hit}}$ compared to the MVD, the different thresholds are applied.

- Requirement of a HES hit
  The positron candidate should be associated with a HES cluster. It is required to use the position reconstructed by the HES in the analysis. The requirement for a candidate is to have

  > a HES hit with a signal above 5 MIP and within 10 cm from the candidate position reconstructed by the CAL.

- Radius cut

$$R_{\mathrm{CTD}} > 20 \text{ cm},$$

  where R_{CTD} is the radius of the positron position on the CTD exit window ($z = -100$ cm). The cut ensures the positron to traverse at least three layers of the CTD, which is preferable to the hit requirement using the road utility. In addition, $R_{\mathrm{CTD}} = 20$ cm corresponds to $R_{\mathrm{CAL}} \sim 30$ cm so that the cut generally override the box cut at the one of the TLT filter (SPP16).

- Geometry cut
  To ensure the good reconstruction of the positrons, the following geometry cuts on the positron position are applied.

  - module edge cut
    The energy measurement of a positron hitting a module is degraded due to the existence of the wave length shifter. Moreover, the HES does not cover the module edge so that the reconstructed position near the module edge has larger uncertainty. The positrons are required not to be at the module edge as

    $$\text{the distance to the module edge} \begin{cases} > 1.5 \text{ cm in the BCAL} \\ > 2.0 \text{ cm in the RCAL.} \end{cases}$$

    These distances roughly corresponds to the Moliere radius (2 cm) of the calorimeter.

  - super crack cut
    The space between the RCAL and the BCAL is called the super crack. In the $r\phi$ view, the BCAL placed in front of the outer part or the RCAL. If the scattered positron comes to this region, the energy deposit may be shared with both the BCAL and the RCAL. The positron reconstruction in this case is complicated and easily causes misreconstruction of events. Therefore, the super crack region is cut out by requiring

    $$\begin{aligned} &\text{IfapositronisinBCAL}: \quad z \geq -93.5\text{cm} \\ &\text{IfapositronisinRCAL}: \quad r < 135\text{cm}. \end{aligned}$$

  - chimney cut
    The RCAL has a region where EMC cells does not exist. It is to make a space for the cryogenic pipe to the solenoid coil. Without the EMC, positrons cannot be measured well.

    $$\text{Reject positrons in } (y > 90 \text{ cm AND } -14\text{cm} < x < 12\text{cm}) \text{ on the RCAL}$$

  - calorimeter gap cut
    The left and right halves of the RCAL are separated to make it possible to open the ZEUS detector, They can be slid in x direction. The upper part of the middle module is attached to the negative side of the RCAL and the lower part is attached to the positive side. There is a gap between the left and the right halves. The positrons around the gap are rejected.

    $$\text{Reject positrons in} \left\{ \begin{array}{ll} y > 0 & 6.5\text{cm} < x < 12\text{cm} \\ y < 0 & -14\text{cm} < x < -8.5\text{cm} \end{array} \right\} \text{on the RCAL}$$

5.3.2 Vertex requirement

An event should be measured well within the acceptance of the ZEUS detector. The proper angle measurement can be done only with the reconstructed vertex. As seen in Sec. 4.5.1, the efficiency to have the reconstructed vertex is high. The requirement for the event vertex is

Reconstructed event vertex with $|Z_{vtx}| < 30$ cm,

which is within the length of the BMVD. The requirement also rejects background events caused by beam-related or cosmic events, in which particles come not from the central part but from the out of the detector.

5.3.3 Background rejection

Further selections are applied to reject background events and to increase the purity of the sample. As already mentioned in Sec. 5.2, $\sum(E - p_z)$ of DIS events without the initial state radiation should be around 55 GeV, twice of the positron beam energy. If the radiation occurs, the radiated photon bring out some of $E - p_z$ so that the value of $\sum(E - p_z)$ gets lower. From the point of uncertainty on radiative correction, it is better not to apply a tight cut on the value of $\sum(E - p_z)$. On the other hand, the photoproduction events have also low value of $\sum(E - p_z)$ since the positron escape through the beam pipe. For their rejection, imposing a lower boundary is useful. At the upper side of the peak of 55 GeV, the beam gas backgrounds may cause the high value of $\sum(E - p_z)$. Therefore, the value is required to be in the range of

$$42 < \delta < 65 \text{ GeV},$$

where $\delta \equiv E'_e(1 - \cos\theta_e) + \delta_h$. In the rest, δ is also referred as $E - p_z$.

In the DIS, the transverse momentum of the hadron system ($p_{T,h}$) and the scattered positron ($p_{T,e}$) should balance so that the requirement of

$$p_{T,h}/p_{T,e} > 0.3$$

is applied. In addition to the suppression of non-DIS events, it eliminates poorly reconstructed DIS events.

Another background source is large angle QED Compton events, which have a positron and a photon in the main detector. By considering all the activity excluding the scattered positron as a hadronic system, the events can contaminate to the high Q^2 events. Elastic QED Compton events are rejected using the event topology.

> Elastic QED Compton rejection;
> An event has multiple positron candidates with two of them fulfilling
> - balancing in p_T
> - back-to-back in $r\phi$ plane
> - the rest energy in the event < 3 GeV
>
> is rejected.

5.3.4 Kinematic cuts

Furthermore, kinematic cuts are applied on the selected sample. Since the important region for this measurement is high y, the event selections are optimized to the high y events. The low y region is excluded from the analysis by the requirement of

$$y_{JB} > 0.05.$$

The positron energy requirement of $E_e > 4$ GeV corresponds to $y \lesssim 0.85$ for $Q^2 \lesssim 100$ GeV^2. The events with very high reconstructed y_{el} should have positrons in the forward direction, where there are huge fake positrons originated from the hadronic system in the photoproduction. They are excluded by requiring

$$y_{el} < 0.95.$$

5.3.5 Summary of the offline event selection

In summary, the applied selections are as following.

- Positron requirement. A positron candidate with the highest P_{Sira} is considered.
  - $P_{\text{Sira}} > 0.95 - 1.5 \cdot \exp\left(-\frac{E_e}{2.5}\right)$
  - $E_e > 4$ GeV
  - CTD $\mathcal{F}_{\text{Hit}} \geq 0.6$
  - MVD $\mathcal{F}_{\text{Hit}} \geq 0.45$ if the candidate traverses the MVD.
  - A HES hit with a signal above 5 MIP and within 10 cm from the candidate position reconstructed by the CAL.
  - $R_{\text{CTD}} > 20$ cm
  - Geometry cut
- Requirement of reconstructed event vertex with $|Z_{vtx}| < 30$ cm
- $42 < \sum(E - p_z) < 65$ GeV
- $p_{T,h}/p_{T,e} > 0.3$
- Elastic QED Compton rejection
- $y_{JB} > 0.05$
- $y_{el} < 0.95$.

The number of events after all the selections is 654780, 226331 and 127124 events for the HER, LER and MER data respectively.

5.4 Photoproduction backgrounds

In the selected events, a small but non-negligible number of photoproduction background events are still contaminated. Their amount needs to be estimated by the photoproduction MC. However, the cross sections of photoproduction used in the MC is based on a model and should not be blindly trusted. They should be checked by a comparison with the data. Two samples are used for this comparison, namely *6m tagged sample* and *photoproduction enriched sample*.

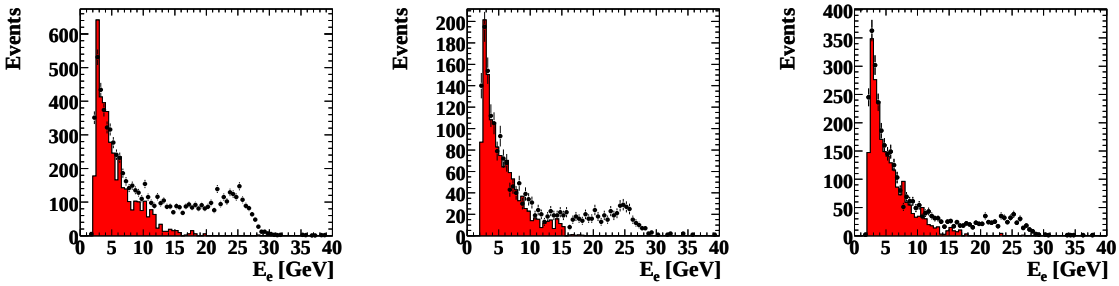

(a) HER (b) MER (c) LER

Figure 5.2: E'_e distribution for 6m tagged sample. The points are data and the red histogram is the γp MC.

5.4.1 6m tagged sample

The direct detection of photoproduction events can be done by the 6m tagger, which detects the positrons escaping from the main detector. The distribution of photoproduction events is checked using the 6m-tagged sample.

Among the DIS sample, events which has a positron in the 6m tagger with the energy of $3 < E < 10.5$ GeV are selected[1]. The positron energy, E'_e, reconstructed in the main detector is shown in Fig. 5.2, where dots are data and red histogram is the photoproduction MC. In addition to the scattered positrons from photoproduction events, the 6m tagger also detects positrons from the Bethe Heitler process. The process has a high cross section so that the 6m tagged data also contains genuine DIS events with the accidental overlap with the Bethe Heitler process. These overlapped events need to be statistically subtracted. In order to estimated the fraction of accidentally overlapping of the Bethe Heitler events, the ratio of the tagged data to the all selected DIS data is extracted as plotted in Fig. 5.3. At $E'_e \gtrsim 15$ GeV, where the fake positrons are expected not to be contaminated, the ratio is almost constant. The values indicated by the dotted lines in the plots are used as the overlapping fractions. The DIS data distributions after multiplying the factor is subtracted from the 6m tagged distributions as the DIS contribution.

The distribution of tagged events after the subtraction of overlapped DIS events is shown in Fig. 5.4 for each HER, LER and MER sample. Though the agreement is not perfect, E'_e and $\sum(E - p_z)$ distributions are reasonably described by the MC both in the shape and the absolute value.

5.4.2 Photoproduction enriched sample

The other sample to see distributions of photoproduction events is so-called photoproduction enriched sample. The sample is selected similar to the DIS selections but with different thresholds on E'_e, $\sum(E - p_z)$ and P_{Sira} to take the photoproduction events dominantly;

[1]The detailed selection for the 6m tagger is described in Sec. C.3

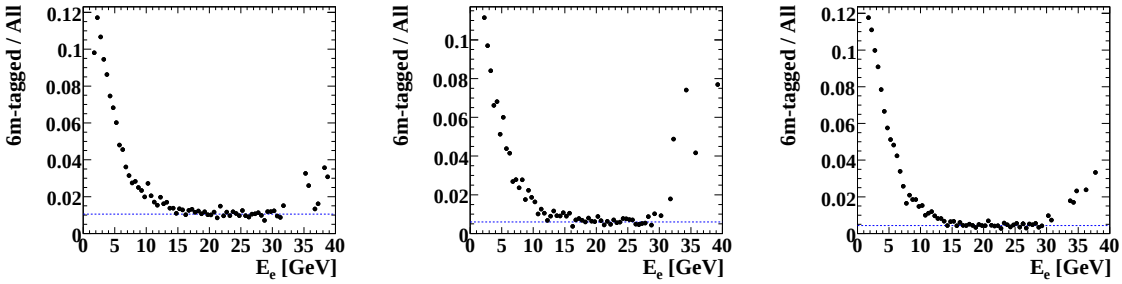

(a) HER (b) MER (c) LER

Figure 5.3: Fraction of overlapped DIS events.

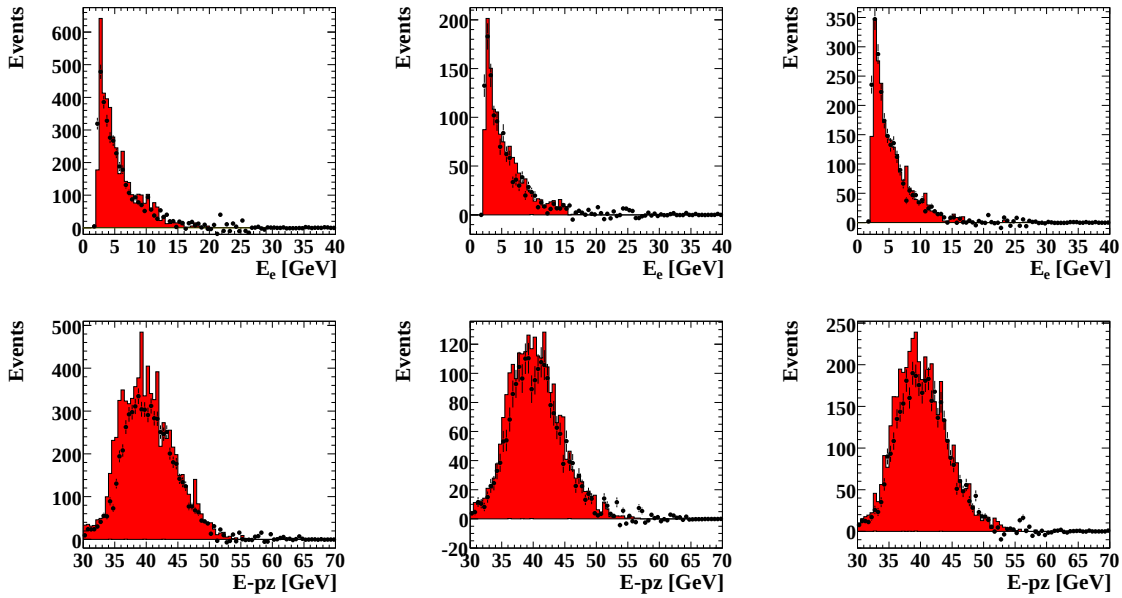

(a) HER (b) MER (c) LER

Figure 5.4: Distributions of 6m tagged sample after the subtraction of overlapped events. The points are data and the red histogram is the γp MC.

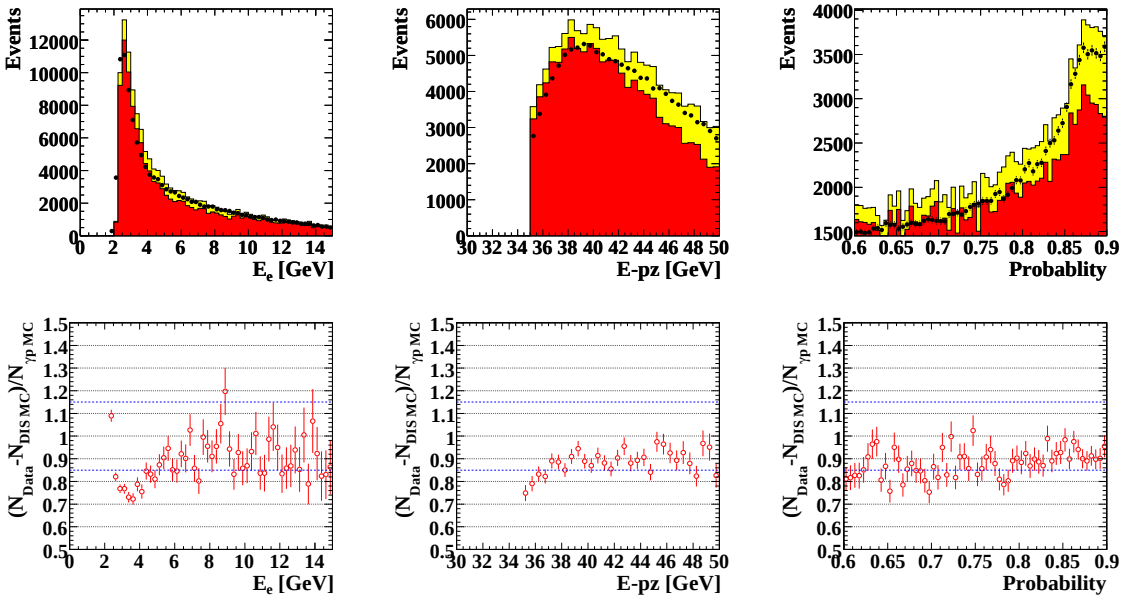

Figure 5.5: Distributions of photoproduction enriched sample for HER. The points are data and the yellow and the red histograms are the DIS+γp and the γp MCs, respectively.

- $2 < E'_e < 15$ GeV
- $35 < \sum(E - p_z) < 50$ GeV
- $0.6 < P_{\mathrm{Sira}} < 0.9$.

The distributions of the sample are shown in the upper part of Fig. 5.5, Fig. 5.6 and Fig 5.7 for HER, LER and MER respectively. The red and yellow histograms are the photoproduction MC and the sum of the photoproduction and DIS MC, respectively. They indicate that most of the events in this sample are photoproduction events. The distributions of E'_e, $\sum(E - p_z)$ and P_{Sira} are reasonably described by the MC for all HER, LER and MER. In the lower part of the figures, plotted are the ratio of

$$\frac{N_{\mathrm{data}} - N_{\mathrm{DIS\ MC}}}{N_{\gamma p\ \mathrm{MC}}}, \tag{5.1}$$

which corresponds to the expected normalization of the γp MC. The ratios are generally around 1 and almost flat. In the plots, the blue dotted lines are ± 15 % lines from 1 and the ratios are well distributed within the lines, especially at $E'_e > 4$ GeV.

5.4.3 Conclusion

From the both samples described above, it is seen that MC reasonably describes the photoproduction data. The photoproduction MC is used as it is, i.e. the normalization scale is set to 1. The uncertainty of normalization is assigned as $\pm 15\%$. This value is used for testing systematic uncertainty in Sec. 6.3.1.

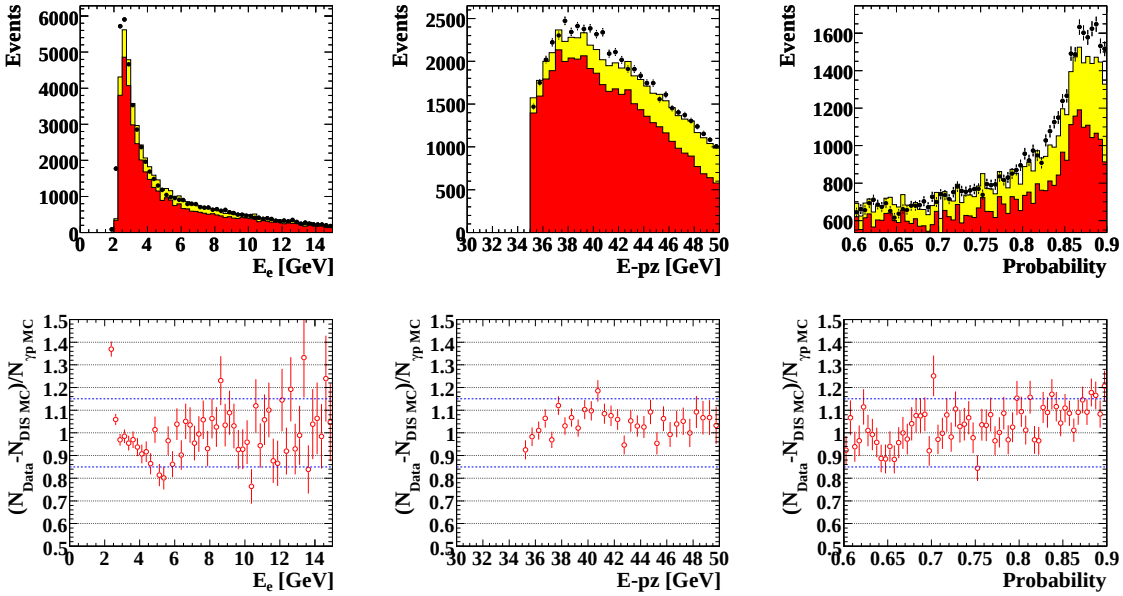

Figure 5.6: Distributions of photoproduction enriched sample for LER. The points are data and the yellow and the red histograms are the DIS+γp and the γp MCs, respectively.

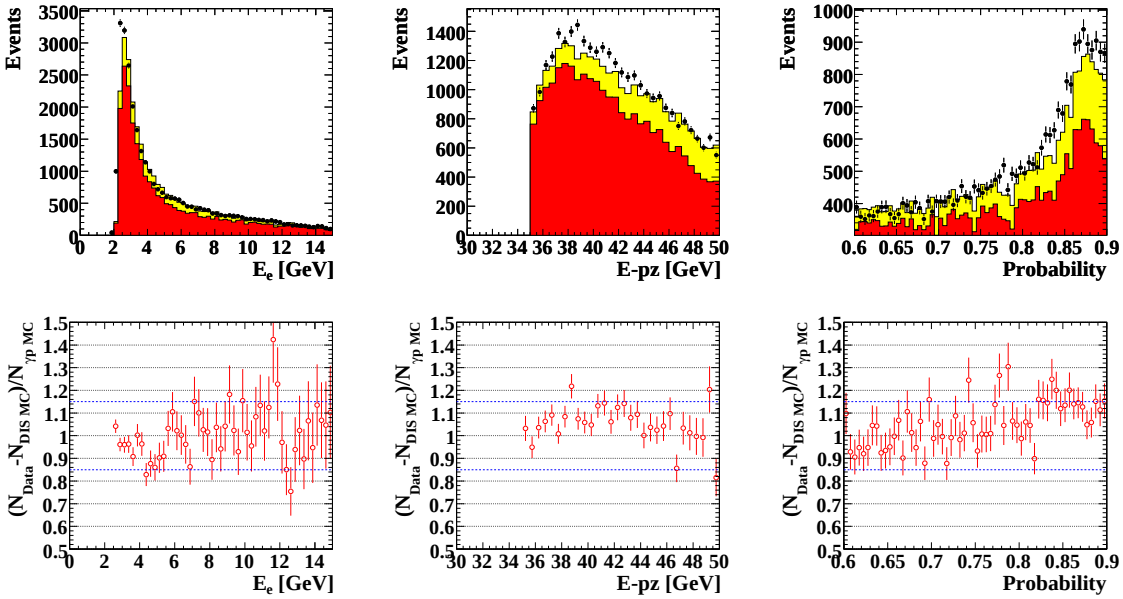

Figure 5.7: Distributions of photoproduction enriched sample for MER. The points are data and the yellow and the red histograms are the DIS+γp and the γp MCs, respectively.

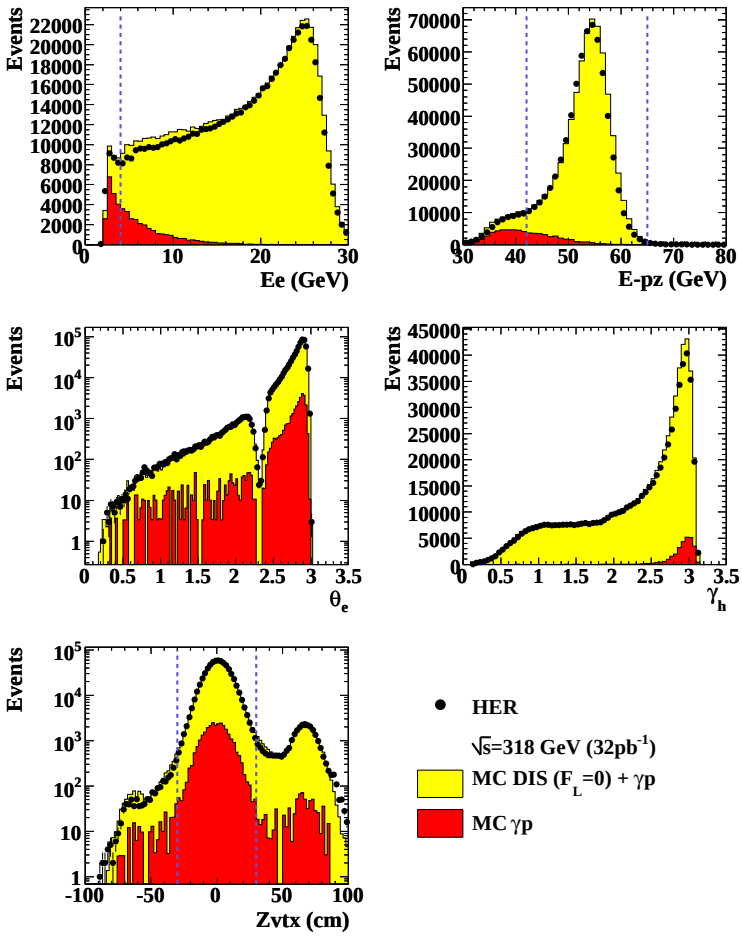

Figure 5.8: HER event distribution.

5.5 Event distribution

The distributions of various measured variables are shown in Fig. 5.8, Fig. 5.9 and Fig. 5.10 for each HER, LER and MER sample respectively. The shown variables are E'_e, $E-p_z$, θ_e, γ_h and Z_{vtx}. In the plot, all the DIS selections except for the one related to the variable are applied. The dotted lines in the plots are the threshold lines used in the event selections.

The contamination of the photoproduction events is seen at low E'_e and low $E-p_z$. In the $E-p_z$, the DIS peak at 55 GeV has a tail at low value due to radiative events. In the ZEUS coordination, higher value of θ_e or γ_h corresponds to the rear direction. The θ_e distribution has a steep rise as expected from $\frac{1}{Q^4}$ dependence of the DIS cross section. The dip at $\theta_e \sim 2.2$ rad is caused by the B/RCAL super crack cut in the event selection. The Z_{vtx} distribution is well described by the MC including satellite distributions for all the HER, LER and MER samples.

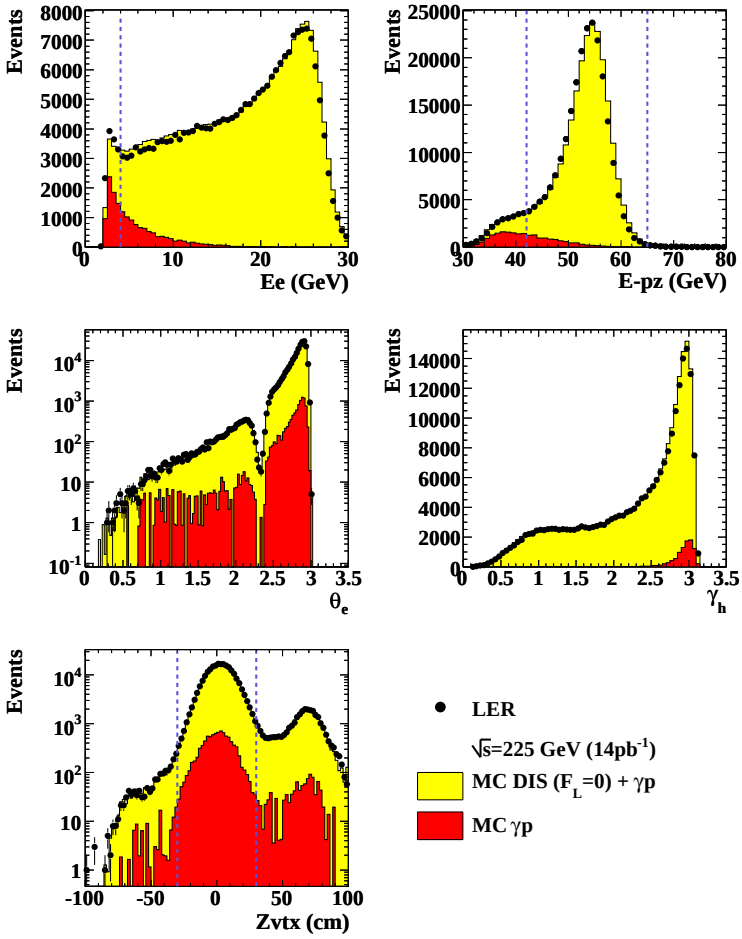

Figure 5.9: LER event distribution.

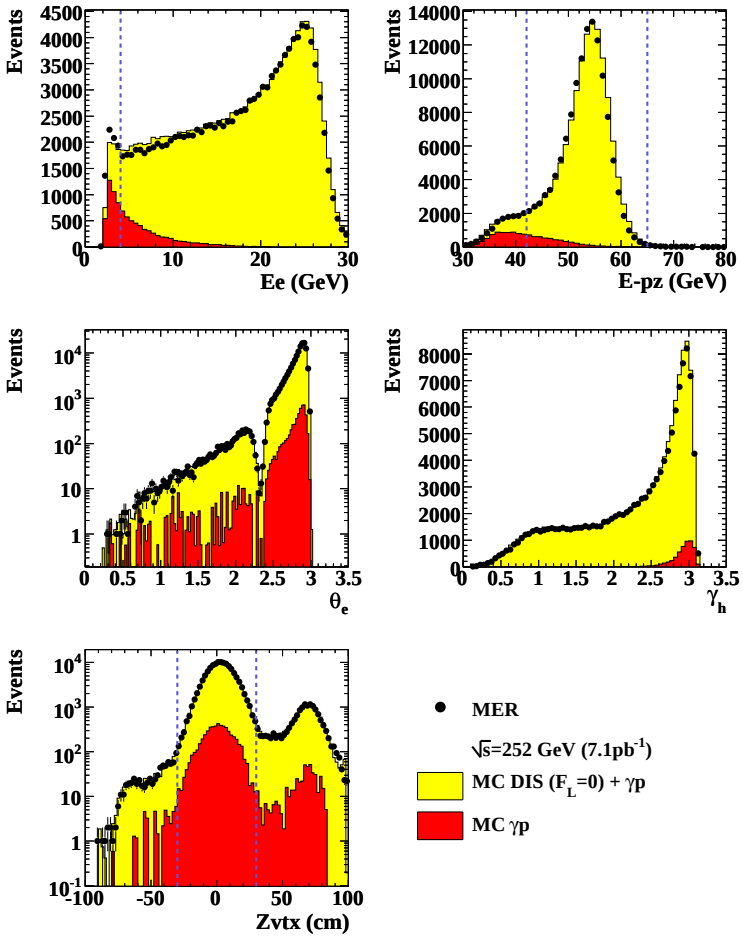

Figure 5.10: MER event distribution.

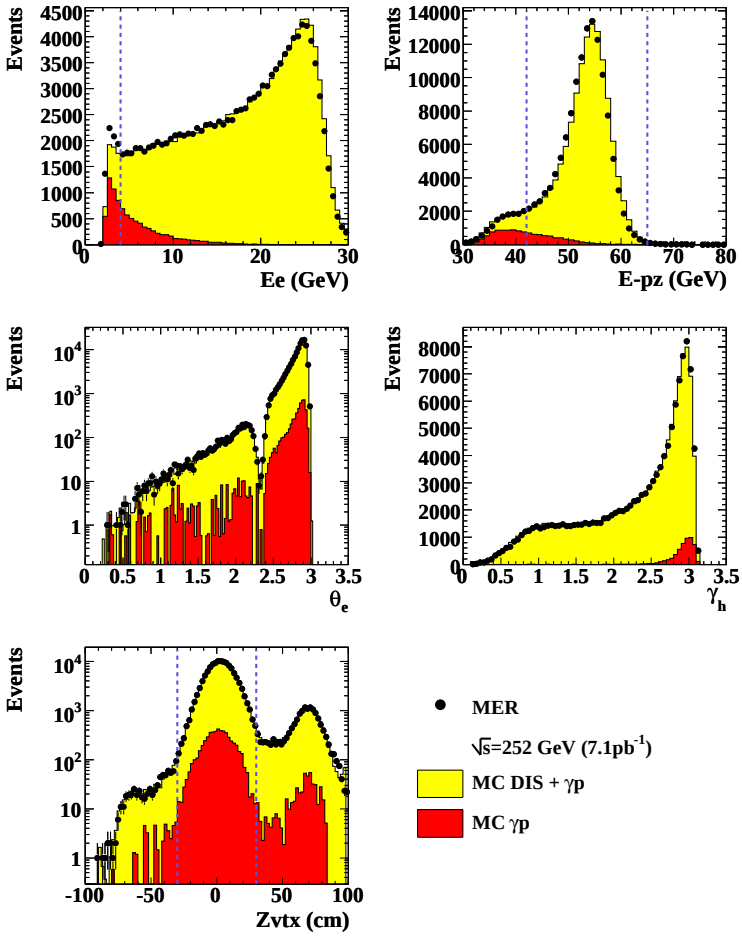

Figure 5.11: MER event distribution with the F_L weighted MC.

At low E'_e, the data has less events than the MC in all three sample. This is explained by the fact that the MC is generated with $F_L = 0$ and does not have F_L contribution. With non-zero F_L the DIS cross section is predicted to decrease at high y. In Fig. 5.11, the MER event distribution, the MC distributions are weighted with the F_L contribution predicted from a pQCD calculation. The low E'_e region is then well described by the MC. The same effect is also seen in the HER and LER distributions.

In summary, the MC describes the data distributions well. The description of variables related to the both electron and hadron sides of the DIS agrees with the data.

Chapter 6

Cross section measurement

In this chapter, the DIS reduced cross sections, $\tilde{\sigma}$ (Eq. 4.1), are extracted from each HER, LER and MER data. The covered kinematic regions are $20 < Q^2 < 130$ GeV^2 and $0.09 < y < 0.78$. This study extends the measurements towards the high y region (~ 0.75) comparing to the previous analysis [51]. The high y measurements are the first step to extract F_L.

Due to the electroweak radiation, the kinematics of the scattering are changed and the apparent cross section differs from the Born level cross section. The radiative effect can be corrected as

$$\left.\frac{d^2\sigma}{dxdQ^2}\right|_{\text{app.}} = \frac{d^2\sigma^{\text{Born}}}{dxdQ^2}(1+\delta_r(x,Q^2)), \tag{6.1}$$

where δ_r represents for electroweak radiative corrections. The DIS Born level process can be written with a simplest diagram with a boson exchange. Higher order diagrams bring some corrections on the cross section and the kinematic reconstruction. $O(\alpha)$-corrections include initial state radiation (ISR) and final state radiation (FSR) and interference terms from vertex correction and from propagator correction. The cross sections are presented at the Born level, i.e. without electroweak radiation, to allow easy comparison with the QCD calculations.

6.1 Bin definition

Generally, the bins are defined with the kinematic variables. The number of bins is determined by the acceptance, the resolution and the statistics of the measurement. The experimental conditions such as detector acceptance limit the measurable region on the kinematic plane. The finite resolution of the detector causes smearing of the reconstructed kinematic variables so that events migrate among the bins.

In this measurement, the bins for the cross section measurement are defined in the (y, Q^2) plane to have a good coverage in the high y region. Since the proton beam energy is not explicitly used in the determination of y and Q^2 with the Electron method, it is natural to use the same bin definition for all HER, LER and MER measurement. The lowest Q^2 value is limited by the radius cut of R_{CTD} and the highest y value is limited by the measurable lowest energy of the positron. Though

events with $E_e > 4$ GeV are selected in Chapter 5, the measurement is restricted in the region with $E_e > 6$ GeV to have less influence from any imperfect understanding of photoproduction backgrounds as described in Sec. 6.3.2. The widths of bins are determined with the resolutions of Q^2 and y reconstruction, which are shown in Fig. 4.3 and Fig. 4.4. As discussed in Sec. 4.2, the Electron method gives good resolution of both Q^2 and y at high y but the y resolution gets worse at low y so that wider bins are defined at the low y region.

The bins are defined over $20 < Q^2 < 130$ GeV^2 and $0.09 < y < 0.78$. The quality of each bin can be estimated from the MC using the values of *Efficiency*, *Purity* and *Acceptance* which have following definitions;

$$\textit{Efficiency} = \frac{\text{the number of measured and generated events in the bin}}{\text{the number of generated events in the bin}}, \tag{6.2}$$

$$\textit{Purity} = \frac{\text{the number of measured and generated events in the bin}}{\text{the number of measured events in the bin}} \tag{6.3}$$

$$\textit{Acceptance} = \frac{\text{the number of measured events in the bin}}{\text{the number of generated events in the bin}} \tag{6.4}$$

where the measured events are the events which pass the event selections and are reconstructed in the bin. *Efficiency* shows how many events remain in the original bin after the analysis. The value reflects the net result of both selection efficiency and migration effect, which comes from finite resolution. *Purity* estimates migration effect. Its value is given by looking how many events among the measured events are originally generated in the bin, i.e. the number of events not migrating to other bins. *Acceptance* shows the acceptance effect from the event selections. The effect needs to be considered at the extraction of cross section as described in the Sec. 6.2. The value of *Acceptance* may be over 100 % due to the migration and its definition. These three variables have a relation of $\textit{Efficiency} = \textit{Acceptance} \times \textit{Purity}$.

They are shown for each bin in Fig. 6.1, Fig. 6.2 and Fig. 6.3. The acceptance is generally good for most of the bins and is acceptable (> 20 %) except for a low y bin. All the bins have moderate purity around 50 % .

6.2 Unfolding

The procedure to extract the cross section from the number of events in a bin is called *unfolding*. The number of DIS events in a bin is related to the cross section as

$$N_{\text{meas.}} = \mathcal{L} \int_{\Delta y, \Delta Q^2} a \cdot \frac{d^2\sigma^{\text{BORN}}}{dxdQ^2}(1+\delta_r)dxdQ^2, \tag{6.5}$$

where $\mathcal{L}$, a and δ_r represent for integrated luminosity, acceptance of the measurement and electroweak radiative correction. In this analysis, the differential cross sections at the Born level are extracted by the bin-by-bin procedure based on the one-step unfolding. The procedure takes account of background subtraction, radiative correction, acceptance correction and bin-centering correction in a single step as described below.

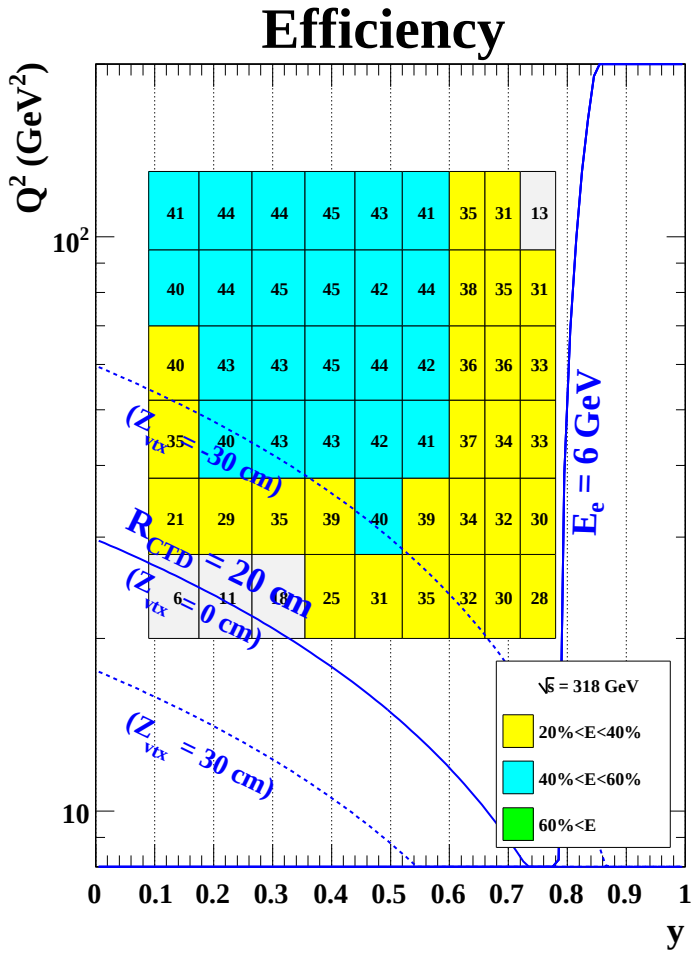

Figure 6.1: Efficiency of bins for the cross section measurement, shown for the HER sample.

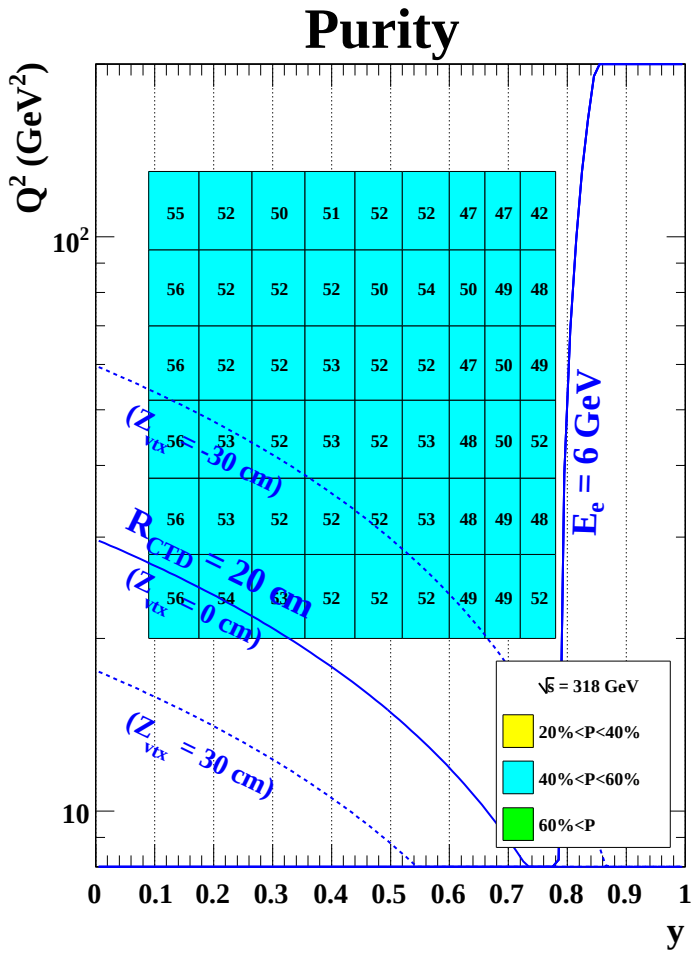

Figure 6.2: Purity of bins for the cross section measurement, shown for the HER sample.

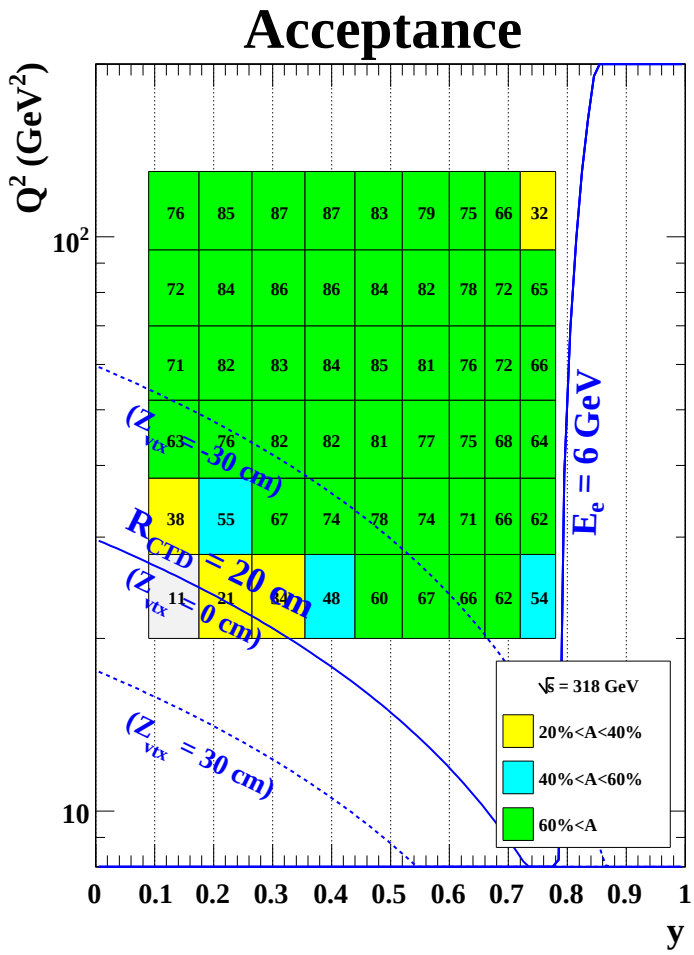

Figure 6.3: Acceptance of bins for the cross section measurement, shown for the HER sample.

The photoproduction background events are statistically subtracted as,

$$N_{\text{meas.}} = N_{\text{data}} - N_{\gamma p}, \tag{6.6}$$

where N_{data} is the number of data in a bin. $N_{\gamma p}$ is the number of photoproduction MC events in a bin, estimated as discussed in Sec. 5.4. The estimated contamination of the photoproduction events, $\frac{N_{\gamma p}}{N_{\text{data}}}$ is shown in Fig. 6.4. The amounts of contamination are quite similar between the three samples and are reasonably suppressed to 17 % at maximum, which is seen in the bin with the lowest Q^2 and the highest y.

The imperfection of the detector results into limited acceptance and event migration. The effect is corrected relying on the Monte Carlo simulation as

$$\frac{1}{A} = \frac{N^{\text{rad.}}_{\text{gen.}}}{N_{\text{MC}}}, \tag{6.7}$$

where $N^{\text{rad.}}_{\text{gen.}}$ is the number of generated events in the bin with radiative effect and N_{MC} is the number of measured DIS MC events in the bin.

At this point, the integrated radiative cross section can be obtained as

$$\sigma^{\text{rad.}}|_{\Delta y \Delta Q^2} = \frac{N_{\text{meas.}}}{\mathcal{L}A}. \tag{6.8}$$

Since the event generators take account of radiative effect, the simulation is also used for the radiative correction to extract the Born cross sections. The corrections is applied by the factor of

$$\frac{1}{C_{\text{rad.}}} = \frac{N^{\text{BORN}}_{\text{true}}}{N^{\text{rad.}}_{\text{gen.}}} \tag{6.9}$$

where $N^{\text{BORN}}_{\text{true}}$ is the number of DIS events in a bin with the true kinematics when the radiative effect is switched off.

To extract cross section at certain kinematic point, the integrated cross section should be corrected by the bin-centering correction, C_{center}. The amount of correction is estimated by the theoretical cross sections as

$$\left.\frac{d^2\sigma^{\text{BORN,theo}}}{dxdQ^2}\right|_{\text{bin center}} = C_{\text{center}} \frac{1}{\Delta y \Delta Q^2} \int_{\Delta y, \Delta Q^2} \frac{d^2\sigma^{\text{BORN,theo}}}{dxdQ^2} dxdQ^2. \tag{6.10}$$

With all these corrections, the cross section can be extracted as

$$\frac{d^2\sigma^{\text{BORN}}}{dxdQ^2} = \frac{C_{\text{center}}}{\Delta y \Delta Q^2} \cdot \frac{1}{C_{\text{rad.}}} \cdot \sigma^{\text{rad.}}|_{\Delta y \Delta Q^2} \tag{6.11}$$

$$= \frac{N_{\text{meas.}}}{\mathcal{L}\Delta y \Delta Q^2} \cdot \frac{1}{AC_{\text{rad.}}} \cdot C_{\text{center}}. \tag{6.12}$$

Therefore, by substituting the correction factors for Eq. 6.12,

$$\frac{d^2\sigma^{\text{BORN}}}{dxdQ^2} = \frac{N_{\text{meas.}}}{\mathcal{L}\Delta y \Delta Q^2} \cdot \frac{N^{\text{BORN}}_{\text{true}}}{N_{\text{MC}}} \cdot \frac{\left.\frac{d^2\sigma^{\text{BORN,theo}}}{dxdQ^2}\right|_{\text{bin center}}}{\frac{1}{\Delta y \Delta Q^2} \int_{\Delta y, \Delta Q^2} \frac{d^2\sigma^{\text{BORN,theo}}}{dxdQ^2} dxdQ^2}. \tag{6.13}$$

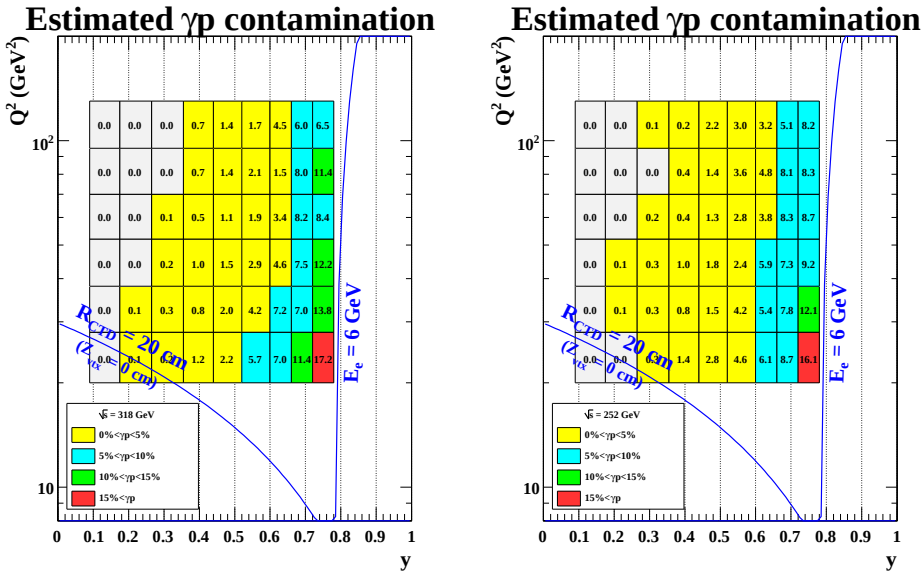

(a) HER

(b) MER

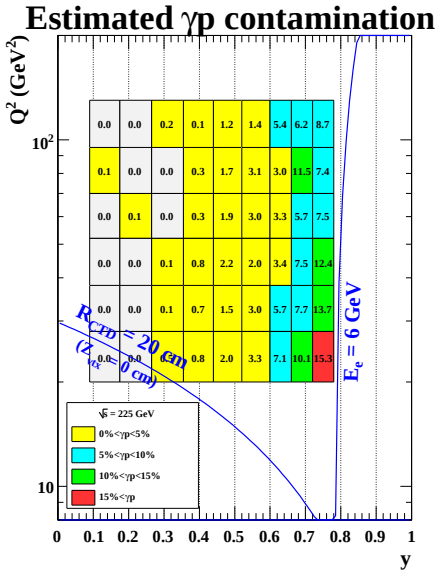

(c) LER

Figure 6.4: Estimated γp contamination.

Using the relation of

$$N_{\rm true}^{\rm BORN} = \mathcal{L} \int_{\Delta y, \Delta Q^2} \frac{d^2\sigma^{\rm BORN,theo}}{dxdQ^2} dxdQ^2, \tag{6.14}$$

the Eq. 6.13 can be written as

$$\frac{d^2\sigma^{\rm BORN}}{dxdQ^2} = \frac{N_{\rm data} - N_{\gamma p}}{N_{\rm MC}} \cdot \frac{d^2\sigma^{\rm BORN,theo}}{dxdQ^2}\bigg|_{\rm bin\ center}. \tag{6.15}$$

The bin-by-bin correction method is valid only if the models in the theory describes the reality in the data. Therefore, the procedure needs to be iterated by modifying the MC cross sections according to the obtained result until the result gets stable.

For the first extraction, the theoretical cross section, $\frac{d^2\sigma^{\rm BORN,theo}}{dxdQ^2}$, is calculated by HECTOR [53]. At LO of QCD, the cross section calculated by HECTOR agrees with that used in the MC generated by HERACLES so that Eq. 6.14 is satisfied.

As shown at the end of this chapter, the first extracted cross sections well agree with the predictions using the ZEUS-JETS PDFs

$$\tilde{\sigma}_{\rm meas.} \simeq \tilde{\sigma}_{\rm ZJ}, \tag{6.16}$$

where $\tilde{\sigma}_{\rm meas.}$ and $\tilde{\sigma}_{\rm ZJ}$ are the measured and the ZEUS-JETS cross sections. Therefore, the stability of the result is checked as following using the MER sample. The cross section in the DIS MC is reweighted according to the ZEUS-JETS prediction and the analysis is redone as

$$\tilde{\sigma}'_{\rm meas.} = \frac{N_{\rm data} - N_{\gamma p}}{N_{\rm MC}^{\rm ZJ\ rew.}} \cdot \tilde{\sigma}_{\rm ZJ}, \tag{6.17}$$

where $N_{\rm MC}^{\rm ZJ\ rew.}$ represents for the reweighted MC. The differences between $\tilde{\sigma}_{\rm meas.}$ and the secondary extracted $\tilde{\sigma}'_{\rm meas.}$ are found as less than 0.7 %. The result is stable at the first extraction and the iterative procedure is not necessary.

6.3 Systematic checks

6.3.1 Sources of correlated systematic uncertainties

Following issues are considered in evaluation of systematic uncertainties.

- Positron finding
  The uncertainty from the positron finding is evaluated by comparing two different set of $P_{\rm Sira}$ criteria. The change affects both efficiency and purity of the positrons. The criteria are

  $$\begin{aligned} &\text{Exponential criterion} &&: P_{\rm Sira} > 0.9 - 1.5 \cdot \exp\left(-\frac{E_e}{2.5}\right), \\ &&&\quad \text{with the lowest boundary of 0.6} \\ &\text{Linear criterion} &&: P_{\rm Sira} > 0.9. \end{aligned}$$

Positron finding	different probability cut
Positron energy scale	$\pm 1\%$ at $E'_e \geq 15$ GeV, increasing to $\pm 2\%$ at $E'_e = 5$ GeV
x position of positron	± 4 mm
y position of positron	± 4 mm
CTD Hit Fraction threshold	± 0.1
MVD Hit Fraction threshold	± 0.1
Z_{vtx} threshold	$\lvert Z_{vtx} \rvert < 50$ cm
$E - p_z$ threshold	± 2 GeV
Normalization of photoproduction MC	$\pm 15\%$

Table 6.1: The sources of the systematic uncertainties and their evaluation.

- Positron energy scale (Sec. 4.3.2)
- Position reconstruction of positrons (Sec. 4.3.3)
- Road utility
  The uncertainty of the utility and imperfection of its description by MC results in uncertainty of the $\mathcal{F}_{\rm Hit}$. It is evaluated by loosening and tightening the threshold of each CTD and MVD $\mathcal{F}_{\rm Hit}$ by ± 0.1. By tightening the threshold by 0.1, events with $\mathcal{F}_{\rm Hit} = \frac{2}{3}$ in the CTD or $\mathcal{F}_{\rm Hit} = \frac{1}{2}$ for the MVD will be rejected.
- Vertex description
  The imperfection of the Z_{vtx} description by the MC causes the different detector acceptance and hence the different luminosity between the data and MC. The systematic effect is estimated by loosen the Z_{vtx} requirement as

  $$\text{Reconstructed event vertex with } \lvert Z_{vtx} \rvert < 50 \text{ cm}.$$

- $E - p_z$ threshold
  The $E - p_z$ threshold determines each amount of photoproduction background and DIS events with ISR in the selected sample. Its uncertainty is evaluated by changing the value of threshold by ± 2 GeV. The value comes from hadronic energy resolution.
- Normalization of photoproduction MC (Sec. 5.4)

All the sources considered in the total systematic uncertainty of the measurement are listed in Table 6.1. For each systematic source, the cross sections are extracted by changing the analysis condition as listed in the table and the deviations from the standard analysis are considered as uncertainty from the source. The extracted uncertainties are symmetrized by taking the larger absolute value for each source and added in quadrature to give the total systematic uncertainty.

The uncertainty from the luminosity measurement is 2.6 %. It should be added in the cross section measurement.

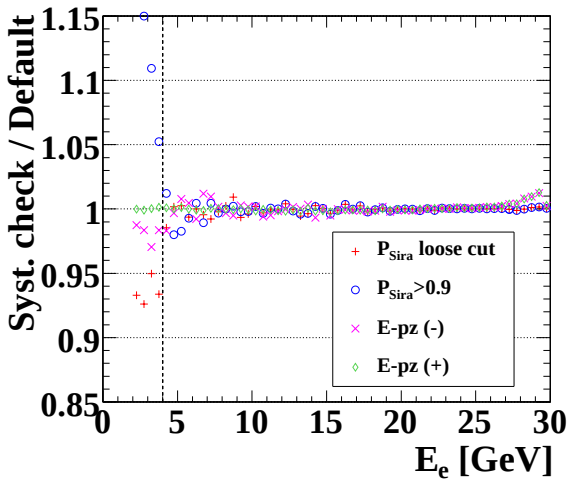

Figure 6.5: Systematic checks as a function of E'_e.

6.3.2 Low E'_e behaviour

During the evaluation of systematic uncertainties, it is seen that the low E'_e region is sensitive to some of the systematic sources. This is why the (y, Q^2) bins are defined at $E'_e > 6$ GeV in Sec. 6.1.

In Figure 6.5, the stability of the measurement is shown as a function of E'_e. It shows the deviation of the ratio of the data to the MC from the standard DIS selection due to the change of the $E - p_z$ or P_{Sira} criteria as done in evaluation of systematic effect. The sample used in the figure is the DIS sample without the E'_e selection.

While the deviations are well within 1 % for $E'_e \gtrsim 6$ GeV, they get larger for lower E'_e and expand just under the E'_e threshold of 4 GeV in this measurement. Since both P_{Sira} and $E - p_z$ selections relate to photoproduction events, the low E'_e behaviour of the deviations may come from imperfection in the understanding of photoproduction backgrounds. Therefore, the measurement is restricted to $E'_e > 6$ GeV as already written in Sec. 6.1.

6.3.3 Trigger efficiency

Trigger efficiency is automatically taken into account by the acceptance calculation. Even the medium-Q^2 trigger logic is loose enough so that its efficiency is quite high and more than 99 %. The validity of the trigger simulation is tested by cross checking the events passing the sub-logics such as *Risoe* and *good track* at the FLT and electron finding and $\sum^{\mathrm{ex.lir}}(E - p_z)$ at the TLT. The check of the SLT and the TLT is also done by using the sample for another measurement [54]. All the FLT, SLT and TLT are well described by the simulation. The uncertainty associated to the trigger is not considered.

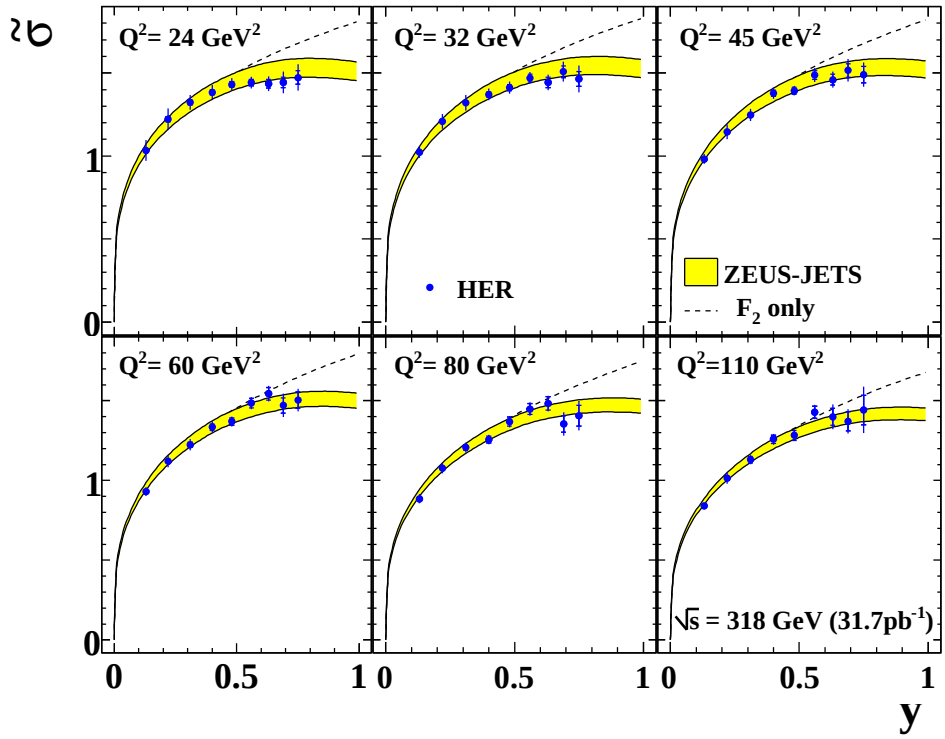

Figure 6.6: HER reduced cross sections.

6.4 Results

The values of measured reduced cross sections and their uncertainties are summarized in Tables A.1, A.2 and A.3 and shown in Fig. 6.6, Fig. 6.7 and Fig. 6.8 for the HER, LER and MER sample, respectively. They are shown for each Q^2 bin as a function of y. The measurement is extended to higher y, where the factor on the F_L contribution to the reduced cross section, $\frac{y^2}{Y_+}$, is larger, comparing to the previous analysis [51].

The total correlated systematic uncertainties include the sources listed in Sec. 6.3.1. Uncertainty from each source is shown in Appendix B. The largest uncertainty originates in the energy scale uncertainty. At high y with low Q^2, the uncertainty from the normalization of the photoproduction MC is also significant. The uncertainty of 2.6 % from the luminosity measurement is not shown in the tables and the figures and to be included in the total uncertainties.

The measured cross sections are compared with the pQCD predictions using the ZEUS-JETS PDFs [12]. They well agree with the predictions. In the figure, dotted lines are F_2, i.e. the prediction with $F_L = 0$. The deviation from the line corresponds to the F_L contribution to the reduced cross section. It is seen that there should be non-zero F_L to describe the DIS cross sections by the pQCD.

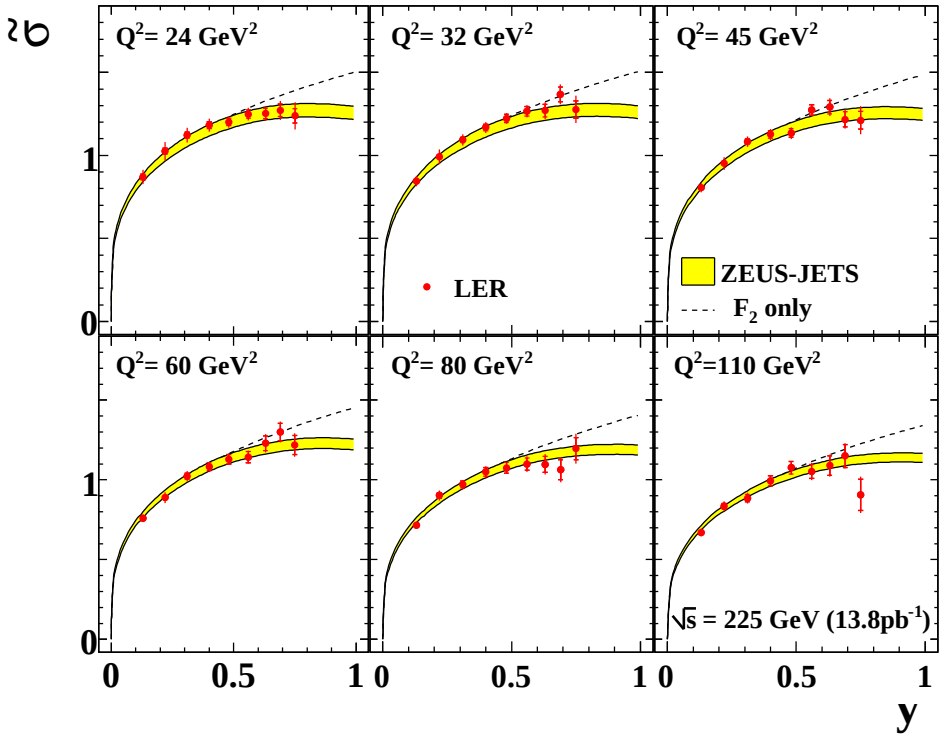

Figure 6.7: LER reduced cross sections.

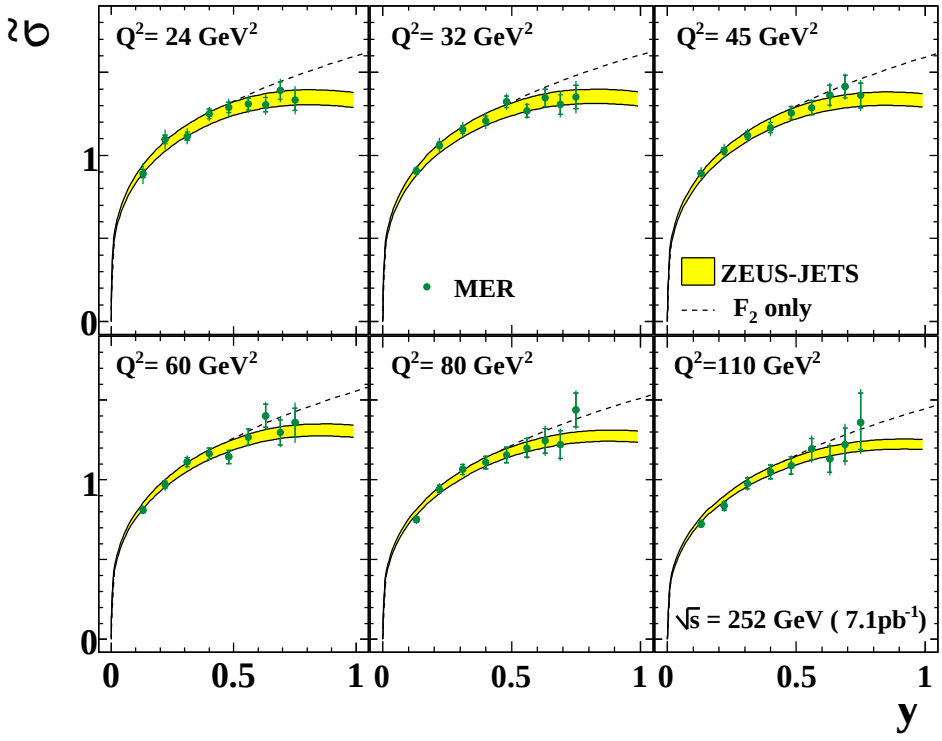

Figure 6.8: MER reduced cross sections.

Chapter 7

Extraction of F_L

In the previous chapter, it is seen that the DIS reduced cross section at high y tends to be flatter which indicates F_L is non zero. In this chapter, the direct measurement of F_L is performed. F_L is extracted from the comparison of the reduced cross sections at the same (x, Q^2) with different y, hence the comparison between the HER, MER and LER cross sections at the same (x, Q^2).

7.1 Reduced cross section measurement with common (x, Q^2) bins

The bins are redefined to be optimized for the direct F_L measurement, such that they allow better comparison of the cross sections and have acceptable statistical uncertainties. The bins are defined on the (y, Q^2) plane. For each HER, LER and MER sample, the bin boundary is set to have the same kinematic range in the (x, Q^2) space, with consideration of the both resolution and statistics.

Efficiency, *Purity* and *Acceptance* for each bin are shown in Fig. 7.1, Fig. 7.2 and Fig. 7.3, respectively. Each bin has acceptable acceptance and purity above 20 % and 30 %, respectively.

The reduce cross section is extracted for each bin using the same bin-by-bin correction described in Sec. 6.2. The cross sections are shown in Table A.4.

7.2 Normalization of data sets

Since the differences between the cross sections measured from the HER, LER and MER samples give F_L, the direct F_L measurement is quite sensitive to the relative uncertainty of normalization between the samples. The possible causes of the uncertainty are relative differences of the luminosity measurement and also imperfect estimation of the amount of events from the satellite bunches, since the machine setting and hence beam condition was different between the samples. To compensate the relative differences of the normalization, the cross sections of each sample are scaled based on the study with the low y events, where the F_L contribution to the cross section is negligible and hence the cross sections with the same (x, Q^2) should be the same.

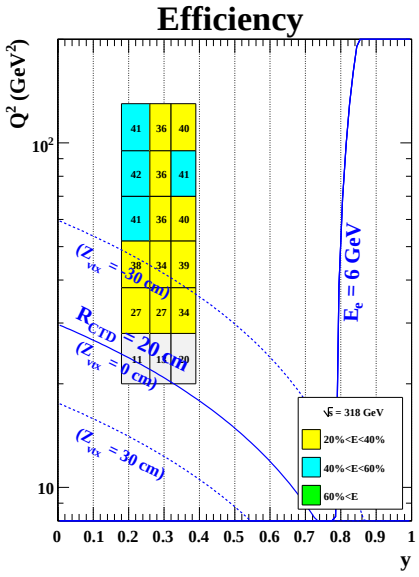

(a) HER

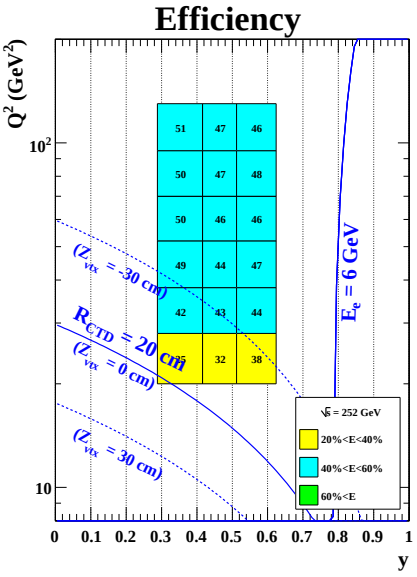

(b) MER

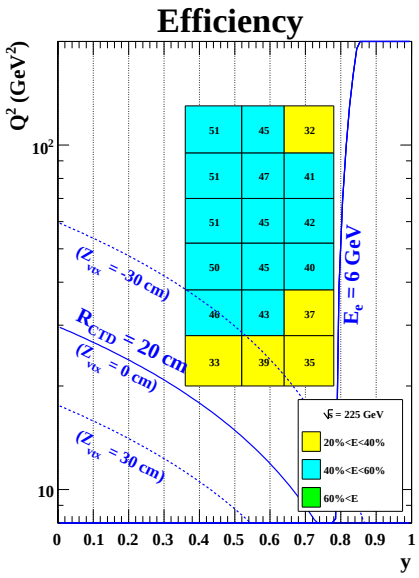

(c) LER

Figure 7.1: Efficiency.

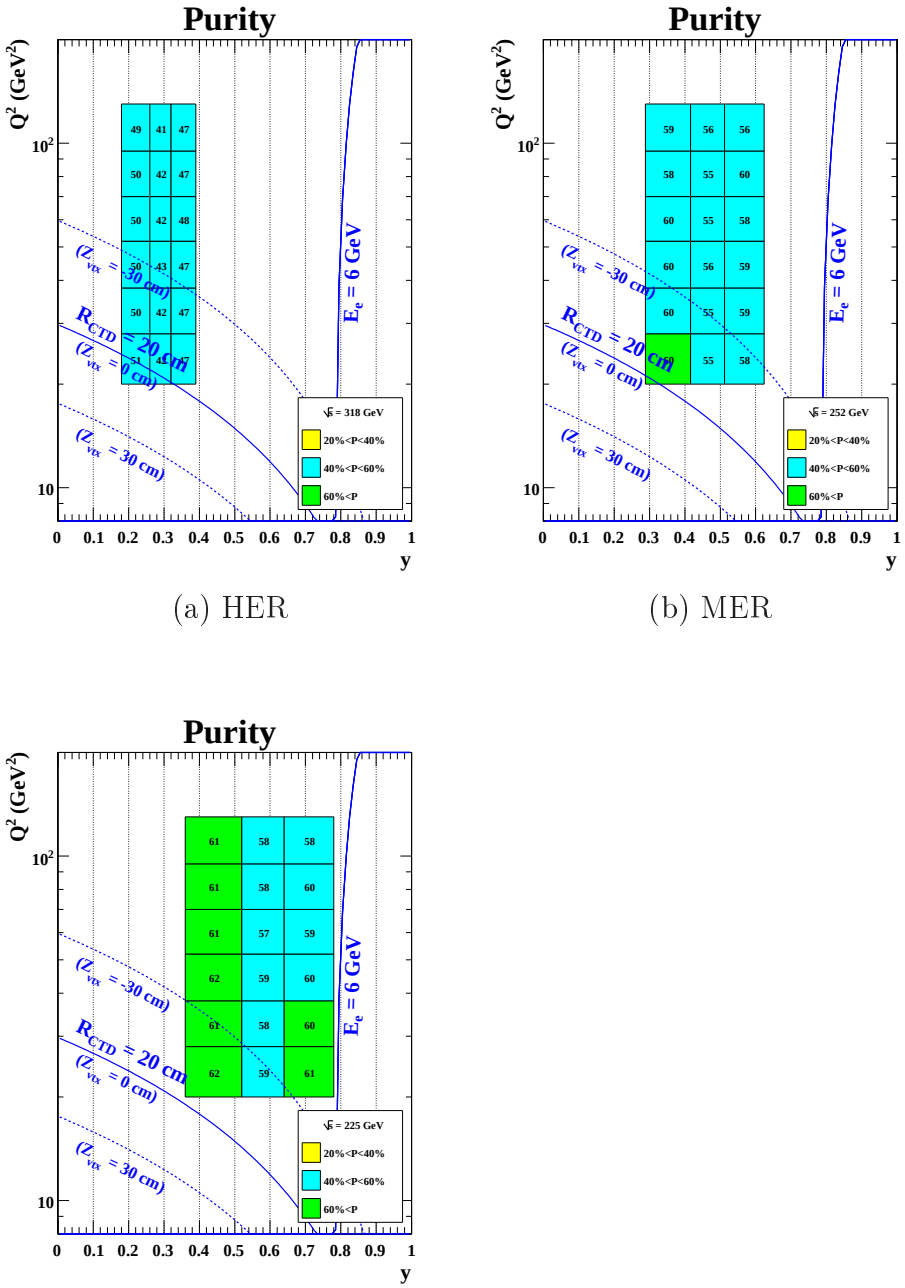

(a) HER

(b) MER

(c) LER

Figure 7.2: Purity.

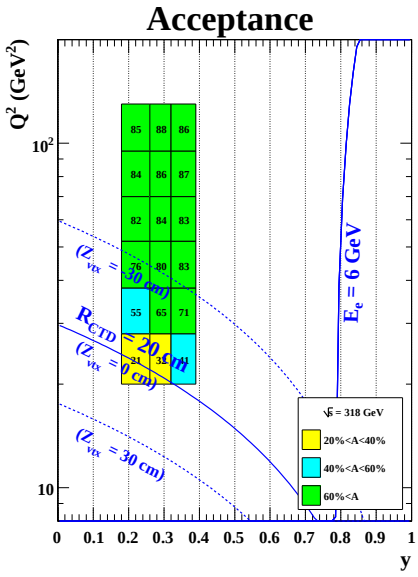

(a) HER

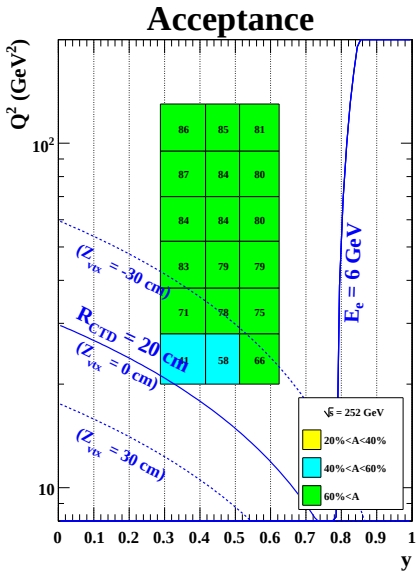

(b) MER

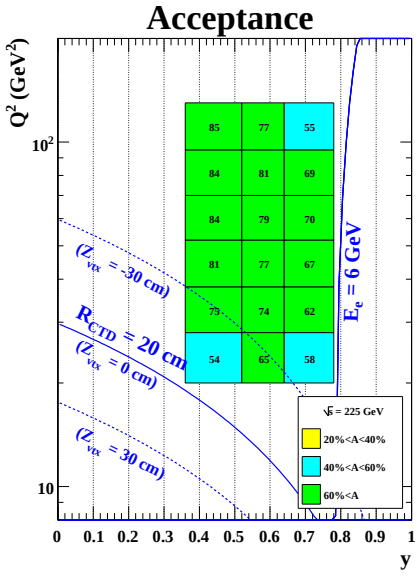

(c) LER

Figure 7.3: Acceptance.

The study is done with the samples selected by the DIS selections described in Chapter 5 but with a looser kinematic cut of $y_{JB} > 0.03$ instead of $y_{JB} > 0.05$. Kinematic reconstruction is done by the Double Angle method, which gives the better resolution at the low y region. A bin is defined for each different energy sample as

$$\begin{array}{lll} \text{HER:} & 20 < Q^2_{DA} < 130 \text{ GeV}^2 & 0.060 < y_{DA} < 0.120 \\ \text{MER:} & 20 < Q^2_{DA} < 130 \text{ GeV}^2 & 0.096 < y_{DA} < 0.192 \\ \text{LER:} & 20 < Q^2_{DA} < 130 \text{ GeV}^2 & 0.120 < y_{DA} < 0.240. \end{array}$$

They cover the same kinematic range on the (x, Q^2) plane. The integrated cross sections in the bins should be the same for all the samples if $F_L = 0$. Non zero and positive F_L decreases the cross section. Based on the predicted cross section using the ZEUS-JETS PDFs, which have good agreement with the measured cross section as shown in Sec. 6.4, decrease of the integrated cross section is estimated as -0.08 %, -0.20 % and -0.31 % for each HER, MER and LER bin respectively. It is found that whether their effect is considered or not in the following procedure makes little difference on the final extracted F_L. The difference is about 10 % of F_L statistical uncertainty at most. Therefore, the effect from non zero F_L is not taken into account in this normalization study.

The normalization factor w_{norm} is determined as

$$\frac{1}{w_{\text{norm}}} = \frac{N_{\text{data}}}{N_{\text{MC}} + N_{\gamma p}}, \tag{7.1}$$

where the MC cross section is taken as a standard value of normalization. The following normalization factors are extracted from this study;

$$\begin{array}{ll} \text{HER} & \frac{1}{w_{\text{norm}}} = 0.967 \pm 0.004 \\ \text{LER} & \frac{1}{w_{\text{norm}}} = 1.006 \pm 0.006 \\ \text{MER} & \frac{1}{w_{\text{norm}}} = 0.989 \pm 0.008. \end{array}$$

The values of w_{norm} are applied to the reduced cross sections which are summarized in Table A.4.

7.3 Extraction of F_L and results

After applying the normalization factors w_{norm} described in the previous section, the HER, LER and MER reduced cross sections are linearly fitted in each bin by

$$\tilde{\sigma} = p_1 - p_2 \frac{y^2}{Y_+}, \tag{7.2}$$

where p_1 and p_2 correspond to F_2 and F_L respectively. The fit results are shown in Fig. 7.4. While the fit is mainly constrained by the HER and LER cross sections due to their better statistics, the MER cross sections show the consistency with the linear fit.

The extracted F_L is summarized in Table A.5. As in the cross section measurement, the sources listed in Sec. 6.3.1 are considered as sources of correlated systematic uncertainties. Effects from each systematic source is shown in Appendix B. The largest uncertainty comes from uncertainty of the energy scale of positrons.

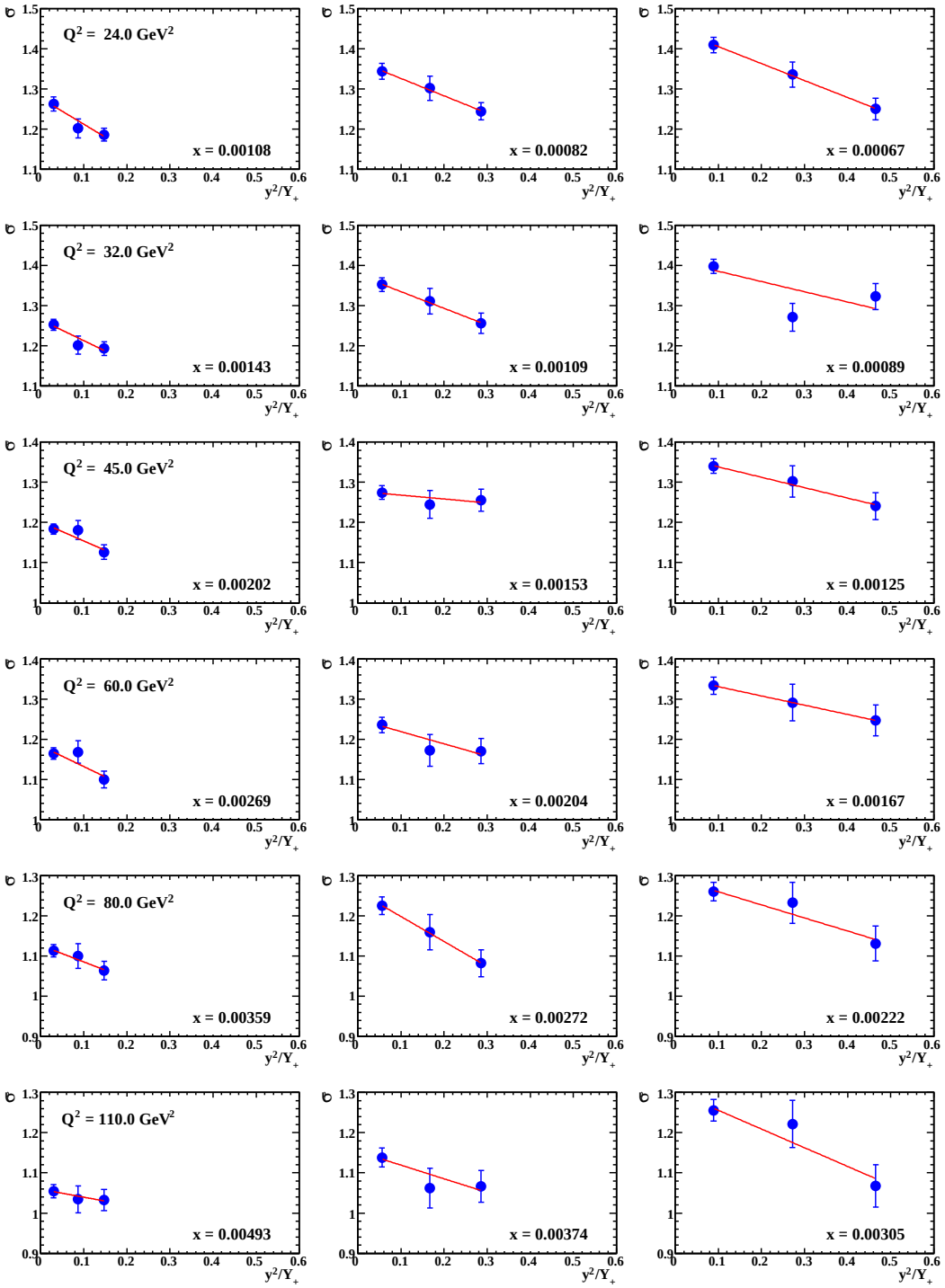

Figure 7.4: Linear fit on the reduced cross sections for each bin.

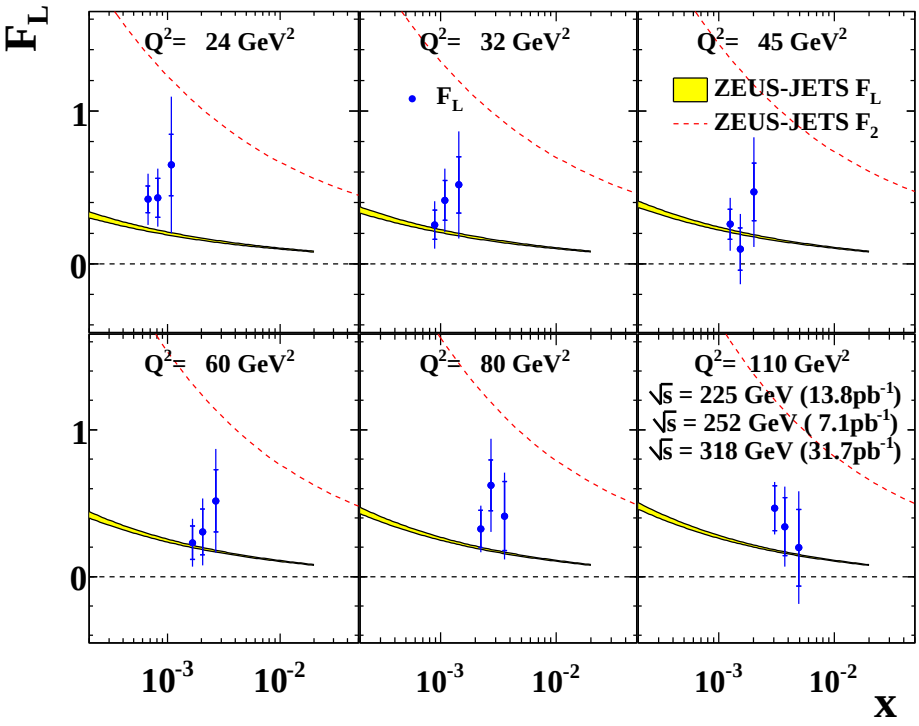

Figure 7.5: F_L compared with the prediction from ZEUS-JETS PDFs.

7.4 Discussion

The measured F_L is shown in Fig. 7.5. This is the one of the first direct F_L measurements at low x[1]. The F_L is separated from the reduced cross section for the first time without model dependence. The measurement demonstrates that the F_L is non zero in this kinematic region and is well smaller than F_2 which is shown by the prediction using ZEUS-JETS PDFs. This agrees with the condition of Eq. 2.19, which is given only by F_L definition.

In the figure, the measurement is compared with pQCD predictions using ZEUS-JETS PDFs. As described in Sec. 2.5.2, the scaling violation, i.e. Q^2 dependence, of F_2 can be indirectly related to the gluon density in the pQCD view. In the ZEUS-JETS PDF, the gluon density mainly determined by the Q^2 dependence of $\tilde{\sigma}$ measured by the ZEUS experiment at lower y. In pQCD, F_L can also be written using gluon density as Eq. 2.35 and hence can be calculated using the known gluon density. The solid lines in the plot are the F_L calculated in such a way using the gluon density of the ZEUS-JETS PDF. The measured F_L are consistent with the lines. Since F_L has a direct sensitivity to the gluon density according to the QCD and the sensitivity is different from the that of scaling violation, the observed consistency demonstrates the validity of the pQCD

[1]Resent result from the H1 collaboration is in [55].

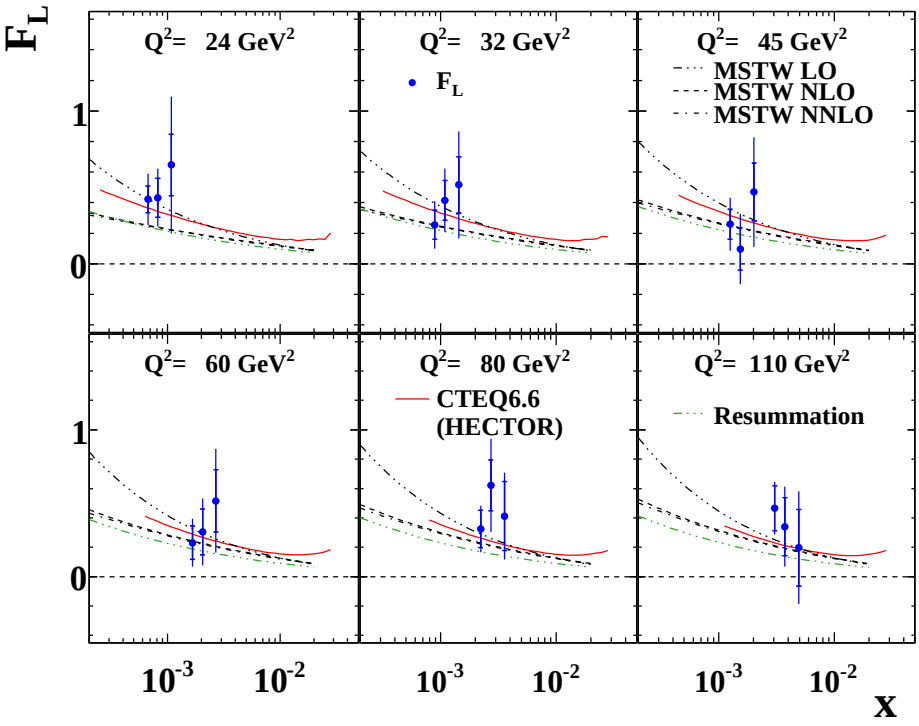

Figure 7.6: F_L compared with various predictions.

framework of the description of proton structure. This also gives a new support for applicability of currently used gluon density to the pQCD calculation of other QCD processes.

The comparison with different F_L predictions is also shown in Fig. 7.6. The predictions are F_L calculated by HECTOR using CTEQ6.6 PDF [56], LO, NLO and NNLO predictions from MSTW [57] and prediction from NLL BFKL resummation fit [58]. Although the measured F_L does not yet have a sensitivity to the detailed differences between the predictions, the measurement agrees with the stability between the various predictions and shows that current approaches can be accepted for further understanding of low x physics.

The observed consistency with pQCD gives one note on the measured cross sections in the previous chapter. In this F_L extraction, the y range of the used HER cross sections is $0.18 < y < 0.39$ while the HER cross section measurement itself is done over $0.09 < y < 0.78$ as described in the previous chapter. The HER cross sections for $0.39 < y < 0.78$ are not used in the F_L extraction but they have sensitivity to F_L at lower x than the measured F_L. Since the consistency between the measured F_L and the pQCD prediction is seen, those cross sections can be analyzed within the pQCD framework. It would be a indirect analysis but, together with results from other DIS measurements, the cross sections measured at high y in the previous chapter can be used for further studies on F_L and gluon distribution.

Chapter 8

Conclusion

The longitudinal structure function F_L has been directly measured for the $24 \leq Q^2 \leq 110$ GeV^2 and $6.7 \cdot 10^{-4} \leq x \leq 4.9 \cdot 10^{-3}$. This is one of the first measurements of F_L at such low x region.

The measurement is based on the e^+p scattering data with three different beam energies collected in 2006 and 2007 with the ZEUS detector at HERA. A key issue in this measurement is accurate reconstruction of the scattered positron with low energy and low angle. A hit finder is newly developed to improve the positron identification. Background events due to positron misidentification are understood with data.

The measured F_L is found to be non zero. The non zero F_L derives from the gluon dynamics in the proton according to the QCD. The agreement between the measured F_L and the pQCD prediction is seen. This demonstrates the validity of pQCD description of the proton structure. It also supports the applicability of the gluon density in the pQCD, which is indirectly determined from the scaling violation, to another pQCD calculation.

The positron-proton inclusive DIS reduced cross sections are also measured at three different center-of-mass energies, namely $\sqrt{s} = 318$, 252 and 225 GeV, for the same Q^2 range as the F_L measurement and $0.13 \leq y \leq 0.75$ extending to higher y than the previous inclusive DIS measurement. Since the pQCD description is consistent with the measured F_L, observed flattening of reduced cross sections at high y is interpreted as F_L contribution. Though high y cross sections at HER is not used for the direct F_L measurement, they have sensitivity to F_L at lower x than the direct measurement. The measured cross sections in this thesis allow further studies on F_L through the QCD global analysis.

Appendix A

Tables

In this chapter, measured reduced cross sections and F_L are listed in tables. In the tables, statistical uncertainties are given in absolute value and systematic uncertainties are give in %. Each systematic source corresponds to;

δ_1	Energy scale
δ_2	Normalization of photoproduction MC
δ_3	Electron finding
δ_4	x position
δ_5	y position
δ_6	Z_{vtx}
δ_7	Threshold of $\sum(E - p_z)$
δ_8	MVD hit fraction
δ_9	CTD hit fraction

A.1 HER reduced cross sections

Q^2	y	x	$\tilde{\sigma}$	δ_{stat}	$\delta_{\text{syst.}}$	δ_1		δ_2		δ_3		δ_4		δ_5		δ_6	δ_7		δ_8		δ_9	
(GeV^2)				(abs.)	(%)	+	−	+	−	+	−	+	−	+	−		+	−	+	−	+	−
24	0.13	1.82e-03	1.034	0.015	5.93	2.82	-1.27	0.00	0.00	0.06	0.06	-0.26	3.50	2.84	-1.29	-0.31	0.00	0.00	-0.58	-0.28	2.54	-0.48
24	0.22	1.08e-03	1.221	0.015	5.19	2.97	-3.66	-0.01	0.01	0.03	0.03	-0.99	2.14	1.59	-0.51	-0.34	-0.04	0.00	-1.16	-0.00	2.24	-0.45
24	0.31	7.63e-04	1.322	0.015	3.15	1.95	-1.75	-0.04	0.04	-0.04	-0.05	-1.80	1.55	0.72	-0.70	-0.19	-0.06	0.34	-0.72	0.01	1.31	-0.22
24	0.40	5.92e-04	1.383	0.016	2.89	1.26	-1.69	-0.19	0.19	0.26	0.26	-0.44	1.04	0.33	-0.59	0.02	-0.83	0.20	-0.81	-0.06	1.61	-0.29
24	0.48	4.93e-04	1.431	0.018	2.27	-0.03	-1.08	-0.34	0.34	-0.05	-0.09	-0.11	0.67	0.23	-0.10	-0.22	-0.30	-0.59	-0.45	0.03	1.66	-0.15
24	0.56	4.23e-04	1.442	0.021	2.02	0.66	1.02	-0.90	0.90	0.38	0.42	0.08	0.57	-0.14	-0.17	-0.25	0.19	-0.17	-0.06	0.10	1.26	-0.01
24	0.63	3.76e-04	1.435	0.026	2.55	-0.19	-1.21	-1.12	1.12	-0.16	-0.75	0.17	1.16	0.22	0.53	-0.03	-0.35	-0.92	-0.45	-0.29	0.74	-0.33
24	0.69	3.43e-04	1.443	0.032	3.98	1.81	1.15	-1.92	1.92	-0.01	-1.08	-1.14	1.77	-0.10	0.94	0.16	0.55	-1.23	0.30	-0.38	1.41	-0.57
24	0.75	3.16e-04	1.473	0.041	4.62	1.09	-0.79	-3.11	3.11	0.43	-0.87	-1.28	0.65	0.41	0.09	-0.43	0.78	-2.26	-1.52	0.51	0.56	0.13
32	0.13	2.43e-03	1.024	0.009	3.33	2.58	-1.93	0.00	0.00	0.05	0.05	-1.15	1.29	0.73	-0.40	-0.26	0.00	0.00	-0.98	-0.05	1.09	-0.16
32	0.22	1.43e-03	1.208	0.011	3.62	2.65	-3.07	-0.02	0.02	0.01	0.01	-0.61	1.17	0.12	-0.48	-0.20	-0.04	0.00	-0.69	-0.05	1.25	0.02
32	0.31	1.02e-03	1.320	0.013	3.37	2.76	-1.88	-0.05	0.05	-0.04	-0.05	0.09	1.04	0.23	-0.21	-0.14	0.03	0.15	-0.89	-0.05	1.32	-0.27
32	0.40	7.89e-04	1.371	0.016	2.30	1.35	-1.63	-0.13	0.13	0.22	0.20	0.41	0.65	0.34	-0.02	-0.25	-0.04	-0.06	-0.17	-0.08	1.39	-0.33
32	0.48	6.57e-04	1.412	0.019	2.28	0.47	0.21	-0.31	0.31	-0.87	-0.83	0.40	0.71	0.01	-0.28	0.04	-0.56	-0.05	-1.16	0.06	1.37	-0.28
32	0.56	5.63e-04	1.470	0.023	1.80	-0.92	0.41	-0.66	0.66	0.14	0.09	-0.39	0.48	0.21	-0.10	-0.04	0.07	-0.16	-0.62	0.07	1.12	-0.06
32	0.63	5.01e-04	1.443	0.032	2.33	0.05	-0.22	-1.16	1.16	-0.16	0.07	-0.51	-1.06	-0.57	-0.69	-0.48	0.53	0.52	0.99	-0.38	0.97	0.08
32	0.69	4.57e-04	1.508	0.035	3.31	-1.13	-1.61	-1.12	1.12	0.33	0.71	-1.36	-0.76	-0.70	-0.36	-0.54	0.72	-0.30	-1.59	0.32	0.97	-0.10
32	0.75	4.21e-04	1.464	0.044	4.53	1.53	-1.13	-2.40	2.40	-0.63	-2.58	-1.02	-0.91	-0.85	0.20	0.20	-0.88	-0.35	-1.65	0.50	-0.70	-0.13
45	0.13	3.41e-03	0.981	0.008	2.94	2.36	-1.94	0.00	0.00	0.04	0.04	-0.02	0.76	0.03	-0.40	-0.25	0.00	0.00	-0.57	-0.03	1.39	-0.19
45	0.22	2.02e-03	1.145	0.011	3.77	3.11	-3.23	0.00	0.00	0.03	0.03	0.38	0.79	0.39	-0.34	-0.22	0.02	0.00	-1.01	-0.17	1.41	-0.21
45	0.31	1.43e-03	1.247	0.013	2.77	2.22	-1.58	-0.03	0.03	0.10	0.09	-0.17	0.95	0.09	-0.13	-0.32	0.15	-0.29	-0.42	0.06	1.21	0.01
45	0.40	1.11e-03	1.378	0.018	2.11	1.08	-1.29	-0.16	0.16	-0.09	-0.23	-0.30	0.99	0.14	-0.05	-0.15	0.37	-0.32	-0.53	0.01	1.13	-0.17
45	0.48	9.24e-04	1.393	0.021	1.36	-0.06	-0.03	-0.22	0.23	-0.19	-0.12	-0.91	0.49	0.01	-0.29	-0.17	-0.32	-0.16	-0.42	0.09	0.73	-0.36
45	0.56	7.92e-04	1.488	0.026	2.20	-1.06	-0.16	-0.44	0.44	-0.62	-0.85	-1.05	-0.52	-0.24	-0.09	-0.45	-0.52	0.18	-0.91	0.27	0.57	-0.04
45	0.63	7.04e-04	1.460	0.034	2.39	0.49	0.45	-0.72	0.72	-1.44	-0.90	-1.44	0.79	-0.15	0.11	-0.24	-0.07	0.28	0.01	0.15	-0.25	-0.79
45	0.69	6.43e-04	1.515	0.041	3.54	-1.37	-0.77	-1.22	1.22	0.16	1.08	0.65	1.06	0.01	-0.02	0.18	-0.34	-0.31	-2.56	0.68	-0.49	0.21
45	0.75	5.92e-04	1.490	0.048	3.77	1.81	0.90	-2.08	2.08	0.13	0.56	0.26	-0.01	-0.32	-0.13	-0.69	1.68	0.06	-0.80	-0.56	-1.47	-0.92
60	0.13	4.55e-03	0.930	0.009	2.76	2.19	-1.36	0.00	0.00	0.03	0.03	-0.32	0.98	0.29	0.11	-0.34	0.00	0.00	-0.80	0.05	1.01	-0.08
60	0.22	2.69e-03	1.121	0.012	3.17	2.64	-2.90	0.00	0.00	0.05	0.05	-0.86	0.46	-0.14	-0.28	-0.27	-0.04	0.00	-0.37	0.03	0.78	-0.15
60	0.31	1.91e-03	1.224	0.016	2.52	2.20	-2.08	-0.01	0.01	0.14	0.14	-0.78	0.16	0.13	0.00	-0.38	0.15	-0.14	-0.51	0.23	0.65	-0.13
60	0.40	1.48e-03	1.334	0.020	2.18	1.31	-1.73	-0.07	0.07	0.02	0.06	-0.52	-0.88	-0.49	0.06	-0.26	-0.09	-0.06	-0.63	0.02	0.50	0.07
60	0.48	1.23e-03	1.370	0.024	1.36	-0.35	-0.48	-0.17	0.17	-0.26	-0.24	-0.25	0.16	-0.15	-0.06	-0.27	0.19	0.05	-1.14	0.02	-0.20	-0.18
60	0.56	1.06e-03	1.485	0.030	1.51	0.14	-0.54	-0.30	0.30	0.16	0.27	0.14	0.69	0.19	-0.33	-0.26	-0.59	-0.22	-0.74	-0.19	0.54	0.15
60	0.63	9.39e-04	1.544	0.040	1.78	0.04	0.67	-0.53	0.53	0.87	0.39	0.34	0.31	0.21	-0.06	-0.03	-0.02	-0.64	0.15	-0.52	-0.92	-0.16
60	0.69	8.57e-04	1.471	0.048	3.81	-2.04	0.78	-1.33	1.33	-0.26	-0.30	-1.91	0.12	-0.05	-0.06	-0.42	1.59	-0.15	1.29	-0.33	0.58	-0.68
60	0.75	7.89e-04	1.504	0.051	3.35	0.82	-0.55	-1.38	1.38	-1.02	-0.83	-0.91	0.48	0.45	-0.12	0.14	-1.58	1.48	0.91	0.22	-1.79	1.28
80	0.13	6.07e-03	0.885	0.010	3.04	2.67	-2.38	0.00	0.00	0.03	0.03	-0.38	-0.02	-0.31	-0.31	-0.43	0.00	0.00	-0.94	0.18	0.87	-0.03
80	0.22	3.59e-03	1.078	0.013	2.71	2.64	-2.21	0.00	0.00	0.00	0.00	-0.24	0.23	-0.12	0.33	0.06	-0.04	0.00	-0.38	0.05	0.20	0.05
80	0.31	2.54e-03	1.207	0.018	2.16	1.54	-1.88	0.00	0.00	-0.10	-0.10	-0.04	0.37	-0.04	-0.07	-0.66	0.44	-0.14	-0.45	-0.10	0.37	-0.01
80	0.40	1.97e-03	1.256	0.022	1.72	1.41	-0.90	-0.11	0.11	-0.24	-0.25	-0.35	0.80	0.16	-0.41	-0.11	0.11	-0.13	-0.17	-0.07	0.17	-0.12

Table A.1: HER reduced cross sections.

Q^2 (GeV^2)	y	x	$\tilde{\sigma}$	δ_{stat} (abs.)	$\delta_{\text{syst.}}$ (%)	δ_1 +	δ_1 −	δ_2 +	δ_2 −	δ_3 +	δ_3 −	δ_4 +	δ_4 −	δ_5 +	δ_5 −	δ_6	δ_7 +	δ_7 −	δ_8 +	δ_8 −	δ_9 +	δ_9 −
80	0.48	1.64e-03	1.369	0.028	1.57	0.69	-1.00	-0.22	0.22	-0.07	0.01	0.58	0.28	-0.03	0.31	-0.40	-0.21	-0.17	-0.14	0.13	0.87	0.38
80	0.56	1.41e-03	1.448	0.034	1.66	0.78	1.18	-0.33	0.33	0.21	0.23	0.23	0.52	0.44	0.47	-0.67	0.34	0.06	-0.33	-0.21	0.18	-0.07
80	0.63	1.25e-03	1.483	0.043	1.57	0.91	-0.13	-0.23	0.23	-0.55	-0.85	-0.12	-0.11	-0.14	-0.21	-0.28	-0.55	0.08	-0.51	-0.10	-0.43	-0.03
80	0.69	1.14e-03	1.354	0.052	3.89	-1.75	-1.43	-1.31	1.31	-0.10	0.65	1.29	0.62	-0.25	-0.09	-0.54	2.63	-0.12	-0.44	-0.15	0.90	0.15
80	0.75	1.05e-03	1.406	0.065	4.70	2.93	2.56	-1.94	1.93	-0.75	0.60	-0.07	-0.60	0.12	-0.00	-0.03	-0.04	-0.57	-2.33	-0.17	-0.20	1.75
110	0.13	8.34e-03	0.842	0.011	1.59	1.55	-1.42	0.00	0.00	0.01	0.01	-0.10	0.10	0.13	-0.10	-0.13	0.00	0.00	-0.04	-0.03	0.28	0.04
110	0.22	4.93e-03	1.015	0.015	3.17	2.71	-3.15	0.00	0.00	-0.03	-0.01	0.17	0.23	-0.14	0.02	0.03	-0.01	0.00	-0.01	0.09	0.07	0.17
110	0.31	3.50e-03	1.130	0.019	1.81	1.70	-1.72	0.00	0.00	0.03	0.03	0.26	0.14	0.12	-0.01	-0.32	0.23	-0.25	-0.15	0.10	-0.16	0.02
110	0.40	2.71e-03	1.258	0.026	1.83	1.62	-1.09	-0.10	0.10	-0.04	-0.01	-0.11	0.17	-0.02	-0.07	-0.04	-0.72	-0.14	-0.24	0.04	0.27	-0.02
110	0.48	2.26e-03	1.283	0.031	1.26	0.15	-0.93	-0.21	0.21	-0.06	0.04	0.04	-0.29	-0.03	-0.00	0.06	0.51	-0.65	-0.32	0.17	0.26	-0.01
110	0.56	1.94e-03	1.428	0.038	1.65	0.20	0.64	-0.26	0.26	0.09	0.21	-0.07	-0.23	0.06	-0.24	-0.38	-1.10	0.45	-0.36	0.05	-0.79	0.40
110	0.63	1.72e-03	1.399	0.053	3.98	-3.35	1.04	-0.71	0.71	0.42	0.85	-0.25	-1.03	-0.35	-0.50	-0.25	-0.37	-0.84	0.65	-0.32	-0.95	0.46
110	0.69	1.57e-03	1.371	0.059	3.44	-1.42	1.09	-0.97	0.97	0.05	0.55	-1.26	0.83	-0.59	0.18	-0.22	-2.15	0.64	-0.33	0.77	1.18	-0.75
110	0.75	1.45e-03	1.442	0.092	7.78	-1.74	-2.33	-1.04	1.04	0.11	-1.24	1.36	2.22	2.42	-0.10	-0.02	-0.26	-6.17	-0.63	-0.90	-1.65	-1.17

Table A.1: HER reduced cross sections.

A.2 LER reduced cross sections

Q^2 (GeV^2)	y	x	$\tilde{\sigma}$	δ_{stat} (abs.)	$\delta_{\text{syst.}}$ (%)	δ_1 +	δ_1 −	δ_2 +	δ_2 −	δ_3 +	δ_3 −	δ_4 +	δ_4 −	δ_5 +	δ_5 −	δ_6	δ_7 +	δ_7 −	δ_8 +	δ_8 −	δ_9 +	δ_9 −
24	0.13	3.64e-03	0.869	0.017	4.54	2.54	-2.06	0.00	0.00	0.09	0.09	-1.71	2.58	2.05	-1.89	-0.26	0.00	0.00	-0.48	-0.02	1.74	-0.76
24	0.22	2.15e-03	1.025	0.018	5.16	2.98	-3.30	0.00	0.00	-0.12	-0.12	-1.72	1.91	1.91	-1.32	-0.23	0.06	0.00	-0.10	-0.14	2.89	-0.66
24	0.31	1.53e-03	1.122	0.019	3.52	2.32	-1.90	-0.07	0.07	0.06	0.13	-1.19	1.82	1.33	-0.73	0.31	0.20	-0.18	-0.49	0.07	1.25	-0.23
24	0.40	1.18e-03	1.182	0.020	2.75	1.86	-1.22	-0.12	0.12	0.19	0.23	-0.40	0.46	0.84	-0.60	0.45	0.02	0.19	-0.69	-0.12	1.56	-0.26
24	0.48	9.86e-04	1.201	0.022	2.13	-0.40	-0.18	-0.31	0.31	-0.28	-0.40	0.01	0.74	0.61	-0.55	-0.01	-0.48	0.55	-0.68	-0.02	1.57	-0.31
24	0.56	8.45e-04	1.249	0.024	2.39	0.45	-0.63	-0.51	0.51	0.67	0.45	-0.16	1.39	0.07	-0.32	-0.34	-0.27	-0.56	-0.55	-0.19	1.35	-0.10
24	0.63	7.51e-04	1.252	0.032	2.13	0.35	0.82	-1.15	1.14	-0.16	-0.83	0.27	0.66	0.01	-0.14	-0.57	0.66	-0.52	-0.39	0.04	0.69	-0.27
24	0.69	6.86e-04	1.272	0.037	3.41	-1.00	-1.33	-1.69	1.69	-0.46	-0.06	-1.34	-0.52	0.01	-0.65	-0.13	-0.21	0.45	0.82	-0.01	1.91	-0.54
24	0.75	6.31e-04	1.239	0.044	5.57	0.92	-0.04	-2.70	2.70	0.84	0.91	-0.41	-0.64	0.29	-0.46	-0.43	4.44	1.20	1.06	1.13	0.52	-0.30
32	0.13	4.85e-03	0.845	0.011	3.36	2.65	-1.93	0.00	0.00	0.01	0.01	-0.48	1.02	0.90	-0.55	0.01	0.00	0.00	-0.20	-0.11	1.54	-0.29
32	0.22	2.87e-03	0.991	0.014	4.20	3.05	-3.05	-0.00	0.00	-0.02	-0.02	-0.48	1.00	0.61	-0.59	-0.27	0.02	0.00	-1.10	-0.08	2.38	-0.35
32	0.31	2.04e-03	1.094	0.017	2.80	1.89	-2.07	-0.02	0.02	0.02	0.02	-0.42	0.69	0.33	-0.77	-0.04	0.33	-0.25	-0.06	-0.07	1.54	-0.11
32	0.40	1.58e-03	1.168	0.020	2.20	1.34	-1.60	-0.11	0.11	-0.09	-0.09	-0.01	0.86	0.44	-0.42	0.09	-0.48	-0.01	-0.24	-0.02	1.02	-0.12
32	0.48	1.31e-03	1.223	0.024	1.96	-0.40	-0.05	-0.23	0.23	0.08	0.09	-0.27	0.90	0.05	-0.15	0.25	0.16	0.60	1.04	-0.22	1.14	-0.17
32	0.56	1.13e-03	1.266	0.028	1.90	0.73	0.31	-0.46	0.46	-0.59	-0.39	-0.17	-0.03	0.08	0.22	-0.04	-0.93	0.27	-0.10	-0.26	1.22	-0.04
32	0.63	1.00e-03	1.270	0.038	2.81	0.41	-1.12	-0.90	0.90	-0.88	-1.22	-0.58	-0.34	0.11	0.10	0.83	-0.23	0.09	-1.43	0.70	1.09	0.66

Table A.2: LER reduced cross sections.

Q^2 (GeV^2)	y	x	$\tilde{\sigma}$	δ_{stat} (abs.)	$\delta_{\text{syst.}}$ (%)	δ_1 +	δ_1 −	δ_2 +	δ_2 −	δ_3 +	δ_3 −	δ_4 +	δ_4 −	δ_5 +	δ_5 −	δ_6	δ_7 +	δ_7 −	δ_8 +	δ_8 −	δ_9 +	δ_9 −
32	0.69	9.14e-04	1.368	0.045	2.97	-0.70	0.83	-1.24	1.24	-0.39	-1.52	-0.14	-0.38	-0.33	0.83	0.26	-0.30	-0.63	-1.68	0.89	-0.36	0.25
32	0.75	8.41e-04	1.277	0.052	4.91	0.48	-1.09	-2.38	2.38	-0.32	0.96	-0.38	0.64	0.33	0.10	0.02	3.85	-0.41	-0.36	-0.10	0.30	0.91
45	0.13	6.83e-03	0.805	0.010	3.09	2.35	-1.82	-0.00	0.00	0.06	0.06	0.10	1.14	0.60	-0.36	0.43	0.00	0.00	-0.15	-0.04	1.46	-0.05
45	0.22	4.03e-03	0.952	0.013	3.69	2.97	-2.72	-0.00	0.00	0.06	0.06	0.02	1.05	0.23	-0.22	-0.22	0.07	0.00	0.18	-0.20	1.88	-0.25
45	0.31	2.86e-03	1.083	0.017	2.35	1.47	-1.88	-0.01	0.01	0.04	0.04	0.18	0.57	0.08	0.09	0.16	0.46	-0.21	-0.42	-0.16	1.10	-0.17
45	0.40	2.22e-03	1.126	0.021	2.28	1.43	-1.79	-0.11	0.11	0.04	-0.02	-0.86	0.61	-0.43	-0.10	-0.03	0.49	-0.16	-0.32	0.09	0.84	0.02
45	0.48	1.85e-03	1.134	0.026	2.01	0.06	-0.92	-0.33	0.33	0.20	0.23	-1.33	-0.31	-0.48	0.01	-0.13	-0.10	-0.38	-0.60	0.32	0.71	-0.07
45	0.56	1.59e-03	1.274	0.031	1.38	0.28	0.67	-0.31	0.31	0.43	0.72	-0.46	-0.52	-0.37	0.31	0.10	0.25	-0.13	-0.47	-0.07	0.24	-0.35
45	0.63	1.41e-03	1.291	0.041	2.61	-0.25	-0.07	-0.53	0.53	-1.07	-0.91	0.14	0.11	-0.36	-0.03	-0.56	-1.05	-0.74	-1.93	-0.25	0.04	0.19
45	0.69	1.29e-03	1.217	0.046	2.72	1.16	0.26	-1.22	1.22	-0.05	0.06	0.23	0.42	-0.44	0.39	0.90	-1.11	1.39	-0.53	-0.62	1.05	0.42
45	0.75	1.18e-03	1.212	0.054	5.40	-1.52	3.52	-2.12	2.12	-0.61	-0.29	-0.97	-0.83	-0.62	0.44	1.54	-0.67	2.71	-0.82	0.48	0.09	0.50
60	0.13	9.10e-03	0.760	0.011	2.92	2.38	-1.82	0.00	0.00	0.12	0.12	-0.83	0.63	-0.21	-0.16	-0.16	0.00	0.00	-0.98	0.13	1.05	-0.16
60	0.22	5.38e-03	0.889	0.015	3.39	2.76	-2.96	-0.02	0.02	-0.03	-0.03	-0.56	0.87	-0.06	0.19	-0.24	-0.05	0.00	-0.13	0.09	1.37	-0.20
60	0.31	3.82e-03	1.022	0.020	2.48	2.13	-1.81	0.00	0.00	0.09	0.09	-0.77	0.05	0.21	-0.07	-0.04	-0.15	0.27	-0.55	0.14	0.77	0.04
60	0.40	2.96e-03	1.083	0.025	1.67	1.22	-0.69	-0.05	0.05	-0.08	-0.08	-0.10	0.11	0.25	0.13	0.62	-0.42	-0.51	-0.51	0.16	0.55	0.25
60	0.48	2.47e-03	1.129	0.030	1.33	0.71	-0.41	-0.29	0.29	0.21	0.27	-0.40	0.31	0.39	-0.65	0.03	0.33	-0.37	-0.45	-0.41	0.12	0.42
60	0.56	2.11e-03	1.143	0.035	1.84	-0.85	-0.06	-0.46	0.46	0.28	0.59	-0.17	-0.06	0.14	-0.86	-0.19	0.68	-0.77	-0.60	-0.48	0.61	0.26
60	0.63	1.88e-03	1.229	0.047	2.77	-1.75	1.23	-0.52	0.52	0.17	-0.72	-0.65	0.67	0.04	0.30	1.32	-0.59	0.77	-0.75	0.22	0.60	0.18
60	0.69	1.71e-03	1.300	0.055	2.65	0.04	-0.77	-0.91	0.91	-0.42	-0.51	0.04	1.25	0.71	-0.41	-1.51	-0.30	-0.66	0.58	0.01	-0.51	0.40
60	0.75	1.58e-03	1.218	0.059	3.61	1.70	-0.12	-1.21	1.21	0.36	2.08	-0.51	-1.07	0.51	-0.22	0.70	0.37	-0.39	0.33	0.58	-1.41	-0.67
80	0.13	1.21e-02	0.716	0.012	2.20	2.01	-1.62	-0.01	0.01	0.03	0.03	-0.38	-0.49	-0.02	-0.11	0.21	0.00	0.00	-0.40	-0.00	0.62	-0.06
80	0.22	7.17e-03	0.902	0.017	3.00	2.13	-2.87	0.00	0.00	0.07	0.07	-0.66	-0.72	-0.13	-0.05	-0.13	0.06	0.00	-0.39	0.17	0.18	0.09
80	0.31	5.09e-03	0.971	0.021	1.98	1.71	-1.71	0.00	0.00	0.09	0.09	-0.07	0.54	-0.20	-0.09	-0.04	0.14	0.24	-0.68	0.08	0.40	0.10
80	0.40	3.94e-03	1.049	0.028	2.20	1.55	-1.75	-0.05	0.05	0.10	0.10	0.15	-0.09	0.11	-0.13	-0.98	0.20	-0.48	-0.56	0.06	-0.43	-0.02
80	0.48	3.29e-03	1.076	0.034	1.52	0.28	-0.67	-0.25	0.25	0.07	0.09	0.01	0.03	-0.37	0.00	0.94	-0.52	0.26	-0.66	-0.01	0.25	-0.18
80	0.56	2.82e-03	1.099	0.039	2.61	-0.32	1.61	-0.47	0.47	1.09	1.19	0.29	0.75	-0.14	0.08	0.09	0.34	0.66	0.99	0.12	0.77	0.10
80	0.63	2.50e-03	1.097	0.050	3.75	-0.85	1.95	-0.46	0.46	0.62	0.57	-0.01	1.77	-0.29	0.06	0.16	1.57	0.51	0.98	-0.04	-1.72	0.33
80	0.69	2.29e-03	1.063	0.063	4.22	0.18	0.95	-1.95	1.95	0.50	0.55	0.54	2.48	-0.35	-0.11	0.54	2.34	0.93	-0.55	-0.55	0.67	0.01
80	0.75	2.10e-03	1.196	0.069	5.27	2.14	-0.04	-1.20	1.20	1.48	-1.86	-0.44	0.06	-0.17	-0.07	0.78	-3.71	1.15	0.71	0.12	-1.81	0.43
110	0.13	1.67e-02	0.671	0.013	2.74	2.56	-1.10	0.00	0.00	0.06	0.06	0.14	0.31	-0.02	0.01	0.90	0.00	0.00	0.17	-0.03	0.15	0.10
110	0.22	9.86e-03	0.834	0.019	3.09	1.86	-2.87	0.00	0.00	-0.17	-0.17	-0.00	0.58	0.02	-0.14	-0.43	0.10	0.00	-0.82	-0.11	0.12	-0.20
110	0.31	7.00e-03	0.885	0.024	2.74	2.66	-1.83	-0.03	0.03	-0.12	-0.12	0.13	0.03	-0.02	0.12	0.01	-0.01	-0.16	0.56	0.22	0.22	0.24
110	0.40	5.42e-03	0.994	0.031	1.44	-0.06	-1.14	-0.02	0.02	0.18	0.18	0.04	0.18	-0.32	-0.24	0.27	0.48	0.06	0.44	-0.01	-0.22	-0.35
110	0.48	4.52e-03	1.076	0.038	1.86	0.53	-0.87	-0.18	0.18	0.35	0.24	0.28	0.46	-0.45	0.47	-0.50	0.93	-0.41	-0.87	0.03	-0.23	0.52
110	0.56	3.87e-03	1.052	0.043	3.03	-0.76	-0.35	-0.21	0.21	-1.62	-1.85	0.15	0.23	-0.03	0.49	-0.64	-1.45	0.87	-0.99	0.50	-1.18	-0.20
110	0.63	3.44e-03	1.090	0.061	2.93	-1.79	-0.41	-0.86	0.86	-0.25	-0.13	0.23	0.54	0.56	-0.32	0.20	-1.12	1.00	0.24	-0.07	-1.62	-0.59
110	0.69	3.14e-03	1.150	0.072	2.79	0.96	1.51	-0.99	0.99	-0.34	-1.06	0.15	0.69	0.07	-0.06	-0.38	-0.38	-0.61	0.55	-0.18	0.38	-1.45
110	0.75	2.89e-03	0.905	0.098	6.29	-1.68	2.06	-1.43	1.43	2.35	0.48	-1.00	0.40	-0.04	0.54	1.98	-2.41	-0.42	-0.50	-0.30	-4.06	-0.74

Table A.2: LER reduced cross sections.

A.3 MER reduced cross sections

Q^2	y	x	$\tilde{\sigma}$	δ_{stat}	$\delta_{\text{syst.}}$	δ_1		δ_2		δ_3		δ_4		δ_5		δ_6	δ_7		δ_8		δ_9	
(GeV^2)				(abs.)	(%)	+	−	+	−	+	−	+	−	+	−		+	−	+	−	+	−
24	0.13	2.91e-03	0.891	0.024	6.54	3.22	-2.21	0.00	0.00	-0.01	-0.01	-1.65	2.91	2.47	-1.01	0.68	0.00	0.00	-2.63	-0.46	3.23	-1.00
24	0.22	1.72e-03	1.096	0.026	4.86	3.37	-3.78	-0.01	0.00	0.18	0.18	-1.49	1.68	0.93	-0.87	-0.95	0.05	0.00	-0.91	-0.26	1.96	-0.61
24	0.31	1.22e-03	1.115	0.025	3.73	2.26	-1.31	-0.04	0.04	-0.30	-0.30	-0.74	2.14	1.35	-0.26	-0.22	-0.33	-0.54	0.14	-0.14	1.40	-0.67
24	0.40	9.47e-04	1.249	0.029	2.59	1.65	-1.46	-0.21	0.21	0.43	0.42	-0.40	0.35	0.39	-0.57	-0.19	-0.21	-0.30	-0.05	-0.16	1.78	-0.57
24	0.48	7.89e-04	1.289	0.031	3.29	-0.31	0.70	-0.44	0.44	-0.11	-0.11	0.45	0.51	-0.05	-0.29	-0.05	-0.93	-0.82	-1.50	-0.16	2.59	-0.17
24	0.56	6.76e-04	1.309	0.035	3.02	0.59	-0.28	-0.72	0.72	-0.76	-0.50	-0.49	0.35	-0.47	-0.00	-0.30	0.09	-0.02	0.17	-0.40	2.64	-0.25
24	0.63	6.01e-04	1.306	0.044	3.28	-1.01	-0.20	-0.97	0.97	-0.88	-1.25	-1.03	1.83	0.02	-0.04	-0.02	0.50	0.87	0.44	0.18	1.72	0.07
24	0.69	5.49e-04	1.391	0.052	3.36	0.98	0.79	-1.44	1.44	-0.54	-0.51	0.23	0.05	0.12	-0.55	-1.10	0.40	-1.45	-1.61	-0.09	1.30	0.30
24	0.75	5.05e-04	1.333	0.062	4.26	-0.40	1.27	-2.88	2.88	-0.53	-0.23	-1.12	-1.28	0.64	-0.10	-0.85	0.48	-0.37	-0.73	-0.24	2.10	0.12
32	0.13	3.88e-03	0.907	0.017	2.68	1.85	-1.70	0.00	0.00	0.07	0.07	-0.33	1.13	0.66	-0.64	0.05	0.00	0.00	-0.89	0.23	1.12	-0.70
32	0.22	2.30e-03	1.060	0.020	3.83	2.94	-2.99	-0.01	0.01	0.06	0.09	-0.20	1.23	0.54	-0.70	-0.18	0.00	0.00	-1.01	0.21	1.63	-0.30
32	0.31	1.63e-03	1.156	0.024	3.49	1.68	-2.36	-0.05	0.05	-0.08	-0.08	-0.12	1.26	-0.03	-0.56	-0.12	0.49	-0.16	-1.09	-0.06	1.80	-0.40
32	0.40	1.26e-03	1.209	0.028	3.39	1.43	-1.31	-0.12	0.12	0.56	0.48	-0.41	1.41	0.15	-0.71	0.01	0.25	-0.36	-1.08	0.08	2.31	-0.22
32	0.48	1.05e-03	1.323	0.034	2.77	0.63	-0.15	-0.23	0.23	-0.15	-0.18	-0.74	0.95	0.58	0.43	-0.11	-0.97	0.20	0.42	-0.41	2.20	-0.05
32	0.56	9.01e-04	1.269	0.039	2.16	0.05	-0.58	-0.65	0.65	-0.81	-0.69	-1.04	0.54	-0.03	-0.26	-0.28	-0.63	0.35	0.06	-0.02	1.26	-0.31
32	0.63	8.01e-04	1.346	0.053	1.98	0.56	0.35	-0.86	0.86	-0.77	0.59	-0.94	0.21	0.22	0.09	-0.37	-0.23	-0.20	0.45	-0.29	0.97	-0.39
32	0.69	7.32e-04	1.307	0.059	3.94	-0.31	0.74	-1.27	1.27	0.15	1.12	-1.32	-0.42	-0.14	-0.24	0.65	-0.88	2.74	-0.83	-0.58	1.31	-0.53
32	0.75	6.73e-04	1.351	0.070	5.04	0.33	-3.73	-2.07	2.07	-0.05	-1.20	-1.11	1.56	-0.22	-0.63	-0.44	-0.43	0.41	-1.49	-0.77	-0.04	0.59
45	0.13	5.46e-03	0.891	0.015	3.84	2.59	-2.09	0.00	0.00	-0.01	-0.01	0.76	1.29	0.39	-0.10	-0.27	0.00	0.00	-0.64	-0.09	2.40	-0.52
45	0.22	3.23e-03	1.028	0.019	3.74	2.96	-2.49	-0.01	0.01	-0.00	-0.00	0.11	1.06	-0.13	0.13	-0.22	0.11	0.00	0.16	0.03	2.00	-0.27
45	0.31	2.29e-03	1.120	0.024	2.98	2.14	-1.93	-0.04	0.04	-0.14	-0.14	-0.13	0.94	0.09	-0.28	-0.15	-0.21	0.04	0.46	-0.14	1.75	-0.14
45	0.40	1.78e-03	1.168	0.030	3.85	2.68	-1.66	-0.16	0.16	0.32	0.32	-0.06	1.13	-0.13	0.76	-0.04	-0.72	0.09	-1.56	-0.22	1.65	-0.33
45	0.48	1.48e-03	1.255	0.038	1.85	-0.62	0.47	-0.28	0.28	0.21	0.33	-0.75	0.31	0.11	-0.59	0.05	-0.15	0.56	0.17	0.00	1.26	-0.06
45	0.56	1.27e-03	1.287	0.043	1.76	-0.86	0.63	-0.37	0.37	-0.12	-0.15	-0.13	0.53	0.09	-0.02	-0.33	0.05	0.58	0.34	-0.07	1.17	-0.33
45	0.63	1.13e-03	1.362	0.060	3.37	2.33	1.13	-0.93	0.93	1.21	1.54	0.49	-0.17	0.27	-0.29	-0.67	-0.11	-0.58	-0.77	-0.36	-0.51	-1.00
45	0.69	1.03e-03	1.415	0.069	2.78	-1.24	-2.09	-1.19	1.19	-0.02	0.24	0.33	-0.45	-0.14	-0.21	0.01	0.69	-0.82	-0.15	0.58	0.80	0.33
45	0.75	9.47e-04	1.362	0.074	4.12	0.83	-2.10	-1.53	1.53	1.04	-1.90	0.74	-0.85	-0.32	0.24	0.26	1.64	2.14	1.01	-0.48	0.36	-0.33
60	0.13	7.28e-03	0.811	0.016	2.87	2.14	-2.14	0.00	0.00	-0.03	-0.03	-0.66	0.80	-0.45	-0.13	-0.53	0.00	0.00	-0.18	-0.15	1.57	0.01
60	0.22	4.30e-03	0.970	0.022	3.34	3.01	-2.48	0.00	0.00	-0.03	-0.03	-0.18	0.51	0.12	0.09	-0.21	0.01	0.00	0.14	0.29	1.31	-0.17
60	0.31	3.05e-03	1.112	0.029	2.65	1.80	-1.69	-0.03	0.03	-0.15	-0.15	-0.80	0.17	-0.32	0.32	-0.55	0.61	0.16	-0.89	0.44	1.24	0.30
60	0.40	2.37e-03	1.165	0.035	1.59	0.81	-1.11	-0.05	0.05	-0.05	-0.05	-0.73	0.50	0.69	-0.54	-0.18	0.04	-0.35	-0.01	0.02	0.40	0.03
60	0.48	1.97e-03	1.144	0.042	1.52	0.59	-0.54	-0.19	0.19	0.33	0.33	0.23	-0.55	0.09	0.10	-0.72	0.46	0.06	-0.35	0.07	-0.79	0.19
60	0.56	1.69e-03	1.268	0.051	2.04	-0.58	0.86	-0.44	0.44	0.17	0.20	0.35	0.76	-0.10	0.55	-0.03	-0.66	0.53	-1.31	0.23	-0.39	0.38
60	0.63	1.50e-03	1.402	0.071	3.42	0.30	-1.10	-0.59	0.59	-0.17	-0.43	-0.65	-1.63	-0.34	-0.36	0.07	-1.27	-2.27	-1.33	0.31	0.48	0.16
60	0.69	1.37e-03	1.297	0.079	3.61	-0.36	0.70	-1.36	1.36	0.78	1.22	0.34	0.67	0.53	0.30	0.03	2.81	-2.09	0.33	0.10	-0.36	0.69
60	0.75	1.26e-03	1.360	0.089	6.62	0.49	3.30	-1.43	1.43	-0.38	-0.44	1.23	1.33	-0.21	1.12	2.62	-3.65	2.34	0.07	0.43	-2.69	0.08
80	0.13	9.71e-03	0.752	0.017	3.10	2.89	-2.14	0.00	0.00	0.04	0.04	-0.10	-0.24	0.12	0.08	0.46	0.00	0.00	0.01	-0.14	0.96	0.03
80	0.22	5.74e-03	0.943	0.024	3.03	2.86	-2.60	0.00	0.00	0.05	0.05	-0.47	-0.10	0.32	0.01	0.06	0.00	0.00	-0.48	-0.12	0.66	0.04
80	0.31	4.07e-03	1.065	0.032	2.30	1.15	-2.02	0.00	0.00	-0.05	0.03	-0.54	0.39	-0.13	-0.48	-0.28	0.64	-0.25	-0.05	-0.05	0.45	0.03
80	0.40	3.15e-03	1.109	0.040	1.93	-0.13	-1.18	-0.07	0.07	0.19	0.27	0.27	0.78	-0.82	-0.00	0.30	0.26	0.30	-0.77	-0.02	0.46	-0.14

Table A.3: MER reduced cross sections.

Q^2 (GeV^2)	y	x	$\tilde{\sigma}$	δ_{stat} (abs.)	$\delta_{\text{syst.}}$ (%)	δ_1 +	δ_1 −	δ_2 +	δ_2 −	δ_3 +	δ_3 −	δ_4 +	δ_4 −	δ_5 +	δ_5 −	δ_6	δ_7 +	δ_7 −	δ_8 +	δ_8 −	δ_9 +	δ_9 −
80	0.48	2.63e-03	1.156	0.048	1.69	-0.42	-0.96	-0.21	0.21	-0.72	-0.72	0.44	0.53	-0.48	0.04	-0.66	0.34	0.28	0.20	0.45	-0.30	0.33
80	0.56	2.25e-03	1.201	0.058	3.24	2.22	0.38	-0.56	0.56	0.77	0.64	0.33	1.43	-0.04	0.40	-1.38	-0.42	-0.17	0.10	0.33	0.53	-0.29
80	0.63	2.00e-03	1.245	0.077	4.49	-2.90	-1.85	-0.75	0.75	-0.60	0.87	-0.58	0.42	0.18	-1.04	-0.22	1.28	-2.44	1.59	0.01	0.64	0.47
80	0.69	1.83e-03	1.221	0.088	4.12	-0.77	2.13	-1.33	1.33	0.38	1.12	-0.11	1.16	-0.29	0.28	1.40	0.38	-0.12	0.16	-0.74	2.32	0.47
80	0.75	1.68e-03	1.439	0.107	4.18	0.59	-0.73	-1.36	1.36	-0.87	-1.54	-0.75	-0.08	0.01	-0.14	-0.57	2.03	-1.49	1.71	-0.23	-2.17	-0.45
110	0.13	1.34e-02	0.725	0.019	2.43	1.06	-2.00	0.00	0.00	0.12	0.12	-0.75	0.66	-0.14	-0.68	-0.48	0.00	0.00	0.69	0.18	0.45	-0.22
110	0.22	7.89e-03	0.837	0.026	2.94	2.58	-2.78	0.00	0.00	-0.01	-0.01	-0.11	0.46	-0.24	-0.51	0.50	-0.19	0.00	0.03	0.12	0.27	0.38
110	0.31	5.60e-03	0.978	0.035	2.98	2.64	-1.05	-0.01	0.01	-0.00	-0.00	0.78	0.28	0.19	0.56	0.07	0.84	-0.64	-0.36	-0.37	-0.39	0.35
110	0.40	4.34e-03	1.050	0.044	2.44	1.20	-1.42	-0.03	0.03	0.68	0.68	0.03	0.75	0.18	0.38	-1.01	-0.19	-0.19	1.31	0.08	0.01	0.12
110	0.48	3.62e-03	1.090	0.055	2.86	1.13	-0.23	-0.34	0.34	-0.32	-0.35	-0.59	0.28	-0.03	-0.08	-0.14	-0.26	0.96	1.85	-0.19	0.77	1.39
110	0.56	3.10e-03	1.194	0.067	4.55	-2.96	0.64	-0.46	0.46	-1.65	-1.65	-0.53	0.02	-0.46	-0.46	-1.37	-1.58	-0.11	-1.36	0.15	1.53	1.40
110	0.63	2.76e-03	1.131	0.083	5.34	1.43	-0.27	-0.49	0.49	0.64	0.92	1.09	1.09	0.33	0.41	1.50	3.55	0.16	2.61	1.02	1.53	0.66
110	0.69	2.51e-03	1.221	0.103	6.50	-2.49	0.37	-0.80	0.80	-0.36	0.34	-0.44	0.90	-0.12	-0.88	-0.80	0.93	1.09	-2.87	0.05	4.86	0.44
110	0.75	2.31e-03	1.360	0.183	7.44	4.17	-0.82	-1.33	1.33	0.21	0.46	1.63	1.05	0.56	1.44	-1.28	-5.06	0.28	-1.46	0.00	-0.98	-1.40

Table A.3: MER reduced cross sections.

A.4 Reduced cross section for F_L extraction

Q^2	x	HER			LER			MER		
(GeV^2)		y_{HER}	$\tilde{\sigma}$	$\delta_{\mathrm{stat.}}$	y_{LER}	$\tilde{\sigma}$	$\delta_{\mathrm{stat.}}$	y_{MER}	$\tilde{\sigma}$	$\delta_{\mathrm{stat.}}$
24	1.08e-03	0.220	1.220	$\pm$0.016	0.440	1.193	$\pm$0.015	0.352	1.188	$\pm$0.022
24	8.16e-04	0.290	1.299	$\pm$0.018	0.580	1.252	$\pm$0.020	0.464	1.287	$\pm$0.028
24	6.67e-04	0.355	1.362	$\pm$0.018	0.710	1.257	$\pm$0.026	0.568	1.321	$\pm$0.030
32	1.43e-03	0.220	1.211	$\pm$0.012	0.440	1.201	$\pm$0.016	0.352	1.188	$\pm$0.021
32	1.09e-03	0.290	1.307	$\pm$0.016	0.580	1.264	$\pm$0.024	0.464	1.296	$\pm$0.030
32	8.89e-04	0.355	1.351	$\pm$0.016	0.710	1.331	$\pm$0.031	0.568	1.257	$\pm$0.033
45	2.02e-03	0.220	1.145	$\pm$0.011	0.440	1.133	$\pm$0.017	0.352	1.168	$\pm$0.023
45	1.53e-03	0.290	1.232	$\pm$0.016	0.580	1.263	$\pm$0.026	0.464	1.231	$\pm$0.033
45	1.25e-03	0.355	1.296	$\pm$0.017	0.710	1.248	$\pm$0.032	0.568	1.288	$\pm$0.037
60	2.69e-03	0.220	1.125	$\pm$0.013	0.440	1.106	$\pm$0.019	0.352	1.156	$\pm$0.026
60	2.04e-03	0.290	1.195	$\pm$0.018	0.580	1.178	$\pm$0.030	0.464	1.159	$\pm$0.037
60	1.67e-03	0.355	1.289	$\pm$0.020	0.710	1.254	$\pm$0.037	0.568	1.277	$\pm$0.044
80	3.59e-03	0.220	1.076	$\pm$0.014	0.440	1.070	$\pm$0.022	0.352	1.088	$\pm$0.029
80	2.72e-03	0.290	1.185	$\pm$0.020	0.580	1.089	$\pm$0.033	0.464	1.147	$\pm$0.043
80	2.22e-03	0.355	1.219	$\pm$0.022	0.710	1.138	$\pm$0.042	0.568	1.219	$\pm$0.049
110	4.93e-03	0.220	1.019	$\pm$0.016	0.440	1.039	$\pm$0.025	0.352	1.023	$\pm$0.033
110	3.74e-03	0.290	1.100	$\pm$0.022	0.580	1.073	$\pm$0.038	0.464	1.050	$\pm$0.048
110	3.05e-03	0.355	1.214	$\pm$0.026	0.710	1.074	$\pm$0.051	0.568	1.208	$\pm$0.057

Table A.4: Reduced cross sections for F_L extraction.

A.5 F_L

Q^2 (GeV^2)	x	F_L	δ_{stat} (abs.)	$\delta_{\text{syst.}}$ (%)	δ_1 +	δ_1 −	δ_2 +	δ_2 −	δ_3 +	δ_3 −	δ_4 +	δ_4 −	δ_5 +	δ_5 −	δ_6	δ_7 +	δ_7 −	δ_8 +	δ_8 −	δ_9 +	δ_9 −
24	1.08e-03	0.646	0.201	61.5	48.7	-49.3	3.1	-3.0	2.2	2.8	-16.1	26.2	14.5	-1.2	-7.7	4.1	-6.0	-10.1	0.4	15.8	-2.5
24	8.16e-04	0.432	0.127	32.7	22.2	-18.2	7.6	-7.6	-7.0	-2.6	-15.8	6.3	9.9	-7.3	1.1	3.7	8.8	-5.6	0.6	-3.3	-2.4
24	6.67e-04	0.423	0.087	33.9	13.1	-13.9	14.3	-14.3	0.4	-0.5	-11.3	17.4	5.5	-0.5	2.6	-17.6	0.3	-8.4	-2.1	5.4	0.5
32	1.43e-03	0.517	0.184	57.7	52.8	-47.5	3.2	-2.5	0.7	0.7	-8.0	7.5	-3.0	-2.2	-7.3	4.1	-3.6	-19.3	1.1	3.3	4.9
32	1.09e-03	0.415	0.131	38.5	22.0	-29.6	6.3	-6.4	9.3	6.0	0.3	14.8	1.5	-7.0	-6.2	8.9	-2.1	-4.0	-0.7	-0.7	-8.9
32	8.89e-04	0.255	0.095	48.0	26.4	-25.6	23.1	-21.7	6.7	12.0	16.7	7.1	5.1	-8.8	-1.6	-10.6	5.7	-2.8	-4.8	20.8	-8.6
45	2.02e-03	0.470	0.187	65.1	52.5	-38.2	3.9	-4.6	-1.8	-1.3	25.5	11.7	16.2	-9.7	-3.7	-4.0	5.9	-16.8	-8.7	14.6	-4.5
45	1.53e-03	0.097	0.139	189.1	94.8	-173.5	22.6	-21.7	8.1	-8.7	-5.9	38.0	23.4	-19.4	-0.0	8.4	3.2	41.9	7.9	35.7	14.8
45	1.25e-03	0.259	0.099	54.4	22.0	-29.4	16.1	-16.3	4.5	2.8	5.3	24.7	5.8	-3.9	-15.7	14.8	-25.5	-0.1	4.0	16.0	-5.1
60	2.69e-03	0.516	0.211	54.9	33.7	-50.9	2.3	-3.2	-0.2	-0.6	-11.1	3.9	-6.6	0.5	-9.3	2.1	7.1	3.6	0.9	5.6	-10.1
60	2.04e-03	0.305	0.157	54.7	51.3	-32.6	6.1	-5.8	-1.0	-0.1	-8.0	4.0	-4.6	5.3	-9.6	4.1	5.9	2.1	7.6	4.1	-7.0
60	1.67e-03	0.231	0.114	50.2	34.9	-37.3	15.4	-15.4	-5.7	-11.0	-12.4	-8.8	-7.9	4.5	-2.5	-7.1	1.4	-11.5	-0.6	19.1	1.7
80	3.59e-03	0.413	0.234	43.6	40.0	-9.7	2.7	-3.0	-0.8	-0.9	-7.4	2.6	1.4	11.3	3.5	-1.0	4.3	3.7	-0.6	8.1	2.2
80	2.72e-03	0.621	0.173	42.8	15.6	-39.1	3.8	-3.8	-7.3	-8.0	-4.1	-2.5	0.7	-0.9	-5.1	-2.8	-7.7	-10.7	-2.5	3.4	-2.3
80	2.22e-03	0.326	0.127	29.2	12.2	-16.2	11.1	-11.3	-12.2	-1.5	-2.2	-7.8	6.2	-3.8	-6.7	9.6	-7.2	-1.3	0.4	8.5	-0.5
110	4.93e-03	0.197	0.262	142.3	92.8	-135.1	4.2	-4.1	-11.7	-8.8	-1.0	6.4	5.4	-17.4	1.8	-34.6	11.3	6.5	3.9	16.1	6.1
110	3.74e-03	0.340	0.197	55.3	40.2	-46.1	6.9	-6.6	15.1	17.6	3.1	-8.3	3.1	-4.0	1.8	15.1	-17.0	9.5	-3.2	10.6	-1.2
110	3.05e-03	0.466	0.153	19.4	14.4	-3.9	4.9	-5.2	-0.3	3.1	2.1	-2.5	-0.5	1.5	1.5	8.0	1.3	-4.4	1.6	2.6	6.0

Table A.5: F_L.

Appendix B

Systematic uncertainties

Uncertainty from each systematic source is shown for each measured bin. The colored area region corresponds to the amount of total systematic uncertainty.

B.1 Reduced cross section measurement

B.1.1 HER reduced cross section

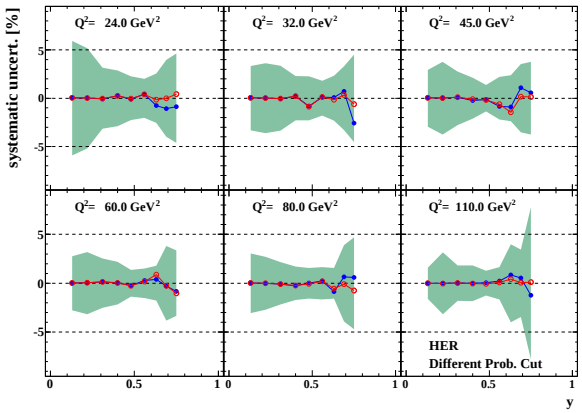

Figure B.1: Electron finding.

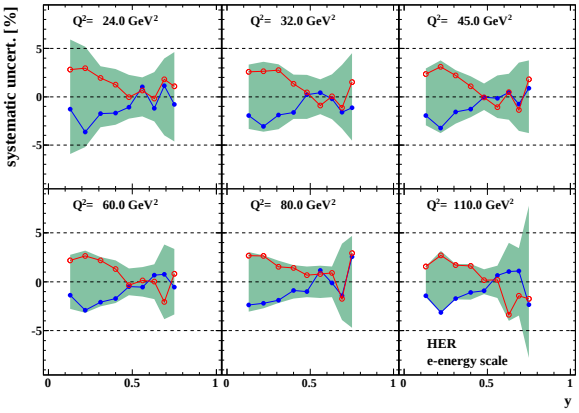

Figure B.2: Energy scale.

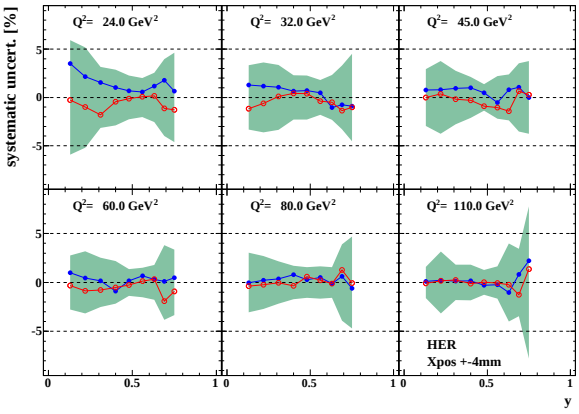

Figure B.3: x position of the positron.

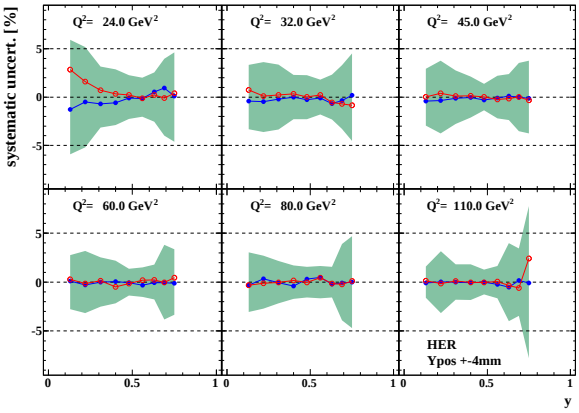

Figure B.4: y position of the positron.

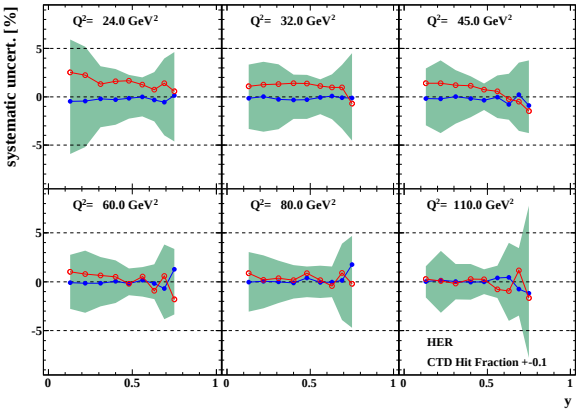

Figure B.5: CTD Hit fraction.

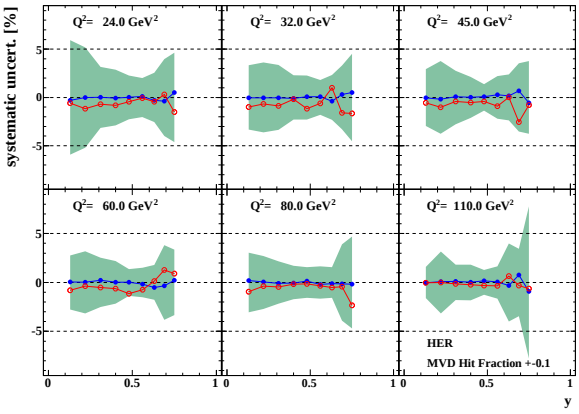

Figure B.6: MVD Hit fraction.

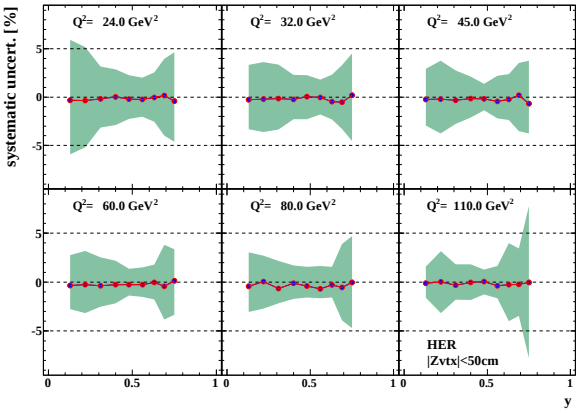

Figure B.7: Z_{vtx}.

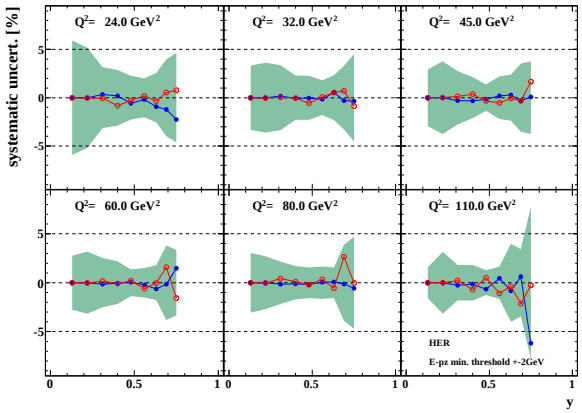

Figure B.8: $\sum(E - p_z)$ minimum threshold.

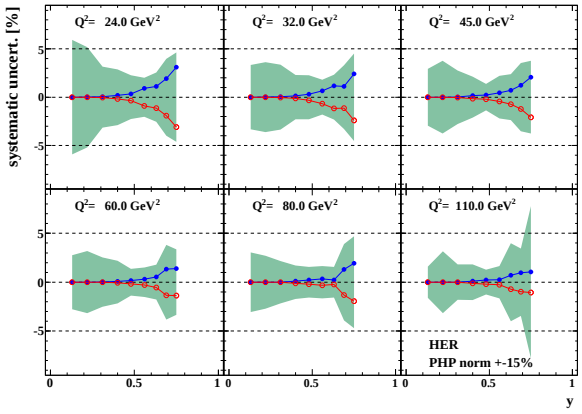

Figure B.9: PHP normalization factor.

B.1.2 LER reduced cross section

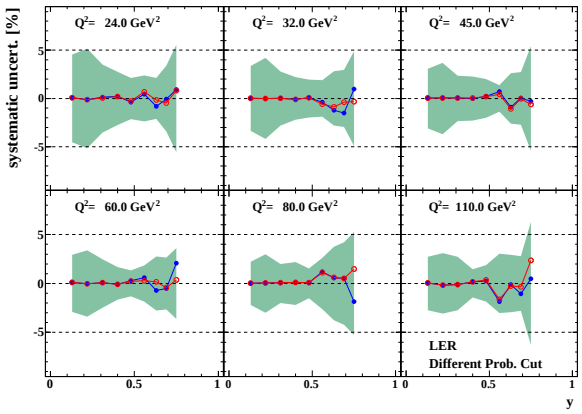

Figure B.10: Electron finding.

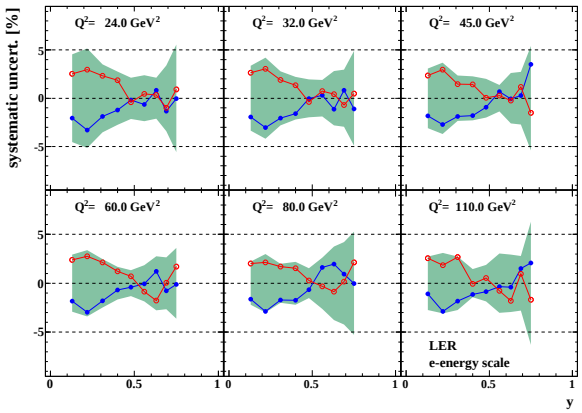

Figure B.11: Energy scale.

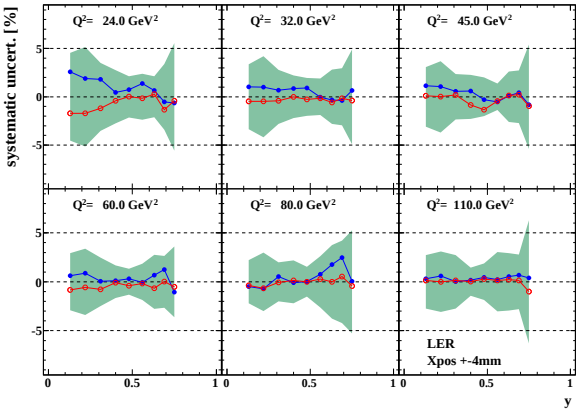

Figure B.12: x position of the positron.

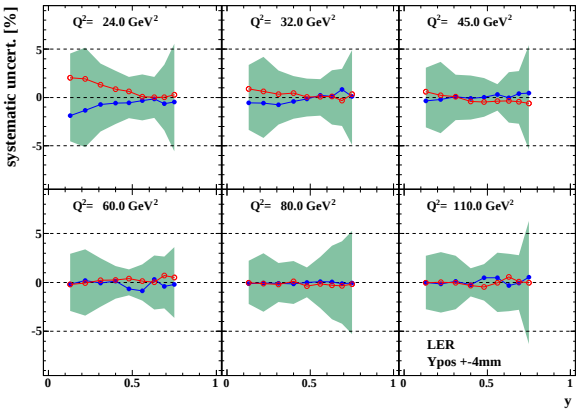

Figure B.13: y position of the positron.

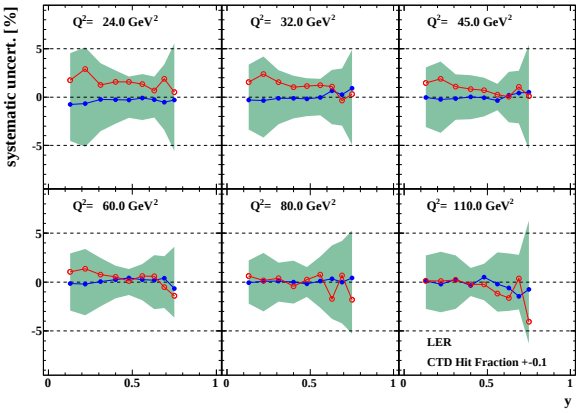

Figure B.14: CTD Hit fraction.

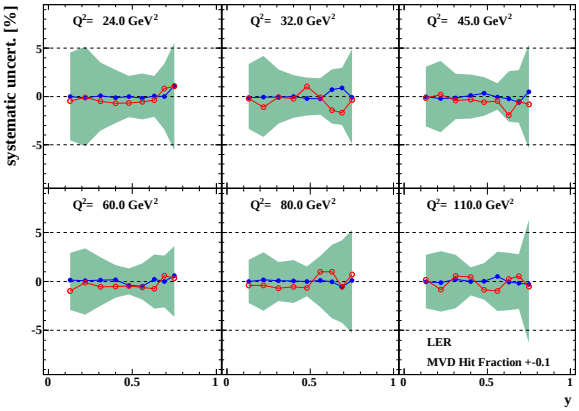

Figure B.15: MVD Hit fraction.

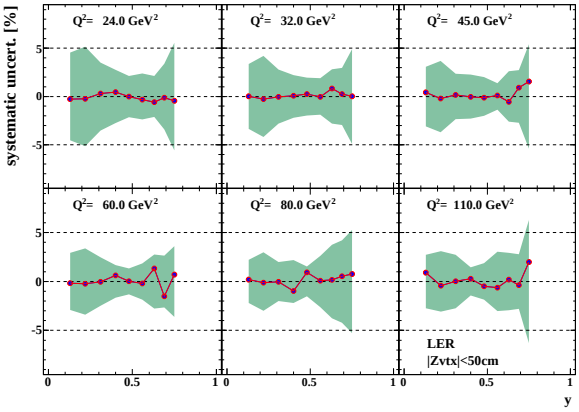

Figure B.16: Z_{vtx}.

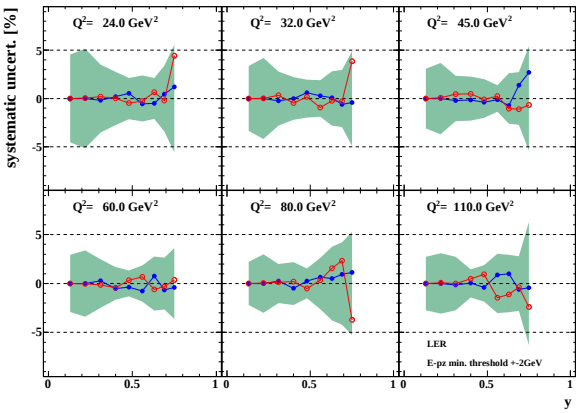

Figure B.17: $\sum(E - p_z)$ minimum threshold.

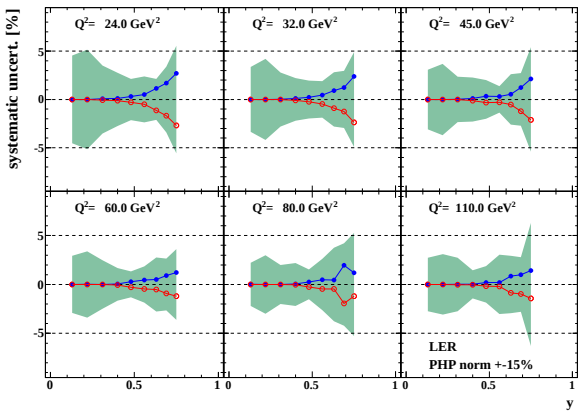

Figure B.18: PHP normalization factor.

B.1.3 MER reduced cross section

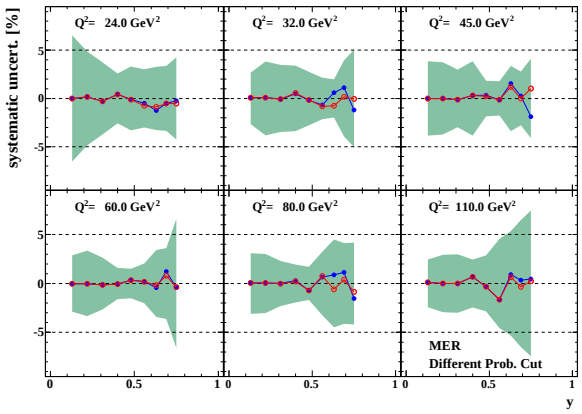

Figure B.19: Electron finding.

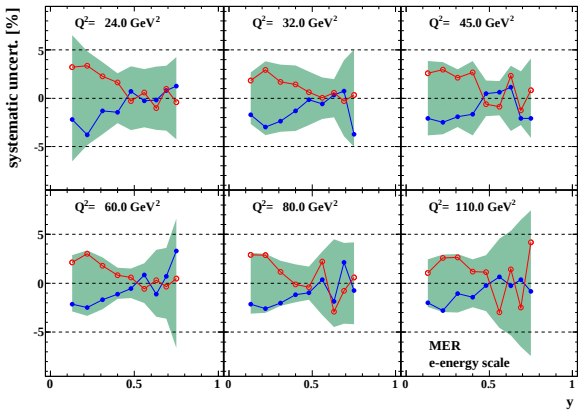

Figure B.20: Energy scale.

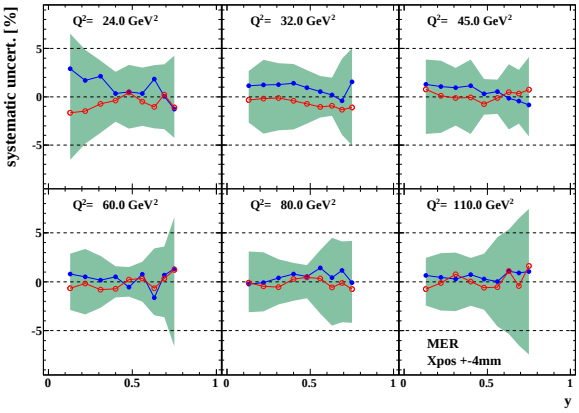

Figure B.21: x position of the positron.

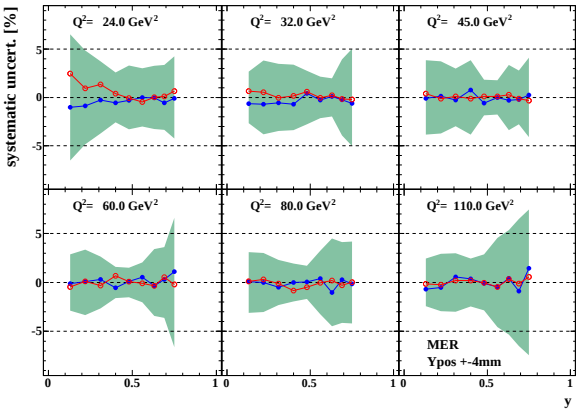

Figure B.22: y position of the positron.

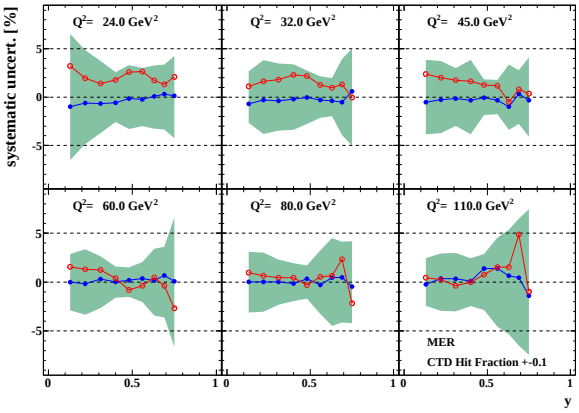

Figure B.23: CTD Hit fraction.

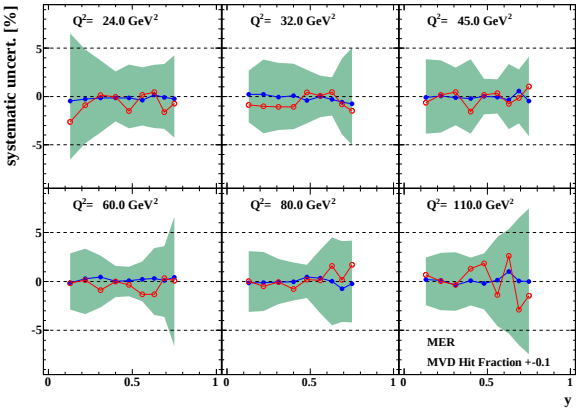

Figure B.24: MVD Hit fraction.

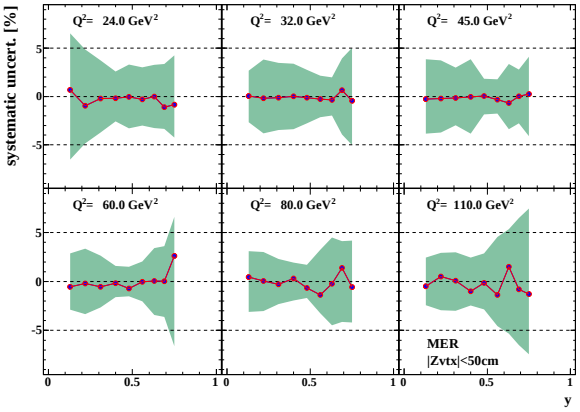

Figure B.25: Z_{vtx}.

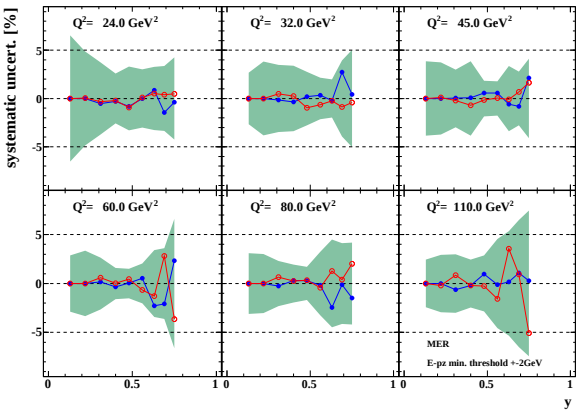

Figure B.26: $\sum(E - p_z)$ minimum threshold.

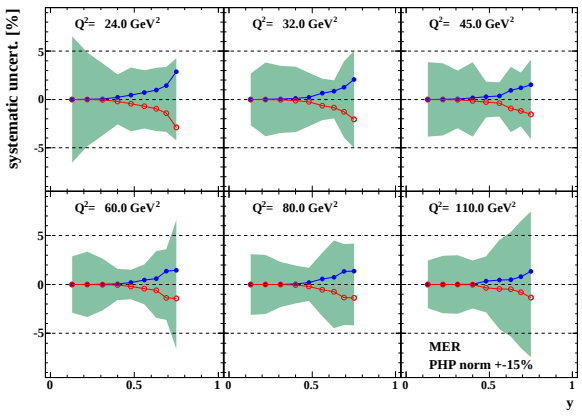

Figure B.27: PHP normalization factor.

B.2 F_L measurement

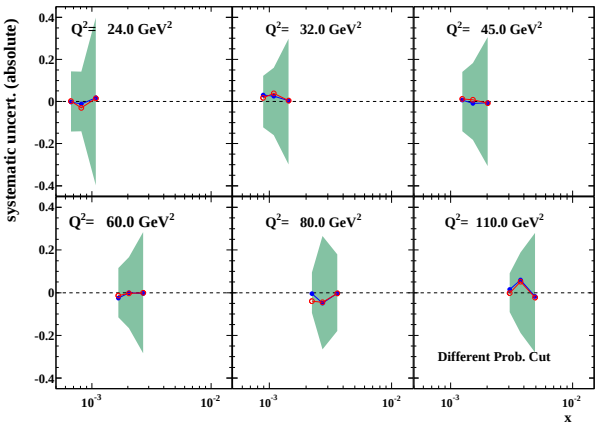

Figure B.28: Electron finding.

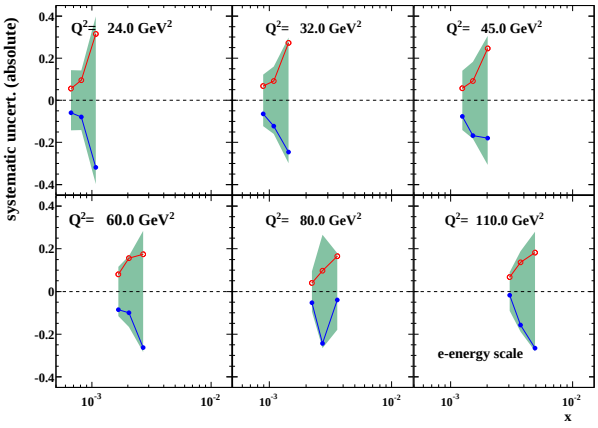

Figure B.29: Energy scale.

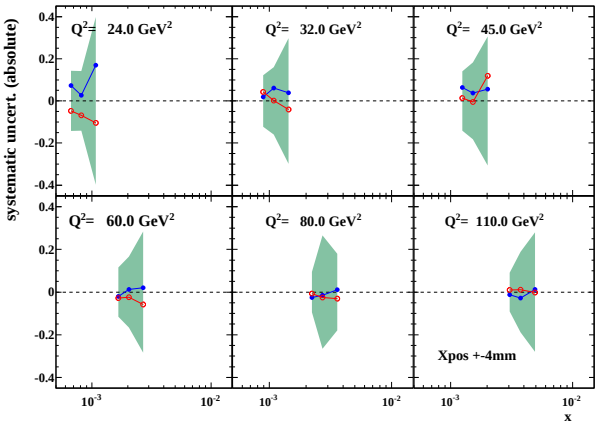

Figure B.30: x position of the positron.

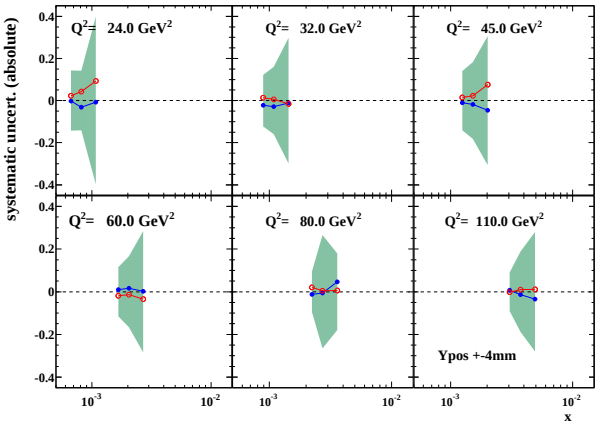

Figure B.31: y position of the positron.

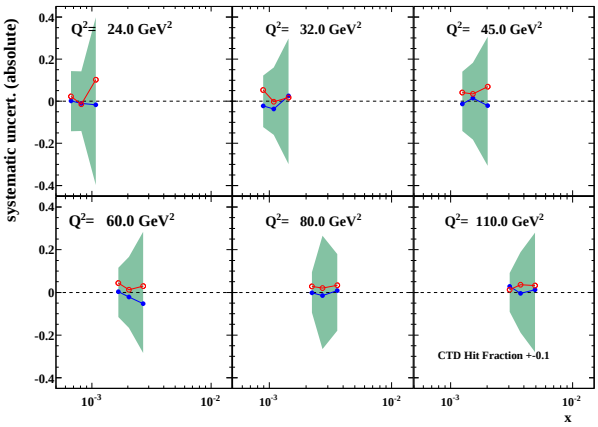

Figure B.32: CTD Hit fraction.

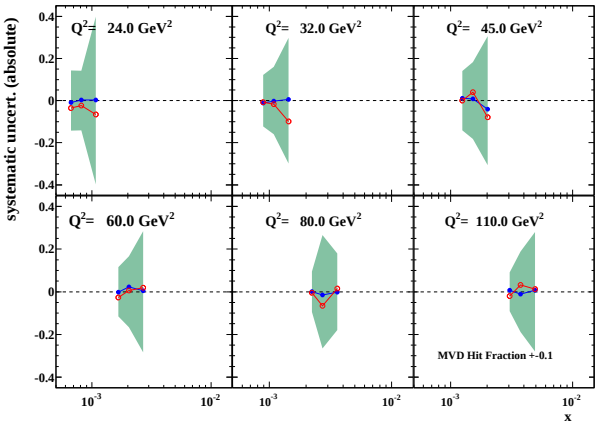

Figure B.33: MVD Hit fraction.

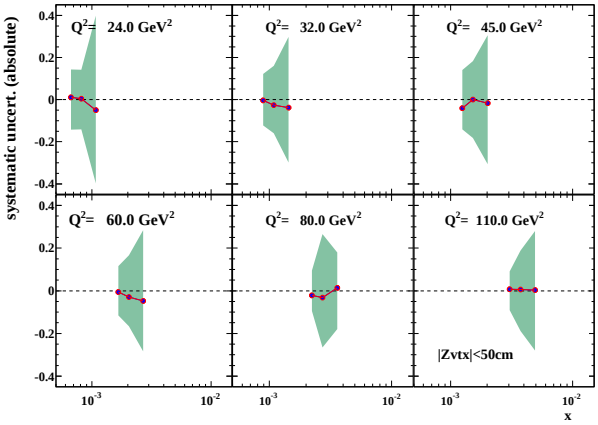

Figure B.34: Z_{vtx}.

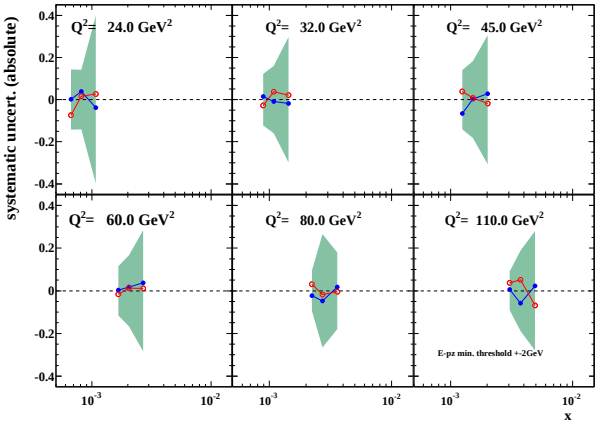

Figure B.35: $\sum(E - p_z)$ minimum threshold.

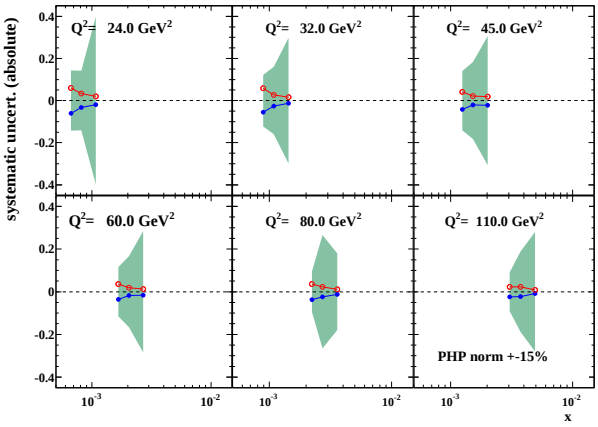

Figure B.36: PHP normalization factor.

Appendix C

Definition of samples

The event selection of the samples used for various checks are described.

C.1 Sample for HES efficiency

The HES efficiency is checked using the sample selected as the standard DIS event selections with following modifications.

- No requirement of a HES hit for the scattered positron. If its position cannot be reconstructed from the HES, position from the CAL is used.
- $R_{\mathrm{CAL}} < 115$ cm. This requirement to eliminate the bias from the outer region where the HES is not equipped.

C.2 Sample for vertex reconstruction efficiency

The sample is selected in the similar way as the standard DIS event selections but with the following variations.

- No vertex requirement.
- No backward tracking requirement. The backward tracking definitely needs reconstructed vertex.
- $\sum(E - p_z) > 50$ GeV. This requirement is to reduce the amount of Photoproduction events increased by the absence of the backward tracking requirement.
- $R_{\mathrm{HES}} > 30$ cm. The radius cut is applied by the position reconstructed by the HES to avoid any inter- or extra- polation of the position using the vertex.
- $\sum p_T < 20$ GeV. This requirement is to suppress the beam originated or cosmic background events which are rejected by vertex requirement.

C.3 6m tagged sample

The selection for the 6m tagger is as following.

- Data taken with good condition of the 6m tagger.
- The position of the cell with highest energy should be

$$1 \leq i_x \leq 12 \quad \text{AND} \quad 1 \leq i_y <\leq 2,$$

  where i_x and i_y are cell index in x and y, respectively.
- Energy reconstructed by 3×3 cells should be

$$3.0 \leq E_{3\times3} \leq 10.5\text{GeV}.$$

- The ratio of energy reconstructed from 3×3 cells to that from 5×5 should be

$$E_{3\times3}/E_{5\times5} > 0.65.$$

- Cut on noisy part of the 6m tagger.

Appendix D

FLT logic

D.1 Medium-Q^2 trigger Logic

The FLT requirement is to fire one of the following 11 slots.

The first 2 slots are the main slots for the HER data analysis. They inclusively take events with low energy positrons at the outside the RCAL 1st inner ring.

- slot 30: ($E_{\mathrm{REMC},>1ir} > 2.0$ GeV OR $E_{\mathrm{REMC},1ir} > 15.0$ GeV) AND *Risoe*
- slot 37: $E_{\mathrm{REMC},>1ir} > 1$ GeV AND *good track*

$E_{\mathrm{REMC},>1ir}$ is the total REMC energy excluding the RCAL 1st inner ring, while $E_{\mathrm{REMC},1ir}$ is the EMC energy of the RCAL 1st inner ring. *Risoe* is the isolated EMC energy deposit with the EMC energy above 2 GeV. While the other entire DIS slots for the RCAL positrons require *Risoe*, slot 37 is independent from the *Risoe* and requires *good track* instead, which can be expected from hadronic activity with large angle in the high y events.

The next 3 slots are general DIS slots to tag the positron in the RCAL, though they have no exclusive events with the positron outside the 1st inner ring, which would be always also tagged by slot 30.

- slot 36: ($E_{\mathrm{REMC},>1ir} > 3.4$ GeV OR $E_{\mathrm{REMC},1ir} > 5.0$ GeV) AND *FCAL energy around the beam pipe* > 5.0 GeV AND *Risoe*
- slot 46: ($E_{\mathrm{REMC},>1ir} > 2.0$ GeV OR $E_{\mathrm{REMC},1ir} > 3.8$ GeV) AND *good track* AND *Risoe* AND *3 quadrants*
- slot 47: ($E_{\mathrm{REMC},>1ir} > 2.0$ GeV OR $E_{\mathrm{REMC},1ir} > 3.8$ GeV) AND *Risoe* AND $E_{\mathrm{CAL}} > 4$ GeV AND *3 quadrants*

The RCAL region around the beam pipe is separated into 4 quadrants. *3 quadrants* means *Risoe* exists in one of the 3 quadrants excepting the one hit by the off-momentum positrons. E_{CAL} is the total CAL energy excluding 3 inner rings in the FCAL and the RCAL 1st inner ring.

The rest of the slots are mainly for high Q^2 events which have high energy positrons in the BCAL.

- slot 28: *Isoe in the FCAL or BCAL* AND *good track* AND $E_{T,all} > 18$ GeV
- slot 40: $E_{\mathrm{EMC}} > 20$ GeV
- slot 41: $E_T > 30$ GeV
- slot 43: $E_T > 15$ GeV AND *good track*
- slot 44: ($E_{\mathrm{BEMC}} > 4.7$ GeV OR $E_{\mathrm{REMC},>1ir} > 3.4$ GeV) AND *good track*
- slot 62: multiple *Isoe*

While E_T is the total E_T of the CAL excluding the inner rings, $E_{T,all}$ includes the FCAL towers around the beam pipe.

D.2 Low-Q^2 trigger logic

The FLT requirement is again to fire one of the 11 slots as in the HER logic, but some of them have looser criteria.

The first 2 slots are the same as in the HER trigger logic.

The next 3 slots are loosened especially to take events with positrons at the RCAL 1st inner ring.

- slot 36: ($E_{\mathrm{REMC},>1ir} > 2.0$ GeV OR $E_{\mathrm{REMC},1ir} > 2.5$ GeV) AND *FCAL energy around the beam pipe* > 5.0 GeV AND *Risoe*
- slot 46: ($E_{\mathrm{REMC},>1ir} > 2.0$ GeV OR $E_{\mathrm{REMC},1ir} > 2.5$ GeV) AND *good track* AND *Risoe* AND *3 quadrants*
- slot 47: ($E_{\mathrm{REMC},>1ir} > 2.0$ GeV OR $E_{\mathrm{REMC},1ir} > 2.5$ GeV) AND *good track* AND *Risoe* AND $E_{\mathrm{CAL}} > 4$ GeV

While slot 36 takes non-diffractive events, the slot 47 takes events mainly. The slot 46 is a backup slot for the slot 47.

The last 6 slots for high Q^2 events are unchanged from the HER.

Bibliography

[1] E. Rutherford, Philos. Mag **21** (1911), 669.

[2] C.H. Llewellyn Smith, Phys. Rep. **3C** (1972), 261.

[3] C.G. Callan and D.J. Gross, Phys. Rev. Lett. **22** (1969), 156.

[4] Y.L. Dokshitzer, Sov. Phys. JETP **46** (1977), 641.

[5] V.N. Gribov and L.N. Lipatov, Sov. J. Nucl. Phys. **15** (1972), 438.

[6] L.N. Lipatov, Sov. J. Nucl. Phys. **20** (1975), 96.

[7] G. Altarelli and G. Parisi, Nucl. Phys. **B126** (1977), 298.

[8] K. Prytz, Phys. Lett. **B311** (1993), 286.

[9] Particle Data Group, C. Amsler, et al., *Review of particle physics*, Phys. Lett. **B 667** (2008), 1–1340.

[10] G. Altarelli and G. Martinelli, Phys. Lett. **B76** (1978), 89.

[11] R. Devenish and A. Cooper-Sarkar, *Deep Inelastic Scattering*, Oxford, 2004.

[12] ZEUS Coll., S. Chekanov, et al., Eur. Phys. J. C **42** (2005), 1.

[13] H1 Coll., C. Adloff, et al., Eur. Phys J. C **30** (2003), 1.

[14] The European Muon Collaboration, Nucl. Phys. B **259** (1985), 189.

[15] L. W. Whitlow et al., Phys. Lett. B **250** (1990), 193.

[16] BCDMS Collab., A. C. Benvenuti, et al., Phys. Lett. B **223** (1989), 485.

[17] The New Muon Collaboration, Nucl. Phys. B **483** (1997), 3.

[18] H1 Collab., C. Adloff, et al., Eur. Phys. J. C **21** (2001), 33.

[19] R.S. Thorne, *The longitudinal structure function at HERA*, Proc. of XVI Int. Workshop on Deep-Inelastic Scattering and Related Topics (London, England), April 2008.

[20] ZEUS Coll. , *The ZEUS detector*, Status report, DESY, 1993.

[21] A. Polini et al., Nucl. Inst. Meth. **A 581** (2007), 656.

[22] B. Foster et al., Nucl. Inst. Meth. A **338** (1994), 254.

[23] R. Hall-Wilton et al., *The CTD tracking resolution*, ZEUS-Note-99-024, 1999.

[24] A. Andersen et al., Nucl. Inst. Meth. A **309** (1991), 101.

[25] A. Bernstein et al., Nucl. Inst. Meth. A **336** (1993), 23.

[26] J. Grosse-Knetter, Ph.D. thesis, Univ. Hamburg, Hamburg, Germany, 1997.

[27] A. Dwuraźny et al., Nucl. Inst. Meth. A **277** (1989), 176.

[28] A. Bamberger et al., Nucl. Inst. Meth. A **401** (1997), 63.

[29] ZEUS Luminosity Group, J. Andruszków, et al., *Luminosity measurement in the ZEUS experiment*, ZEUS-Note-01-004, 2001.

[30] M. Helbich et al., Nucl. Inst. Meth. A **565** (2006), 572.

[31] J. Chwastowski et al., Nucl. Inst. Meth. A **504** (2003), 222.

[32] T. Gosau, Ph.D. thesis, Univ. Hamburg, Hamburg, Germany, 2007, DESY-THESIS-2007-028.

[33] W.H. Smith et al., *The ZEUS trigger system*, ZEUS-Note-89-084, 1989.

[34] H. Spiesberger, *HERACLES and DJANGOH: event generation for ep interaction at HERA includive radiative processes*, 2005, available on http://wwwthep.physik.uni-mainz.de/ hspiesb/djangoh/djangoh.html.

[35] H.L. Lai et al., Eur. Phys. J. C **12** (2000), 375.

[36] H. Spiesberger, *An event generator for ep interactions at HERA including radiative processes*, 1996, available on http://www.desy.de/ hspiesb/heracles.html.

[37] L. Lönnblad, Comput. Phys. Commun. **71** (1992), 15.

[38] T. Sjöstrand, Comput. Phys. Commun. **82** (1994), 74.

[39] T. Sjöstrand et al., *PYTHIA 6.206 manual*, 2002, available on http://www.thep.lu.se/ torbjorn/Pythia.html, [hep-ph/0108264].

[40] T. Sjöstrand et al., Comput. Phys. Commun. **135** (2001), 238.

[41] ZEUS Coll., Phys. Lett. B **293** (1992), 465.

[42] R. Brun et al., *Geant3*, CERN-DD/EE/84-1, CERN, 1987.

[43] F. Jacquet and A. Blondel, *Detection of the charged current event - method II*, Proceedings of the Study for an ep Facility for Europe (Hamburg, Germany) (U. Amaldi, ed.), 1979, p. 391, Also in preprint DESY 79/48.

[44] H. Abramowicz, A. Caldwell, and R. Sinkus, Nucl. Inst. Meth. **A 365** (1995), 508.

[45] R. Sinkus and T. Voss, Nucl. Inst. Meth. **A 391** (1997), 360.

[46] Ch. Amelung, *Electron position reconstruction in ZEUS: Further update of the ELECPO package*, ZEUS-Note-96-093, 1996.

[47] R. Yongdok, Ph.D. thesis, Tokyo Met. Univ., 2009.

[48] J. Grosse-Knetter, *Corrections for the hadronic final state*, ZEUS-Note-98-031, 1998.

[49] E. Maddox, *A Kalman filter track fit for the ZEUS microvertex detector*, ZEUS-Note-03-008, 2003.

[50] R. Frühwirth and A. Strandlie, Comp. Phys. Comm. **120** (1999), 197.

[51] ZEUS Coll., S. Chekanov, et al., Eur. Phys. J. C **21** (2001), 443.

[52] N. Tuning, Ph.D. thesis, University of Amsterdam, NIKHEF, Amsterdam, The Netherlands, 2001, ISBN: 90-646-4500-0.

[53] A. Arbuzov et al., Comput. Phys. Commun. **95** (1996), 128.

[54] A. Levy, *Energy dependence of $\sigma_{\rm tot}(\gamma p)$ at HERA*, Proc. of XVI Int. Workshop on Deep-Inelastic Scattering and Related Topics (London, England), April 2008.

[55] H1 Coll., F.D. Aaron, et al., Phys. Lett. **B 665** (2008), 139.

[56] P.M. Nadolsky et al., Phys. Rev. D **78** (2008), 013004.

[57] G. Watt, A.D. Martin, W.J. Stirling, and R.S. Thorne, *Recent progress in global PDF analysis*, Proc. of XVI Int. Workshop on Deep-Inelastic Scattering and Related Topics (London, England), April 2008.

[58] C. D. White and R. S. Thorne, Phys. Rev. D **75** (2007), 034005.